Theoretical and Experimental Characterization of Time-Dependent Signatures of Acoustic Wave Based Biosensors

A Thesis
Presented to
The Academic Faculty

by

Sang Hun Lee

In Partial Fulfillment
of the Requirements for the Degree
Doctor of Philosophy in the
School of Electrical and Computer Engineering

Georgia Institute of Technology
August 2006

Theoretical and Experimental Characterization of Time-Dependent Signatures of Acoustic Wave Based Biosensors

Approved by:

Dr. William D. Hunt, Advisor
School of Electrical and Computer Engineering
Georgia Institute of Technology

Dr. James S. Kenney
School of Electrical and Computer Engineering
Georgia Institute of Technology

Dr. Mark G. Allen
School of Electrical and Computer Engineering
Georgia Institute of Technology

Dr. A. Bruno Frazier
School of Electrical and Computer Engineering
Georgia Institute of Technology

Dr. Peter J. Edmonson
P.J. Edmonson, Ltd
Hamilton, ON, L9B 1A9, Canada

Date Approved: July 06, 2006

To my family:

My respected father and mother, Chang-Ho Lee and Kyoung-Ja Park
My beloved wife Young-Ah,
And my precious little ones, Iris (Ahyoung) and Keaton (Jeehoon)

ACKNOWLEDGEMENTS

Probably, the reason most people do not use first-person in their thesis is that reaching this point would not be possible without help of others. I am also indebted to so many people. First, I wish to express my heartfelt appreciation to my advisor Professor William Hunt for his continued support, confidence in me, and providing a perfect balance of freedom and guidance during the course of my study. My sincere thank goes also to my thesis committee members: Drs. Steve Kenney, Mark Allen, Bruno Frazier, and Peter Edmonson for reviewing my thesis and giving me invaluable suggestions. It is truly my great honor to have those as my thesis committee. My special thank goes to Dr. Edmonson for providing ideas which turned into a decent chapter to my thesis, as well as for making a long trip from Canada to attend my thesis defense presentation.

I am grateful for the cool guys in the Microelectronic Acoustics Group who made the lab an enjoyable place: Tony Dickherber, Chris Corso, Ryan Westafer, Eric Massey, Farasat Munir, and especially my long time colleague Dr. Desmond Stubbs who conducted thousands of experiments with me and shared so much frustration and elation.

I am forever thankful to my parents for their unwearied support, encouragement, and trust; my loving wife and adorable two kids for their sacrifice, patience, and love; my taciturn younger brother Sang-Mook who always wishes my success. I also acknowledge my parents-in-law Bong-Joo Park and Jung-Kum Kim for their love and prayers.

Finally, I wish to express my thanks to the people at U.S. Customs, GBI, ONDCP, CDC, and TSA for their support, interest in this research, and providing facilities and hard-to-find narcotics and explosive samples.

TABLE OF CONTENTS

LIST OF TABLES

LIST OF FIGURES

LIST OF ACRONYMS

APM Acoustic Plate Mode

BAW Bulk Acoustic Wave

BCA BioChip Arrayer™

BZE Benzoylecgonine, a metabolite of cocaine

CCM Cubic Centimeter per Minute

CLSM Confocal Laser Scanning Microscope

DNP 2,4-Dinitrophenol, an explosive

ELISA Enzyme-Linked Immunosorbent Assay

FITC Fluorescein Isothiocyanate, a fluorescein salt

HMDS Hexamethyldisilazane

IDT Interdigitated Transducer

IgG Immunoglobulin G

IL Insertion Loss

INEEL Idaho National Engineering and Environmental Laboratory

kDa kilo-Dalton, a unit of molecular weight

LCST Lower Critical Solution Temperature

NHS N-hydrocylsulfo-succinimide

NIPAAm N-Isopropylacrylamide, a monomer of hydrogel polymer

OFDM Orthogonal Frequency Domain Modulation

PPF Plasma Polymerized (Thin) Film

ppm, ppb parts per million, parts per billion

QAM Quadrature Amplitude Modulation

PR Photoresist

P-wave Primary wave (the 'first' to arrive at a seismic station), or Pressure wave

pI Isoelectric point

QCM Quartz Crystal Microbalance

RDX Royal Demolition Explosive (hexahydro-1,3,5-trinitro-1,3,5-triazine)

SAM Self-Assembled Monolayer

SAW Surface Acoustic Wave

SAWR Surface Acoustic Wave Resonator

SH-APM Shear Horizontal Acoustic Plate Mode

SH-SAW Shear Horizontal Surface Acoustic Wave

SLPM Standard Liters per Minute

SPA or SpA *Staphylococcal* Protein A

SSBW Surface Skimming Bulk Wave

STW Surface Transverse Wave

S-wave Secondary wave (arrives 'second' to the faster P-wave), or Shear wave

TAE Tris-Acetate-EDTA, a pH buffer

TCD Temperature Coefficient of Delay

TCE Trichloroethylene

SUMMARY

The object of this thesis research is to facilitate the appraisal and analysis of the signatures of the modern acoustic wave biosensors, as well as to improve the experimental methodology to enhance sensor performance. For this purpose, both theoretical characterization of acoustic wave sensor signatures and experimental studies for the most frequently used acoustic wave biosensors, the liquid phase QCM (quartz crystal microbalance) and the vapor phase SAW (surface acoustic wave) sensors, are presented. For the study of SAW vapor phase detection, the author fabricated different types of two-port SAW resonator sensors on quartz substrates and designed and performed a significant number of detection experiments. These were conducted both with calibrated or known target samples under laboratory conditions at Georgia Tech Hunt Lab and with samples of unknown concentrations such as seized crack cocaine (courtesy of Georgia Bureau of Investigation, GBI) to see the sensor's capability to work in the field conditions. In addition, the dependence of the SAW sensor signatures on specific locations of the surface perturbation was investigated to account for some observed abnormal responses. Finally, a novel approach to classify and visualize chemically analogous substances is introduced.

CHAPTER 1

INTRODUCTION

Acoustic wave devices have been in commercial use for more than 60 years, and have received increasing interest in recent years in a wide range of applications where they are currently used as resonators, filters, sensors, and actuators. The telecommunications industry is the largest market, where surface acoustic wave (SAW) filters are in high demand for mobile cell phones, base stations, and RF front ends for portable wireless devices. Due to their compact size and integrated circuit (IC) compatibility, SAW devices have been widely adopted in analog and digital communications. The operation of acoustic wave devices is based on the piezoelectricity which was discovered by brothers Pierre and Paul-Jacques Curie in 1880. Piezoelectricity refers to the production of electrical charges by the imposition of mechanical stress. The phenomenon is reciprocal; applying an appropriate electrical field to a piezoelectric material creates a mechanical stress which is termed *inverse* or *converse* piezoelectricity. Due to this coupling relationship between the mechanical and electrical properties, acoustic wave devices based on piezoelectric materials are used in numerous ways.

One of the emerging applications for acoustic wave devices is the sensor, which includes vapor, humidity, temperature, and mass sensors for industrial and commercial applications and biochemical sensors for medical applications. In piezoelectric acoustic wave sensors, one can apply an oscillating electric field to create a mechanical wave, which propagates through the substrate and is then converted back to an electric field for measurement. They can be mass-produced at a low price using semiconductor

microfabrication and photolithography techniques. A sensor, by definition, is a transducer that transforms a measurand quantity into a readable value such as voltage, current, or frequency. Acoustic wave devices coated with a biolayer represent one biosensor approach for the detection of biomolecules. Figure 1-1 shows a schematic of the acoustic wave based biosensor.

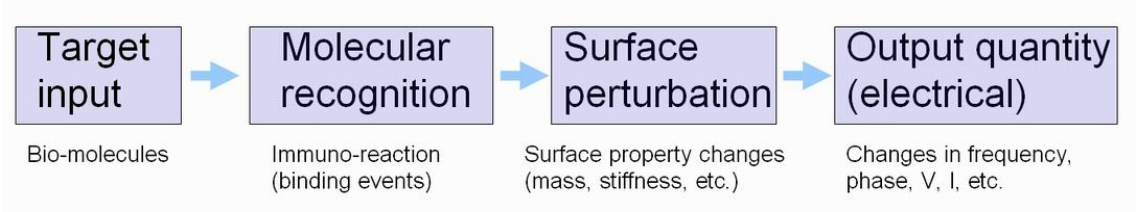

Figure 1-1. Overview of acoustic wave biosensor system

Generally, a biosensor is defined as an analytical device utilizing a biological sensing element incorporated to a transducer that converts the biochemical response into a quantifiable electric signal. Biosensors are finding uses in a broad range of applications including clinical diagnosis, biomedicine, food production and analysis, microbiology, pharmaceutical and drug analysis, pollution control and monitoring, for military and security applications, to name a few. The colloquial view of the term is that biosensors refer to devices that detect the presence of entities of biological origin, such as proteins or cells, and that this detection must take place in a 'liquid' phase. The author's previously published work [1,2,3], however, empirically demonstrated that an acoustic wave sensor with a properly immobilized biolayer need not be restricted to the detection of biomolecules, and that the detection environment can be a 'vapor' phase by making the surface 'semi-aqueous' using a hydrogel layer. Biosensors that incorporate an antibody–antigen interaction are termed immunosensors. They are based on the same principles as

conventional solid-phase immunoassays, such as enzyme linked immunosorbent assay (ELISA) with the antibody immobilized on a solid sensor surface. However, the conventional immunoassays require multistage processes, resulting in complex analysis procedures that require a skilled analyst. Also these procedures must be carried out under strict laboratory conditions. Modern acoustic immunosensors, on the other hand, are being developed to overcome such disadvantages by providing rapid detection, mobility, and ease of use. Immunosensors have wide applications since they can detect various substances from bacteria to environmental pollutants. The same principle could be applied to DNA sensing. Actually, the antibodies can be produced against a broad range of analytes for which the source animal can generate an immune response. This fact makes the range of detection targets virtually limitless.

In a typical application, the acoustic wave device is connected in an oscillator circuit, and the change in frequency (Δf), phase, voltage, or current resulting from a biomolecular event is recorded. Figure 1-2 presents a diagram of a SAW delay line device with a selective coating on it.

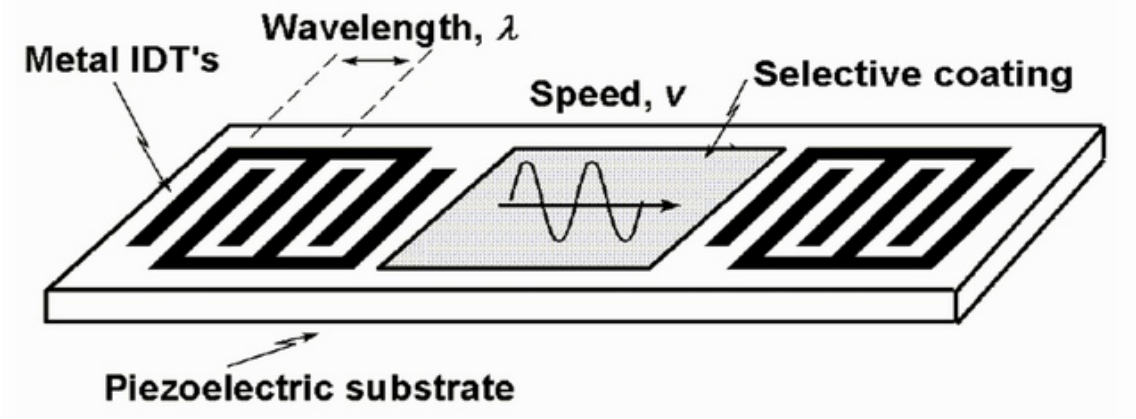

Figure 1-2. Configuration of a SAW delay line sensor

From an instrumentation standpoint, it has been argued that acoustic wave sensors in this oscillator configuration represent a highly advantageous approach to precise detection because the shifts in frequency are far easier to measure than equivalent perturbations in time delay, voltage, or current. For this reason, SAW devices in a resonator structure, rather than a delay line, are considered to be a better choice for high sensitivity detection [4]. This issue will be discussed later in chapter 5.

There are two key parameters for the biochemical sensor: selectivity and sensitivity. The sensitivity is prescribed by the sensor modality and design. Generally, the sensitivity of an acoustic wave sensor is proportional to the operating frequency and the amount of acoustic energy in the location where the sensing is done. Bulk acoustic wave sensors like QCM disperse the energy throughout the material, which can degrade the sensitivity. In SAW sensors, the acoustic energy is concentrated near the surface, tending to provide better sensitivity. Selectivity is the ability to respond only to the target molecule in the presence of other species. The degree of specificity is dependent on the detailed nature of the chemically sensitive film on the surface of the device. Extreme selectivity is obtained by the antibody-antigen reaction because an antibody binds only to a single substance, its antigen.

The contents of this dissertation consist of the theoretical overview of acoustic wave devices followed by a collection of the author's experimental work divided into categories. In chapter 2, a general description and theoretical background for acoustic wave devices typically used as biosensors are introduced. The physics of the various acoustic modes and the fundamental equations for sensor applications are reviewed. To evaluate molecular recognition signatures of modern biosensors and to account for the

observed deviations from the classic theories, a broad relationship has been developed from the complex reciprocity relation and time-dependent perturbation theory. Chapter 3 introduces several antibody immobilization techniques along with a novel fluorescence immunoassay that serves as visual confirmation of both the successful antibody immobilization and the sensor's detection ability. Beginning with chapter 4, a series of the author's representative acoustic wave immunosensor experimental data and results are introduced. In chapter 4, evidence of bacterial spore detection using a liquid phase QCM sensor are presented. In chapter 5, a design of a two-port SAW resonator is described, and vapor phase immunosensing experimental results using an array of two-port SAW resonator sensors are demonstrated. Chapter 6 discusses some practical aspects of SAW immunosensors by investigating the contributions of the sensor's local perturbation to the overall sensor signature. In chapter 7, a novel method to classify and visualize chemically similar molecules is proposed in which the concept of in-phase (I) and quadrature-phase (Q) domain for the detection of orthogonal M-ary signals in digital telecommunication systems theory is used. Finally, some general conclusions about the work presented and suggested work for the future are presented in chapter 8. The thesis work mainly focuses on and performed with SAW sensors. Unless otherwise stated, the design, fabrication, packaging (dicing and wire-bonding), and measurement of all the SAW devices used in this thesis research are conducted by the author in the Hunt Lab, Georgia Institute of Technology.

CHAPTER 2

ACOUSTIC WAVES FOR BIOSENSORS

2.1 Introduction

Acoustic wave devices are described by the mode of wave propagation through or on a piezoelectric substrate. The acoustic modes are distinguished primarily by their velocities and particle displacement directions; many combinations are possible, depending on the material and boundary conditions. It should be noted that solid acoustics is concerned with macroscopic phenomena as if the matter were a continuum [5]; it does not deal with atomic levels. Therefore, the term 'particle' in acoustics means an infinitesimal volume amount yet containing 'many atoms' moving in unison; it does not imply a single atom or a molecule in the microscopic level. Before discussing the details of each wave mode, it seems appropriate to review the definitions of typical acoustic waves and modes.

- **Longitudinal *vs.* shear wave**: In a longitudinal wave (a.k.a. compressional wave, p-wave), the particle motion (or polarization) is parallel to the direction of wave propagation, *i.e.*, particles are moving back and forth about their individual equilibrium positions along the wave propagating direction. A shear wave (a.k.a. s-wave, transverse wave) has particle motion perpendicular to the wave propagating direction. Shear waves can be further divided into shear horizontal (SH) and shear vertical (SV) waves. In this case, the terms vertical and horizontal are specified with reference to a particular boundary plane. Shear horizontal wave motion signifies in-plane polarization parallel to

the substrate surface; shear vertical motion indicates transverse polarization normal to the surface.

- **Quasi-shear and quasi-longitudinal**: Due to the anisotropic nature of the crystal substrate material, shear and longitudinal modes can be coupled. Such modes are called quasi-shear or quasi-longitudinal depending on whichever is dominant. For example, a Rayleigh wave is a quasi-shear wave because it has both longitudinal and shear components with the latter being dominant. The quasi-modes are excited when a wave is propagating in a direction with low crystal symmetry [6].
- **Bulk wave *vs.* surface wave**: In a bulk wave mode, the acoustic energy is distributed throughout the entire substrate or medium. Typical examples include the thickness shear mode (TSM) of QCM and acoustic plate mode (APM) which will be described later in this chapter. In a surface wave mode, the acoustic energy is concentrated close to the surface (roughly within one wavelength) and the amplitude decreases exponentially with increasing depth. Thanks to the energy confinement near the surface, surface waves are extremely sensitive to the external perturbation. The Rayleigh wave is representative of this category.
- **Pseudo-SAW (PSAW) or leaky-SAW (LSAW)**: With the discovery of new piezoelectric material and crystal cuts, several acoustic modes that resemble SAW but have slightly different characteristic have been reported. These modes are termed pseudo-SAW (PSAW) or leaky SAW (LSAW) in the sense that the acoustic energy in these modes typically leaks into the substrate. For example, a surface skimming bulk wave (SSBW) propagates close to the surface but penetrates into the substrate at a very small angle. Based on the fact that the sensitivity of an acoustic wave sensor is determined by

the degree of wave confinement, a leaky mode is not preferable for high sensitivity sensors over a pure SAW mode. For other applications than sensors, however, PSAW has several advantages over their pure SAW counterparts. For example, they have higher velocity, can handle larger power, and are less susceptible to surface contamination than Rayleigh wave devices do.

The propagation of acoustic waves in a solid medium can be described in terms of four variables: stress (**T**), strain (**S**), particle displacement (**u**), and particle velocity (**v**). These four variables require four equations to completely characterize the mechanical motions. For a plane wave propagating in the z-direction, these four equations are as follows.

- Two fundamental physical laws.

  Newton's law: $\frac{\partial T}{\partial z} = \rho \frac{\partial^2 u}{\partial t^2}$ (2.1)

  The definition of strain: $S = \frac{\partial u}{\partial z}$ (2.2)

- Two constitutive equations:

  Definition of particle velocity: $v = \frac{\partial u}{\partial t}$ (2.3)

  Hooke's law: T = c S (2.4)

where ρ is a mass density of the medium and c is a stiffness constant.

Based on these relationships, a one-dimensional wave equation can be derived. Combining (2.1) and (2.3) yields

$$\frac{\partial T}{\partial z} = \rho \frac{\partial v}{\partial t} \tag{2.5}$$

Differentiating (2.2) with respect to *t* gives

$$\frac{\partial S}{\partial t} = \frac{\partial^2 u}{\partial t \partial z} = \frac{\partial v}{\partial z} \tag{2.6}$$

Differentiating (2.5) with respect to *t*, (2.6) with respect to *z*, and applying (2.4) gives

$$\frac{\partial^2 T}{\partial z \partial t} = \rho \frac{\partial^2 v}{\partial t^2} \quad , \quad \frac{\partial^2 S}{\partial z \partial t} = \frac{\partial^2 v}{\partial z^2}, \quad \text{and}$$

$$\frac{\partial^2 v}{\partial t^2} = \frac{c}{\rho} \frac{\partial^2 v}{\partial z^2} \tag{2.7}$$

Equation (2.7) is the one dimensional wave equation, and the solution of (2.7) is a propagating wave with phase velocity

$$V_a = \sqrt{c / \rho} \tag{2.8}$$

The Hooke's law in (2.4) is for one-dimension only, but generally six components of stress and strain over the three-dimensional coordinates are defined. Therefore, stress and strain become second-order tensor quantities and the relationship can be expanded as follows

$$S_{ij} = \frac{1}{2}\left(\frac{\partial u_i}{\partial x_j} + \frac{\partial u_j}{\partial x_i}\right) \qquad i, j = 1, 2, 3 \text{ (1=x 2=y 3=z).} \tag{2.9}$$

$$T_{ij} = \sum_{k,l=1}^{3} c_{ijkl} S_{kl} \tag{2.10a}$$

where c_{ijkl} is now a fourth-rank tensor. Considering the symmetry of the strain and stress tensor (*i.e.*, $S_{ij} = S_{ji}$ and $T_{ij} = T_{ji}$), (2.10a) can be simplified to the Engineering or reduced notation

$$T_I = \sum_{J=1}^{6} c_{IJ} S_J \qquad (2.10b)$$

or more simply $\mathbf{T} = \mathbf{c} : \mathbf{S}$ (2.10c)

where the double dot (**:**) assumes summation over all the axial indices.

There are similarities between the variables in the acoustic wave guide and electromagnetic transmission lines. The field equations are expressed in the similar symbolic form and the solutions are analogous in all respects. Also, the constitutive equations of the electromagnetic and acoustic field can be converted to each other [5]. The analogies are summarized in the Table 2-1.

Table 2-1. Equivalent variables of EM transmission line and acoustic plane wave

EM transmission line parameters	**Acoustic plane wave field parameters**
V, voltage	-T, stress (negative)
I, current	v, particle velocity
v_s, source voltage	F, body force
L, inductance	ρ, mass density
C, capacitance	c^{-1}, inverse stiffness coefficient

2.2 Acoustic Wave Modes for Sensor Applications

2.2.1 Thickness Shear Mode (TSM)

Quartz crystal microbalances (QCM) a.k.a. thickness shear mode (TSM) resonators have been utilized since the 1950s to monitor the thickness of metals being deposited on wafers in evaporation systems. A QCM consists of a thin disk of AT-cut quartz with circular metal electrodes. The electrodes are typically thin (100 nm) layers of gold sputtered or evaporated onto both sides, and an alternating electric field is applied to induce a mechanical deformation by the piezoelectric effect; more exactly, the *inverse* piezoelectric effect. Figure 2-1 presents snapshots of piezoelectrically excited AT-cut quartz plate in a fundamental thickness shear mode. The polarization, or direction of elastic deformation of the particle, is parallel to the device surface, *i.e.*, there is no surface-normal component. The mechanical definition of fluids assumes that a shear wave cannot be supported by liquid, so only longitudinal stress can be transferred in a liquid. This means the acoustic energy of QCM is not lost into the liquid. This characteristic enables QCM to be a great candidate for a liquid phase sensor. It is well known that in cuts of quartz, such as the AT-cut used for QCM, the linear expansion of the material with varying temperature is compensated by changes in the acoustic velocity such that the round trip delay for an acoustic wave in a resonator does not vary with temperature, *i.e.* the temperature dependency of the resonant frequency is negligible.

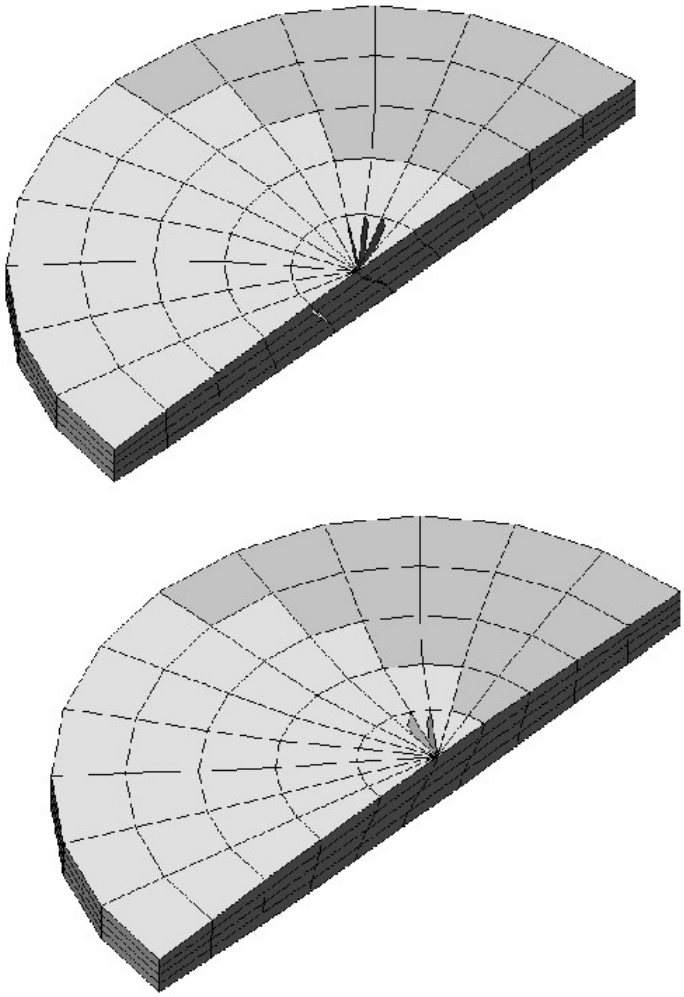

Figure 2-1. Simulation of a thickness shear vibration of the AT-cut quartz crystal plate when an alternating electric filed is applied by electrodes on both sides. (Electrodes are not shown.) Illustrations are captured from the animation at http://www.ieee-uffc.org

The governing equation for the QCM operation was empirically derived by Sauerbrey [7] in 1959.

$$\Delta f = -K f_0^{\,2} \frac{\Delta m}{A} \qquad (2.11)$$

where f_0 is the resonance frequency, K is a constant, and A is the sensing area. This is the fundamental equation for QCM-based sensors, but it can only be useful for a rigid film with negligible thickness and in a vacuum environment. Such restrictions give rise to significant deviations when the detection is done in the liquid phase.

In 1985, Kanazawa and Gordon [8] derived a similar relationship of QCM in contact with liquid.

$$\Delta f = -f_0^{\,3/2} (\eta\rho / \pi\mu_q \rho_q)^{1/2} \qquad (2.12)$$

where f_0 is again the resonance frequency, η and ρ are the viscosity and absolute density of the solution, respectively, and μ_q and ρ_q are the shear stiffness and density of the quartz crystal, respectively. This equation introduces the dependence of the viscosity of the medium, in addition to the mass.

From (2.11) and (2.12), it is predicted that a higher resonant frequency (f_0) improves the sensitivity. However, the resonant frequency of the QCM is limited by the thickness of the quartz substrate, resulting in a fundamental mode in the low MHz range. The resonant frequency of a thickness mode resonator based on its resonant condition can be found as

$$f = \frac{NV_a}{2d}, N = 1,3,5,\ldots \qquad (2.13)$$

where f is the resonant frequency, V_a is acoustic wave phase velocity (~3.34×10^3 m/sec for AT-cut quartz), and d is the substrate thickness.

For example, in order to realize a QCM with 100 MHz of fundamental *(N=1)* resonant frequency on AT-cut quartz, the thickness of the quartz substrate should be around 16 microns, which is obviously not practical. Typical operating frequency of QCM is in the range of 5-10 MHz with the substrate thickness around 0.2 mm for a 10 MHz operation.

2.2.2 Shear-Horizontal Acoustic Plate Mode (SH-APM)

Another type of acoustic mode that can be exploited in the liquid phase application is the shear-horizontal acoustic plate mode (SH-APM) which has been introduces in 1980's. SH-APM devices use a thin piezoelectric substrate, or plate, functioning as an acoustic waveguide that confines the energy between the upper and lower surfaces of the plate (see Figure 2-2).

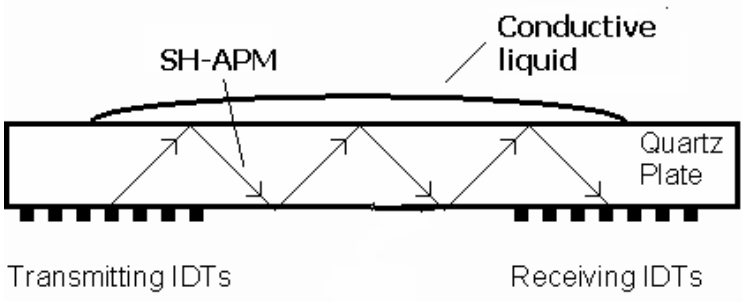

Figure 2-2. Sagittal plane of a Shear Horizontal Acoustic Plate Mode (SH-APM) sensor with a conductive liquid on top. Sensing is done on the non-transducer (non-metal) side of the device.

Technically, this mode can be termed as 'propagating TSM' in the sense that the polarization is parallel to the surface like the TSM, but the wave indeed travels, rather than forming a standing wave, from the transmitting IDT (interdigitated transducer) to the receiving IDT. Like the TSM resonator, the absence of a surface-normal component of wave displacement allows the sensor to be used in liquid for biosensor applications. In a SH-APM mode, both surfaces undergo displacement so the sensing can be done on either side. The obvious advantage of this is that one side containing the IDTs can be isolated from possibly conducting fluids or gases, while the other side can be used as the sensing area. SH-APM sensors have been successfully used to detect microgram-per-liter levels of mercury, which is adequate for Safe Drinking Water Act compliance testing [9]. Like the TSM, a disadvantage of this mode is that the acoustic energy is distributed throughout the substrate which lowers the sensitivity. The sensitivity to mass loading and other perturbations depends on the thickness of the substrate and can be increased if the device is thinned. In this case, however, the robustness will be compromised.

2.2.3 Rayleigh Surface Acoustic Wave (SAW)

In 1887, a British scientist Lord Rayleigh discovered that there is a unique mode of wave propagation in a solid in which acoustic energy is confined very near the surface and decays into the depth within a distance of the order of one wavelength. This is the definition of a SAW (surface acoustic wave) and the discovered wave is called a 'Rayleigh wave' after his name. Rayleigh waves launched on a quartz crystal have been employed for various sensor applications due to its high sensitivity to surface perturbation and its temperature stability. Chemical sensing is one of the major

applications of Rayleigh wave devices. In 1979, Wohltjen and Dessy first used SAW devices as a gas sensor. Thereafter, many researchers have been investigating the detection of vapor phase molecules with selective polymer coatings on Rayleigh SAW devices. Later on, their application extends to biosensors and immunosensors with the development of stable antibody immobilization techniques.

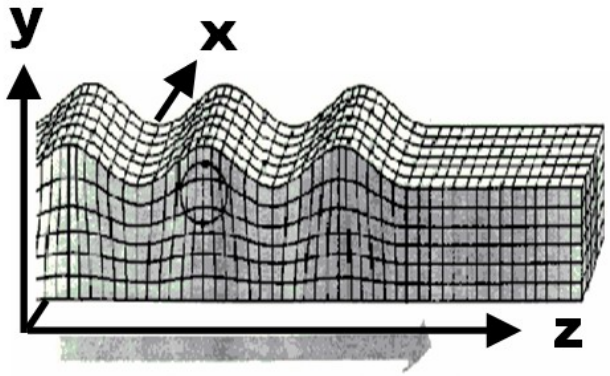

Figure 2-3. Surface deformation of a medium due to a Rayleigh wave propagation

The Rayleigh wave has elliptically rotating particle polarization with the foci located along the y-axis. The reason for the elliptical polarization, rather than circular, is related to the larger surface impedance in the medium than in the air; the particle is easier to move in the air (lower impedance) than in the medium (higher impedance). The characteristic of Rayleigh wave is similar to an ocean wave in that both are surface waves with an elliptical polarization (even the particle rotating directions are opposite near the surface), and neither has shear component along the transversal direction, *i.e.* in the x-axis in figure 2-3. It should be noted that the aforementioned definition of SAW does not include the particle polarization. Although the term 'SAW' generally refers to the Rayleigh wave, there are other SAW modes with substantially different particle polarizations from that of a Rayleigh wave. For example, a STW (surface transverse

wave) meets the SAW requirements, but the particle movement exists only in the x-direction. This acoustic mode is called a shear-horizontal SAW (SH-SAW). More details about SH-SAW are described in section 2.2.4 and 2.2.5.

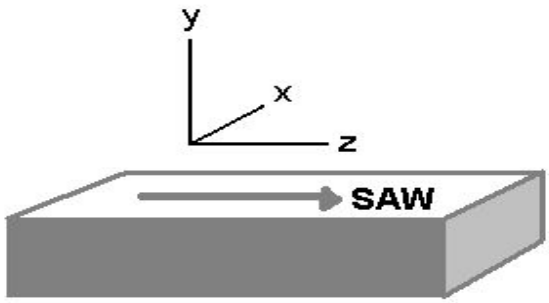

Figure 2-4. SAW propagating in the z-direction. A pure Rayleigh wave has no particle movement in the x-direction while a SH-SAW has particle movements only in the x-direction.

As discussed in section 2.1, the Rayleigh wave is not a pure shear wave. The elliptical nature of the particle motion indicates that a Rayleigh wave has both vertical shear (y) and longitudinal (z) components with no motion in the x-direction. If it were a pure shear wave, there would be no component in the z-direction. However, the dominating one is the vertical shear components. Therefore, it is reasonable to place a Rayleigh wave in the category of 'quasi-shear' wave which is defined in section 2.1.

SAW is most conveniently excited using an interdigital transducer (IDT) on a piezoelectric crystal such as quartz, lithium niobate ($LiNbO_3$), GaAs, and so on. The IDT, invented by White and Voltmer in 1965 [10], consists of two interweaved arrays of spatially periodic metallic electrodes on the surface of the piezoelectric substrate. The IDT provides the electric field necessary to displace the substrate by the inverse piezoelectric effect and thus form an acoustic wave. The wave propagates through the substrate where it is converted back to an electric field at the IDT on the other side by the

piezoelectric effect. Like QCMs, SAW sensors measure the changes in acoustic wave properties (phase shift, velocity change, attenuation, etc.) caused by the interaction of an acoustic wave with the target material in the selective biofilm area of the device. A mass-loading *vs.* frequency relationship analogous to the Sauerbrey equation of the QCM can be derived using the Tiersten formula (2.14) which describes the SAW velocity change resulting from the deposition of an acoustically thin film on the device surface.

$$\frac{\Delta V}{V} = -\omega h \left[c_1 \left(\rho - \frac{\mu}{V^2} \right) + c_2 \rho + c_3 \left(\rho - \frac{4\mu}{V^2} \cdot \frac{\lambda + \mu}{\lambda + 2\mu} \right) \right] \qquad (2.14)$$

where V is the SAW phase velocity, ω is the fundamental angular frequency of the device, h is the film thickness, ρ is the mass density of the film, and λ and μ are Lamé constants. The index c_i *(i=1,2,3)* is the SAW-film coupling parameter related to the particle velocity in each direction (*1=x, 2=y, 3=z*), and should not be confused with the stiffness **c** in the Hooke's law. Because the wavelength of the device is fixed by lithography, the left-hand side of equation (2.14) can be replaced by the frequency ratio, $\Delta f / f$. Thus, (2.14) becomes

$$\Delta f = -2\pi f^2 h \left[c_1 \left(\rho - \frac{\mu}{V^2} \right) + c_2 \rho + c_3 \left(\rho - \frac{4\mu}{V^2} \cdot \frac{\lambda + \mu}{\lambda + 2\mu} \right) \right]$$

$$= -2\pi (c_1 + c_2 + c_3) h \rho f^2 + 2\pi c_1 h f^2 \frac{\mu}{V^2} + 2\pi c_3 h f^2 \frac{4\mu}{V^2} \cdot \frac{\lambda + \mu}{\lambda + 2\mu} \qquad (2.15)$$

Because the particle polarization of the Rayleigh wave is elliptical on the *y*-*z* plane and has no component in the *x*-direction, c_1 =0. Letting c_1 =0 in (2.15) yields

$$\Delta f = (A_2 + A_3)\rho h f^2 - A_3 h f^2 \left(\frac{4\mu}{V^2} \cdot \frac{\lambda + \mu}{\lambda + 2\mu} \right) \quad (2.16)$$

where A_2 = -2πc_2 and A_3 = -2πc_3 now become material constants for the substrates. The first term in the right side of (2.16) is the frequency shift resulting from mass loading (ρ) and the second term describes the effect of changes in the elastic property (*i.e.* shear modulus, μ) of the film. Assuming the coating is soft, the second term can be negligible. Then, (2.16) can be simply reduced to

$$\Delta f = (A_2 + A_3)\rho h f^2 \qquad (2.17)$$

Because the density-height (ρ*h*) product is equivalent to mass per unit area (*m/A*), equation (2.17) is analogous to the Sauerbrey equation (2.11).

In the case of SAW with a shear horizontal polarization such as a STW, c_2 and c_3 in (2.15) become zero because the particle movement is only in the *x*-direction. Then, (2.15) becomes

$$\Delta f = A_1 \rho h f^2 - A_1 h f^2 \left(\frac{\mu}{V^2} \right) \qquad (2.18)$$

Similarly, if the mass loading effect dominates and the elastic term can be assumed to be negligible, the second part of (2.18) vanishes and the resulting equation is again in the similar form to the Sauerbrey equation (2.11) with different constant *K'*.

$$\Delta f = -K' f_0^{\,2} \frac{\Delta m}{A} \qquad (2.19)$$

The evaluated value of the constant *K'* is 2.3 for the QCMs and 1.26 for the ST-cut SAW resonators [11]. The larger coefficient *K'* (nearly a factor of 2) of the QCM does not indicate that QCM has better mass sensitivity because the operating frequency (f_o) of the SAW device is much higher (usually a factor of 10) than that of a QCM.

2.2.4 Surface Skimming Bulk Wave (SSBW)

Rayleigh wave resonators can be used for a variety of gas phase sensors that are very sensitive, small and easy to fabricate. These sensors measure the changes in acoustic wave properties such as phase shift, velocity change, and attenuation caused by the interaction of an acoustic wave with the target material in the selective biofilm area of the device. In the application of liquid phase detection, however, the Rayleigh type sensors are not suitable since the energy is lost into the liquid. For a certain cut of piezoelectric crystal, there exists an acoustic mode that has shear horizontal particle polarization and propagates at an angle from the surface as shown in figure 2-5. This acoustic mode is called Surface Skimming Bulk Wave (SSBW) and was first discovered by Lewis in 1977 [12].

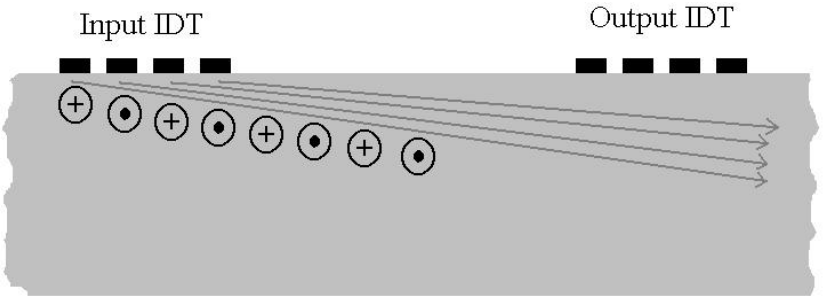

Figure 2-5. Side view diagram of a SSBW. The SSBW propagation angle is exaggerated.

Using a grating structure on the surface, this mode can be converted to a shear horizontal SAW (SH-SAW) or Surface Transverse Wave (STW) [13] which will be discussed in the next section. A SSBW can be generated on a rotated-Y cut crystal quartz substrate using a similar transducer structure that can be used to generate Rayleigh waves. Figure 2-6 represents the quartz cut angles and major characteristics of acoustic mode available from each orientation. As shown in figure 2-6, the SSBW mode exists both on ST-cut and AT-cut quartz.

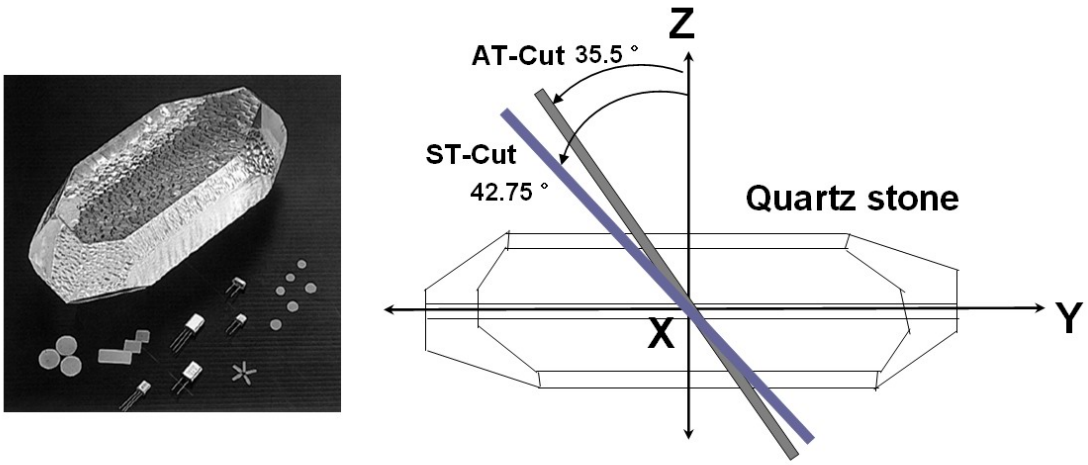

	Propagating direction	Acoustic mode	Wave velocity
ST-cut	X	Rayleigh wave	3158 m/sec
ST-cut	⊥ to X	SSBW	4990 m/sec
AT-cut	⊥ to X	SSBW	5099 m/sec

Figure 2-6. The orientation (cut angle) of quartz substrates and the characteristics of possible acoustic modes.

Another interesting fact is that the ST-cut quartz can support both Rayleigh and SSBW modes by simply changing the propagating direction by 90 degrees; the propagating direction is in the X-direction for Rayleigh wave, and perpendicular to the X-

direction for SSBW. Figure 2-7 shows the orientations for Rayleigh and SSBW mode on ST-cut quartz. One should not be confused between the capitalized X, Y, Z in the figure 2-6 and the lowercase x, y, z in figure 2-3 or 2-4. The former indicate the crystallographic axes which are a characteristic of a crystal, and cannot be modified. The latter are just dummy indices indicating the coordinates. This is a standard notation used in crystallography and the author will conform to this notation throughout the thesis.

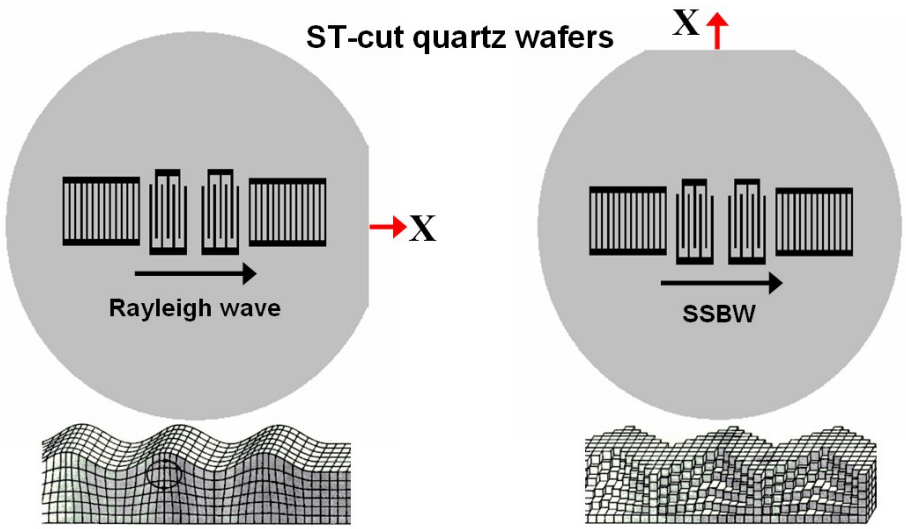

Figure 2-7. Two acoustic modes on ST-cut quartz. Both Rayleigh wave and SSBW can be excited on a ST-cut quartz wafer .

The acoustic wave velocity of a SSBW is known to be about 60% faster than that of a Rayleigh wave. Thus using the same lithography resolution and geometry, the center frequency of a SSBW is 1.6 times higher than that of a Rayleigh wave. To verify this, the author fabricated identical SAW resonators on two ST-cut quartz wafers; one with propagation direction perpendicular to the X-axis to generate a Rayleigh wave and the other parallel to the X-axis to excite a SSBW, as in figure 2-7. A 250-MHz two-port

Rayleigh SAW resonator photomask was used for the fabrication. The fabricated devices were probe-tested and the transmission scattering parameter (S_{21}) measurements are shown in figure 2-8.

The frequency response data in figure 2-8 verifies that the SSBW mode has a center frequency at 396 MHz, which is about 1.6 times higher than 250 MHz. The reason for higher insertion loss in SSBW mode (~28 dB compared to 12 dB in Rayleigh mode) is associated with the diffraction of acoustic waves into the bulk, which is a characteristic of a SSBW. To minimize the wave propagation into the substrate, an energy trapping structure should be employed, which will be described in the next section. The piezoelectric coupling of a SSBW is slightly stronger (larger K^2) than a Rayleigh wave on a quartz substrate, but the temperature coefficient is no longer zero at room temperature [14]. This characteristic of SSBW necessitates additional temperature compensation in the sensor applications. One simple method is to employ a reference sensor that is subjected to the same temperature environment as the sensor under test. The significance of a reference sensor will be discussed in chapter 5.

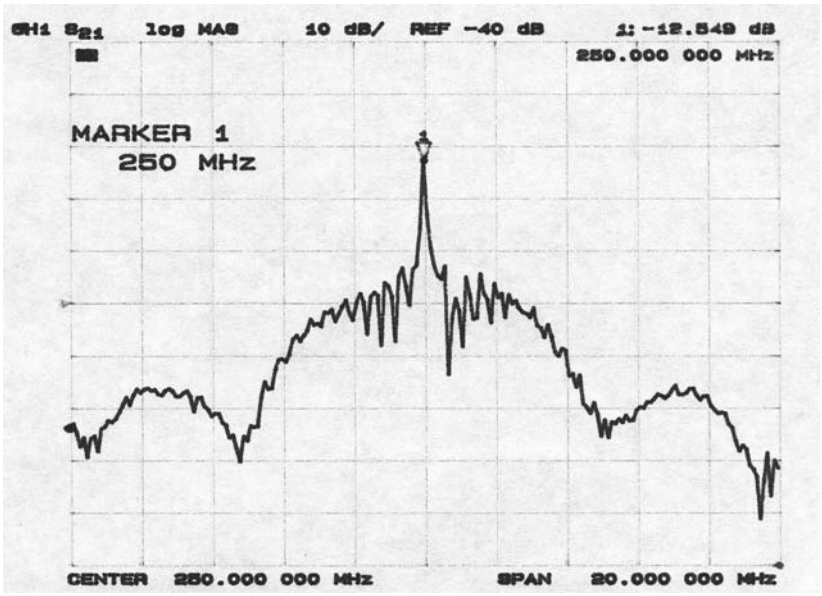

(a)

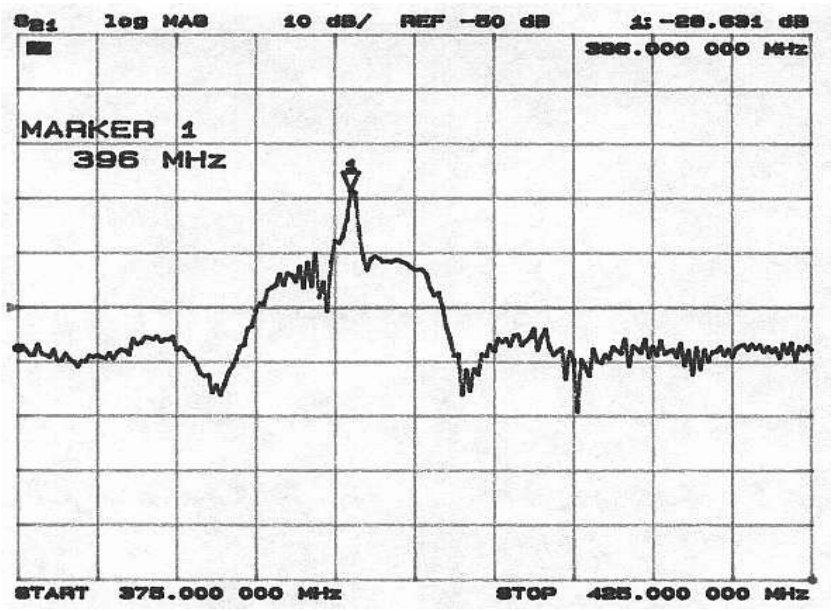

(b)

Figure 2-8. $|S_{21}|$ measurement of Rayleigh(a) and SSBW(b) resonator fabricated on a ST-cut quartz wafer using the same photomask. About 60% increase of the center frequency is observed from a SSBW device.

2.2.5 Surface Transversal Wave (STW)

A Rayleigh wave sensor provides very high sensitivity due to its inherent characteristic of confining all of the acoustic energy within a wavelength from the surface. The sensitivity of an acoustic wave sensor is proportional to the degree of wave confinement. In the case of SSBW, the acoustic energy propagates at an angle from the surface, which results in loss at the output transducer. Using a simple grating structure [13] the acoustic energy of SSBW can be lifted up close to the surface as in figure 2-9. This is called STW or SH-SAW.

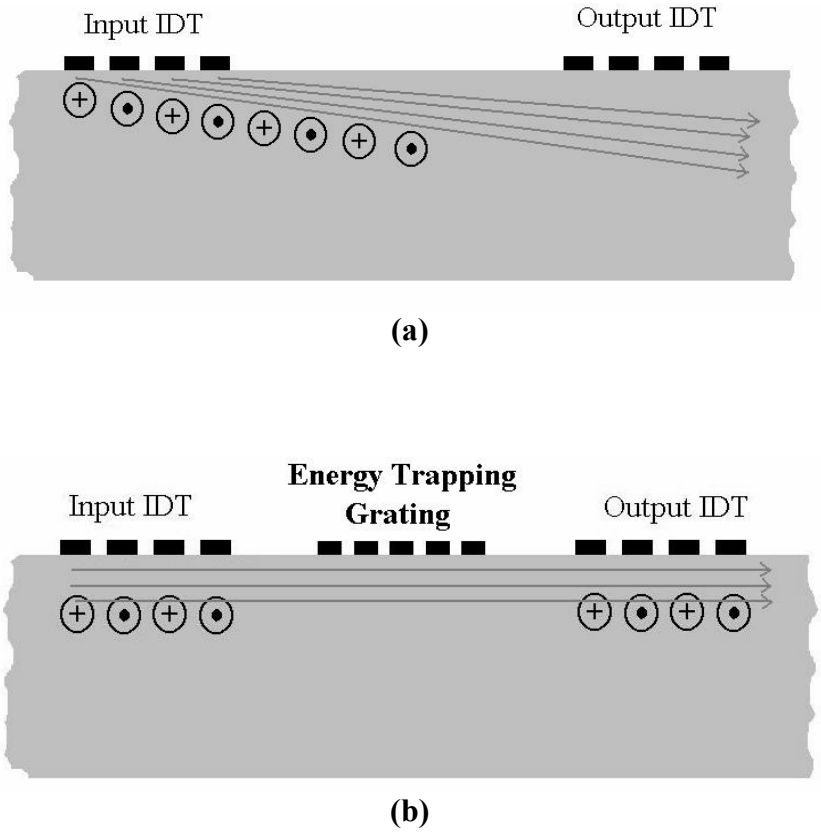

Figure 2-9. Sagittal plane of shear horizontal acoustic wave device. (a) Propagation of a SSBW. (b) The SSBW is converted to a STW by employing an energy trapping grating between the IDTs.

The main mechanism of SSBW being trapped in the surface region is as follows: First, there is a mass loading effect on the substrate by the grating fingers. The wave then slows down in the grating region due to the mass loading. The acoustic wave tends to flow to where the velocity is slower, so the energy is confined in near the grating area. The metal fingers also short the electric field at the substrate-metal interface, which is another reason for slowing down the acoustic velocity. In the case of weak piezoelectric materials such as quartz, however, the mass loading effect dominates and the piezoelectric shorting effect can be negligible.

The period of the energy-trapping grating is usually designed slightly less (~96%) than the IDT or reflector grating pitch [15], otherwise the transducer will *see* the grating as a reflector and a significant amount of the wave is bounced back to the transducer. The period of the center grating, however, should be close enough to that of the IDT and reflector to maintain homogeneity throughout the surface. Alternatively, a large difference in the periodicity will also cause wave reflection due to the surface impedance mismatch along the wave propagating path. By employing the center grating, the acoustic energy is confined in the vertical direction as well as in the horizontal direction by the reflectors. Energy trapping in the transversal (the *x*-axis in figure 2-4) direction need not be considered because there is no energy flow in that direction. Due to the confinement of the acoustic energy near the surface, STW shows higher mass sensitivity than that of a SSBW and the lack of surface normal particle motion enables a STW to be utilized in liquid phase biosensor applications. For example, detection of human Immunoglobulin G (IgG) using a 250-MHz STW device with a detection limit of 0.2 ng/cm^2 was reported [16].

Figure 2-10 shows a computer simulation (a) and the actual S_{21} measurement (b) of a 250 MHz SH-SAW resonator fabricated by the author. The simulation program has been developed and released by Hashimoto [17] at Chiba University, Japan. It is based on the coupling of mode (COM) theory which is accurate and one of the most frequently used tools for the simulation and analysis of SAW resonator devices. The small difference (~ 2 dB) in the insertion loss between the two results is from the fact that the energy trapping grating is not considered in the simulation program, *i.e.*, figure 2-10 (a) is actually a SSBW. The device in figure 2-10 (b) has the center grating that might have converted the SSBW mode in figure 2-10 (a) to the STW mode. The severe ripple beyond the center frequency is due to the reflection of a faster shear horizontal bulk wave excitation which occurs coherently with SSBW.

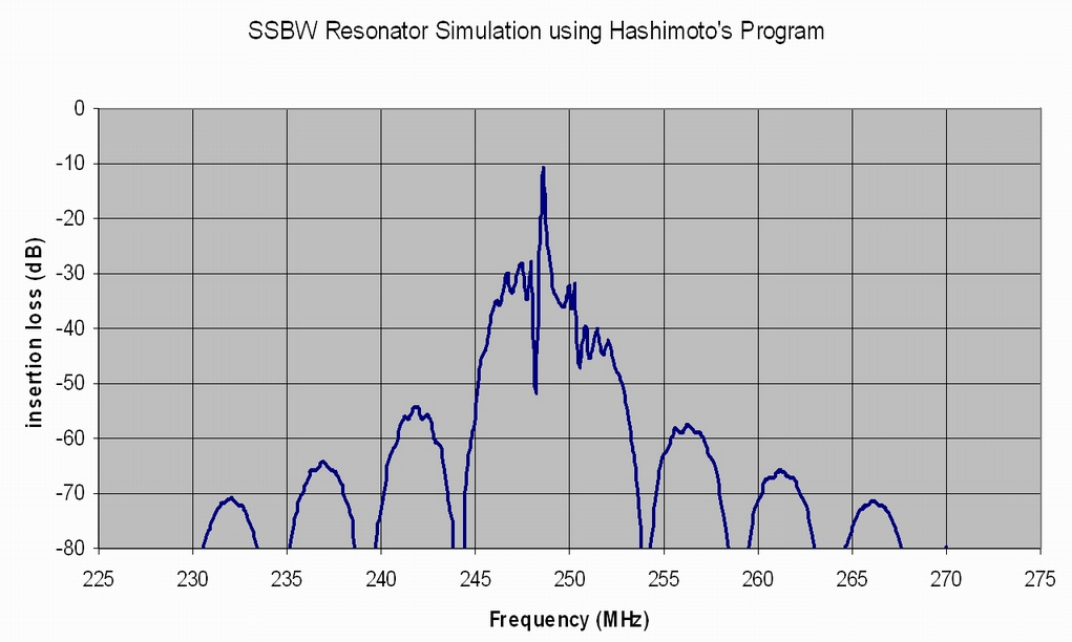

(a)

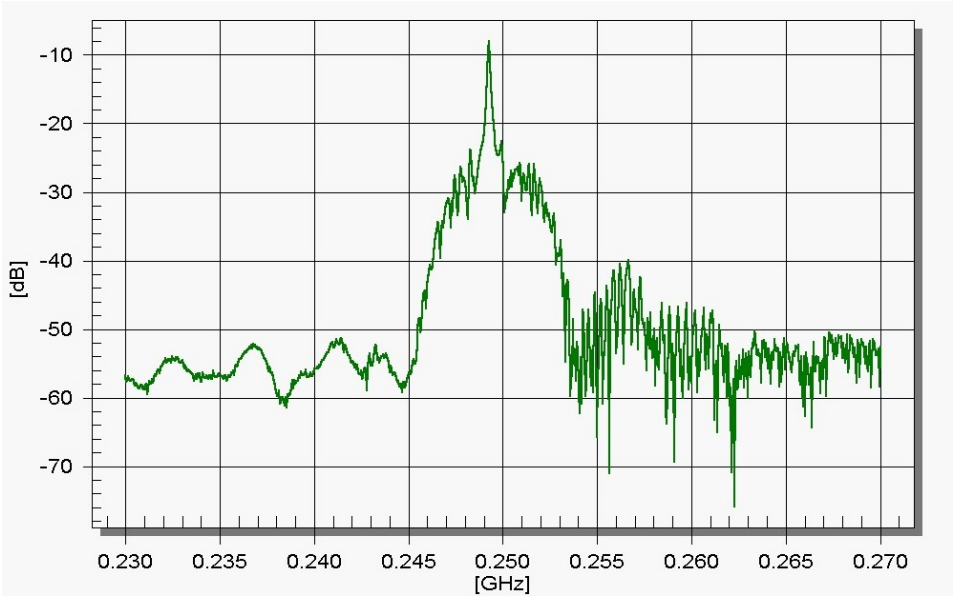

(b)

Figure 2-10. Frequency characteristic of shear horizontal waves on ST-cut quartz (a) simulation result of a 250-MHz SSBW resonator without the center grating considered. (b) Actual S_{21} parameter measurement of the fabricated resonator with the energy trapping grating included.

2.3 Substrate Material Considerations

The operating characteristics of devices based on acoustic waves are essentially determined by the piezoelectric substrate material. The material choice is the most basic consideration, involving a trade-off between insertion loss, coupling efficiency and temperature stability. The most commonly used piezoelectric substrate materials for sensor applications are quartz, lithium niobate, and lithium tantalate. Their major characteristics are compared in Table 2-2.

In spite of the low electromechanical coupling coefficient (K^2), the ST-cut quartz is frequently used for Rayleigh wave sensor applications because it provides outstanding temperature stability. It is known that ST-cut quartz has a temperature coefficient of delay (TCD) of zero at room temperature range [18].

Table 2-2. Physical parameters of commonly used piezoelectric crystals

Material	Quartz	Lithium Niobate	Lithium Tantalate
Orientation (crystal cut)	ST	Y	Y
Direction of Propagation	X	Z	Z
SAW Velocity (m/sec)	3158	3488	3230
SAW coupling (K^2) (%)	0.16	5	0.9
Relative Permittivity (ε_r)	4.5	46	47
Temperature Coefficient (ppm/° C)	**0**	94	35

One of the obvious advantages of the zero TCD is that it virtually eliminates the necessity for temperature compensation circuitry that can cause additional noise to the system. However, in the case of SAW resonator structures, low electromechanical

coupling becomes an issue when a small device size is desired. Unlike an electromagnetic wave which can be totally reflected using a metal plate, reflection of an acoustic wave requires multiple numbers of periodically spaced metal strips where the contribution of each strip's reflection adds constructively to yield higher reflectivity. The number of metal strips required to achieve a near total acoustic reflection depends on the degree of electromechanical coupling. In high K^2, *e.g.* strong piezoelectric material substrate such as lithium niobate, the total reflection ($|R| \sim 1$) is achieved with fewer numbers of metal strips than in a weak piezoelectric material like quartz. To verify this, the author fabricated identical two-port SAW resonators both on ST-cut quartz and lithium niobate substrates. The SAW resonator in this design originally had 500 metal strips on either side of the reflector grating, but the reflectors on the lithium niobate resonators were intentionally cut in half, resulting in roughly 250 strips for each reflector. Both the quartz and lithium niobate resonators had two split-fingered IDTs with 200 metal strips on each. Metallization was accomplished with an Al film with a thickness of 0.15 μm. Because the reflectors occupy the greatest area on a SAW resonator structure, the lithium niobate resonator herein is about half the size of the quartz resonator. The frequency response measurement is shown in figure 2-11. Despite the reduced number of reflector fingers, the two sample resonators on lithium niobate show a much lower insertion loss than the quartz resonator does. This is due to its strong (~30 times higher than quartz) electromechanical coupling coefficient. It is reported that a few hundred reflector strips can yield a total reflection for the lithium niobate, but theoretically about thousand fingers are required for the ST-quartz substrate [14]. In terms of the device size consideration, this is one good reason SAW resonators on quartz substrate should operate

in high frequencies because the spacing between the reflector fingers is inversely proportional to the operating frequency. For sensor applications, however, the temperature stability is more important and in many practical cases the quartz is chosen for the substrate material. Although the reflector with 500 grating fingers in the author's ST-quartz SAW resonator design cannot yield total reflection, this does not seriously degrade the sensor performance. Furthermore, it makes the device size realistic (1.9 mm x 8 mm) and fit to the commonly used TO-8 packages.

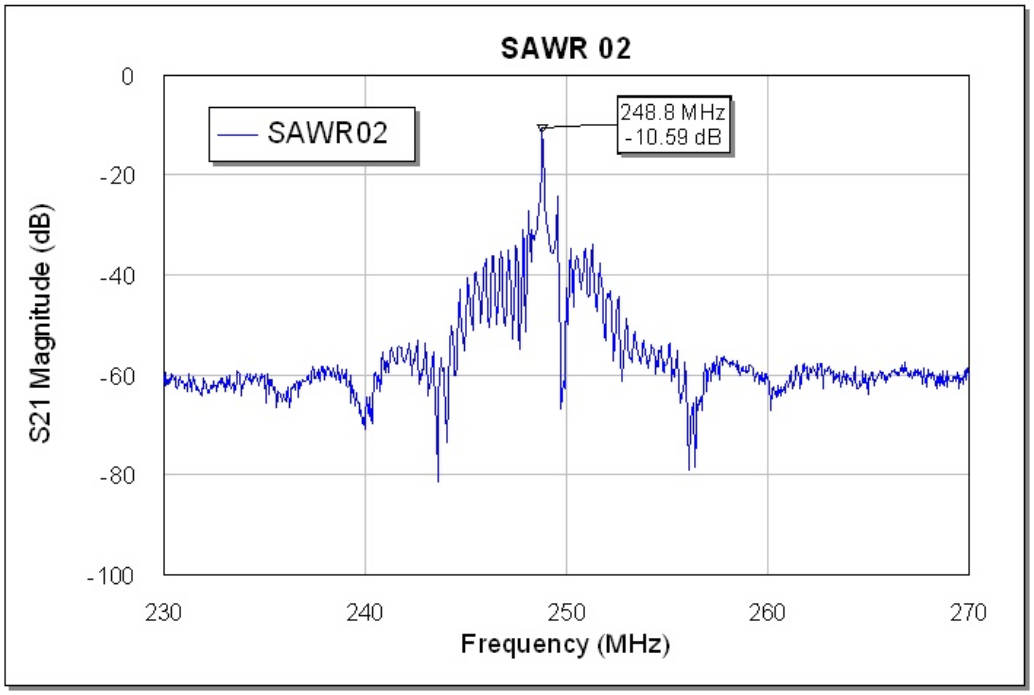

(a)

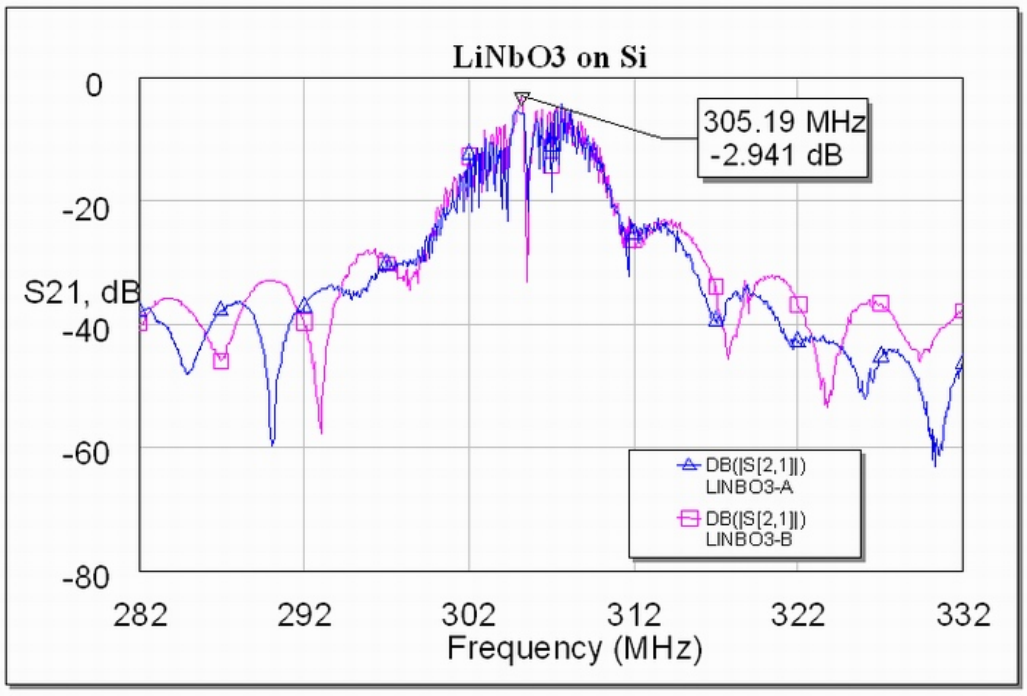

(b)

Figure 2-11. Frequency response of SAW resonators fabricated on (a) ST-cut quartz with 500 reflector fingers and (b) lithium niobate with 250 reflector fingers

2.4 Deviations from the Classic Theories

2.4.1 Background and Motivations

The sensing mechanism of an acoustic wave sensor, in general, is based on perturbation of the sensor surface when detection occurs, leading to a change in the resonant frequency. The perturbation arises from a mass adsorbed to the sensor surface and/or changes of physical properties of the contacting medium. The behavior of the sensor response can be predicted and explained by the famous mass-loading relationship developed by Sauerbrey (1959) and Kanazawa (1985) respectively. As the coating layer becomes complex, *e.g.* coated with an antibody layer and/or other biomolecules, it is observed that the profile of the sensor response deviates from the classic theories.

It is the author's experience that the most frequently occurring anomaly was the positive frequency shift when the target is captured. This phenomenon cannot be explained by classic mass loading theory unless a concept of "negative mass" is introduced which is not practical. Such a positive frequency shift has been reported by several research groups [19, 20], but detailed analyses of underlying mechanism are scarcely found in the current literature. In this section, the author theoretically investigates the factors that must be considered to understand the deviations from the classic theories.

2.4.2 Modal Analysis and Complex Reciprocity Relation

The analysis of waves in a waveguide structure, such as the quartz substrate of SAW or QCM, with a thin film overlay can be accomplished using the technique of modal analysis. It is possible to expand an arbitrary waveguide field distribution as a

superposition of an infinite number of waveguide modes. As long as the set of modes is mathematically complete, it is assumed that the individual modes must be orthogonal in the same sense that the sine and cosine functions in the Fourier series expansion are orthogonal to each other. In a set of partial differential equations that characterize a physical field in a waveguide or resonator structure, there exists a relation called 'complex reciprocity' between any two possible solutions to the field equations [21]. For this specific case these two solutions can be 'perturbed' and 'unperturbed' acoustic fields. Combined with the time-dependent perturbation theory, an analytical relationship has been derived that can be used to evaluate molecular recognition signatures in modern biosensors [22]. This derivation begins with the complex reciprocity relation.

Consider a lossless transmission line with propagation in the z-direction. A differential form of the transmission line equation can be expressed as

$$\frac{\partial V}{\partial z} = -L\frac{\partial I}{\partial t} + v_s \text{ and } \frac{\partial I}{\partial z} = -C\frac{\partial V}{\partial t} \qquad (2.20)$$

where v_s is the source voltage.

To obtain the complex reciprocity relation, assume the two possible solutions of (2.20), (V_1, I_1, v_{s1}) and (V_2^*, I_2^*, v_{s2}^*), where the latter is a complex conjugation of the solution (V_2, I_2, v_{s2}). Now the complex transmission line reciprocity relation can be obtained as follows:

$$\frac{\partial}{\partial z}(I_2^* V_1 + I_1 V_2^*) = -\frac{\partial}{\partial t}(LI_2^* I_1 + CV_2^* V_1) + I_2^* v_{s1} + I_1 v_{s2}^* \qquad (2.21)$$

Now let the solutions 1 and 2 (denoted by subscripts in Eq. 2.21) be the perturbed and unperturbed solutions respectively. Using the electromagnetic transmission line *vs*. acoustic plane wave analogy in section 2.1 and Table 2-1, one can replace the electromagnetic variables in (2.21) with the equivalent acoustic field parameters and expand the relation in 3-dimensions. This would give [21]

$$\nabla\cdot\left\{-\mathbf{v}_u^*\cdot\mathbf{T}_p-\mathbf{v}_p\cdot\mathbf{T}_u^*+\Phi_u^*\frac{\partial\mathbf{D}_p}{\partial t}+\Phi_p\frac{\partial\mathbf{D}_u^*}{\partial t}\right\}=$$
$$-\frac{\partial}{\partial t}\left(\begin{bmatrix}\mathbf{v}_u^* & \mathbf{T}_u^* & -\nabla\Phi_u^*\end{bmatrix}\begin{bmatrix}\rho & 0 & 0\\ 0 & :\mathbf{s}:^E & :\mathbf{d}\cdot\\ 0 & \cdot\mathbf{d}: & \cdot\boldsymbol{\varepsilon}\cdot^T\end{bmatrix}\begin{bmatrix}\mathbf{v}_p\\ \mathbf{T}_p\\ -\nabla\Phi_p\end{bmatrix}\right)+\left(\mathbf{v}_u^*\cdot\mathbf{F}_p+\mathbf{v}_p\cdot\mathbf{F}_u^*\right)+\Phi_u^*\frac{\partial\rho_{ep}}{\partial t}+\Phi_p\frac{\partial\rho_{eu}^*}{\partial t} \tag{2.22}$$

Equation (2.22) is the general acoustic complex reciprocity relation. Because the derivation involves too many variables, it would be helpful to summarize some variables and notations before proceeding to further derivations. They are listed in Table 2-3. The use of these variables is consistently repeated in other chapters or sections throughout this thesis.

Table 2-3. Summary of the frequently used acoustic and electromagnetic variables

Variables	Definition
v	Particle velocity vector
T, S	Stress and strain tensors, respectively
F	External body force tensor
Φ	Electrostatic potential
D	Electric field displacement vector
d	Piezoelectric strain matrix
$\boldsymbol{\varepsilon}^T$	Dielectric permittivity matrix measured in constant stress field
s, c	Compliance and stiffness matrix, respectively
ρ	Mass density of substrate or film depending on subscripts
ρ_e	Volume density of mobile charge carrier
V_s	Phase velocity of acoustic wave
Subscript *p, u*	Denotes variable of the perturbed and unperturbed field respectively

Note: variables in bold indicate matrix, tensor, or vector quantities

2.4.3 Derivation of a New Relation Using the Perturbation Theory

Some of the variables in (2.22) can be eliminated in many practical cases. The perturbation analysis begins with the complex reciprocity relation with the added assumption that there is no external body force, thus the body force term **F** is eliminated. In the case of weak piezoelectric materials like quartz, the mechanical perturbation (*e.g.* mass loading or stiffness change) dominates and the effect of electrostatic potential and mobile charge carrier can be neglected. The sensor system described in this thesis

research employs a reference sensor that is supposed to cancel out non-significant perturbations, such as viscosity changes and surface conductivity changes due to ions in the contacting medium. These conditions further eliminates the terms related to the electrostatic potential, electric displacement, and charge density. As a result, the equation (2.22) is simplified to

$$\nabla \cdot \left(-\mathbf{v}_u^* \cdot \mathbf{T}_p - \mathbf{v}_p \cdot \mathbf{T}_u^* \right) = -\frac{\partial}{\partial t} \left(\begin{bmatrix} \mathbf{v}_u^* & \mathbf{T}_u^* \end{bmatrix} \begin{bmatrix} \rho & 0 \\ 0 & :\mathbf{s}:^E \end{bmatrix} \begin{bmatrix} \mathbf{v}_p \\ \mathbf{T}_p \end{bmatrix} \right) \tag{2.23}$$

For the material parameters associated with the biofilm, which are ρ and $\mathbf{s}^E$, it is necessary to separate terms into perturbed and unperturbed cases. After separating ρ and $\mathbf{s}^E$,the right side of (2.23) becomes

$$-\left\{ \frac{\partial}{\partial t} \left(\begin{bmatrix} \mathbf{v}_u^* & \mathbf{T}_u^* \end{bmatrix} \begin{bmatrix} \rho_u & 0 \\ 0 & :\mathbf{s}_u:^E \end{bmatrix} \begin{bmatrix} \mathbf{v}_p \\ \mathbf{T}_p \end{bmatrix} \right) + \begin{bmatrix} \mathbf{v}_u^* & \mathbf{T}_u^* \end{bmatrix} \frac{\partial}{\partial t} \left(\begin{bmatrix} \rho_p & 0 \\ 0 & :\mathbf{s}_p:^E \end{bmatrix} \begin{bmatrix} \mathbf{v}_p \\ \mathbf{T}_p \end{bmatrix} \right) \right\} \tag{2.24}$$

Note that unperturbed parameters are time-independent with resonant frequency ω_u and perturbed parameters are varying with time with resonant frequency ω_p. Expanding (2.24) yields

$$
\begin{aligned}
&-j\omega_u\begin{bmatrix}\mathbf{v}_u^* & \mathbf{T}_u^*\end{bmatrix}\begin{bmatrix}\rho_u & 0\\ 0 & :\mathbf{s}_u:^E\end{bmatrix}\begin{bmatrix}\mathbf{v}_p\\ \mathbf{T}_p\end{bmatrix}-j\omega_p\begin{bmatrix}\mathbf{v}_u^* & \mathbf{T}_u^*\end{bmatrix}\begin{bmatrix}\rho_p & 0\\ 0 & :\mathbf{s}_p:^E\end{bmatrix}\begin{bmatrix}\mathbf{v}_p\\ \mathbf{T}_p\end{bmatrix}\\
&-jt\frac{\partial\omega_p}{\partial t}\begin{bmatrix}\mathbf{v}_u^* & \mathbf{T}_u^*\end{bmatrix}\begin{bmatrix}\rho_p & 0\\ 0 & :\mathbf{s}_p:^E\end{bmatrix}\begin{bmatrix}\mathbf{v}_p\\ \mathbf{T}_p\end{bmatrix}-\begin{bmatrix}\mathbf{v}_u^* & \mathbf{T}_u^*\end{bmatrix}\begin{bmatrix}\dfrac{\partial\Delta\rho}{\partial t} & 0\\ 0 & \dfrac{\partial:\Delta:\mathbf{s}:^E}{\partial t}\end{bmatrix}\begin{bmatrix}\mathbf{v}_p\\ \mathbf{T}_p\end{bmatrix}
\end{aligned}
\tag{2.25}
$$

where Δ is the difference between perturbed and unperturbed quantities (*e.g.* $\Delta\rho = \rho_p - \rho_u$ and so on).

For convenience, let $\Re = \begin{bmatrix}\mathbf{v}_u^* & \mathbf{T}_u^*\end{bmatrix}\begin{bmatrix}\Delta\rho & 0\\ 0 & :\Delta\mathbf{s}:^E\end{bmatrix}\begin{bmatrix}\mathbf{v}_p\\ \mathbf{T}_p\end{bmatrix}$, then (2.25) can be written as

$$
\begin{aligned}
&-j\Delta\omega\begin{bmatrix}\mathbf{v}_u^* & \mathbf{T}_u^*\end{bmatrix}\begin{bmatrix}\rho_u & 0\\ 0 & :\mathbf{s}_u:^E\end{bmatrix}\begin{bmatrix}\mathbf{v}_p\\ \mathbf{T}_p\end{bmatrix}-j\omega_u\Re-jt\frac{\partial\Delta\omega}{\partial t}\begin{bmatrix}\mathbf{v}_u^* & \mathbf{T}_u^*\end{bmatrix}\begin{bmatrix}\rho_u & 0\\ 0 & :\mathbf{s}_u:^E\end{bmatrix}\begin{bmatrix}\mathbf{v}_p\\ \mathbf{T}_p\end{bmatrix}\\
&-jt\frac{\partial\Delta\omega}{\partial t}\Re-\begin{bmatrix}\mathbf{v}_u^* & \mathbf{T}_u^*\end{bmatrix}\begin{bmatrix}\dfrac{\partial\Delta\rho}{\partial t} & 0\\ 0 & \dfrac{\partial:\Delta:\mathbf{s}_p:^E}{\partial t}\end{bmatrix}\begin{bmatrix}\mathbf{v}_p\\ \mathbf{T}_p\end{bmatrix}
\end{aligned}
\tag{2.26}
$$

and the complex reciprocity relation (2.23) becomes

$$
\begin{aligned}
&\nabla\cdot\left(-\mathbf{v}_u^*\cdot\mathbf{T}_p-\mathbf{v}_p\cdot\mathbf{T}_u^*\right)=-j\Delta\omega\begin{bmatrix}\mathbf{v}_u^* & \mathbf{T}_u^*\end{bmatrix}\begin{bmatrix}\rho_u & 0\\ 0 & :\mathbf{s}_u:^E\end{bmatrix}\begin{bmatrix}\mathbf{v}_p\\ \mathbf{T}_p\end{bmatrix}\\
&-j\omega_u\Re-jt\frac{\partial\Delta\omega}{\partial t}\begin{bmatrix}\mathbf{v}_u^* & \mathbf{T}_u^*\end{bmatrix}\begin{bmatrix}\rho_u & 0\\ 0 & :\mathbf{s}_u:^E\end{bmatrix}\begin{bmatrix}\mathbf{v}_p\\ \mathbf{T}_p\end{bmatrix}\\
&-jt\frac{\partial\Delta\omega}{\partial t}\Re-\begin{bmatrix}\mathbf{v}_u^* & \mathbf{T}_u^*\end{bmatrix}\begin{bmatrix}\dfrac{\partial\Delta\rho}{\partial t} & 0\\ 0 & \dfrac{\partial:\Delta:\mathbf{s}:^E}{\partial t}\end{bmatrix}\begin{bmatrix}\mathbf{v}_p\\ \mathbf{T}_p\end{bmatrix}
\end{aligned}
\tag{2.27}
$$

Equation (2.27) is the fundamental partial differential equation that can be generally applied to various acoustic waveguide or resonator configurations including SAW and QCM devices. Assuming that the spatial distribution of the acoustic field is unchanged but that the resonant frequency is perturbed, the terms **T** and **v** are in the form of a function of spatial variables multiplied by an exponential function of $j\omega_u t$ or $j\omega_p t$ such as

$$\begin{aligned} \mathbf{v}_u &= \mathbf{v}(x,y,z)e^{j\omega_u t}, \mathbf{T}_u = \mathbf{T}(x,y,z)e^{j\omega_u t} \\ \mathbf{v}_p &= \mathbf{v}(x,y,z)e^{j\omega_p t}, \mathbf{T}_p = \mathbf{T}(x,y,z)e^{j\omega_p t} \end{aligned} \tag{2.28}$$

Consider a QCM of AT-cut quartz with the y-axis through the thickness and the x-axis being the direction of displacement as shown in figure 2-12. Equation (2.28) can be evaluated with all the tensor terms reduced to scalars,

$$\begin{aligned} \mathbf{v}_u &= v_x(y)e^{j\omega_u t}\hat{\mathbf{x}} \quad , \quad \mathbf{T}_u = c_{44}S_{xy} = \frac{c_{44}}{j\omega_u}\frac{\partial v_x}{\partial y}e^{j\omega_u t} \\ \mathbf{v}_p &= v_x(y)e^{j\omega_p t}\hat{\mathbf{x}} \quad , \quad \mathbf{T}_p = c_{44}S_{xy} = \frac{c_{44}}{j\omega_p}\frac{\partial v_x}{\partial y}e^{j\omega_p t} \end{aligned} \tag{2.29}$$

where c_{44} is the shear stiffness coefficient.

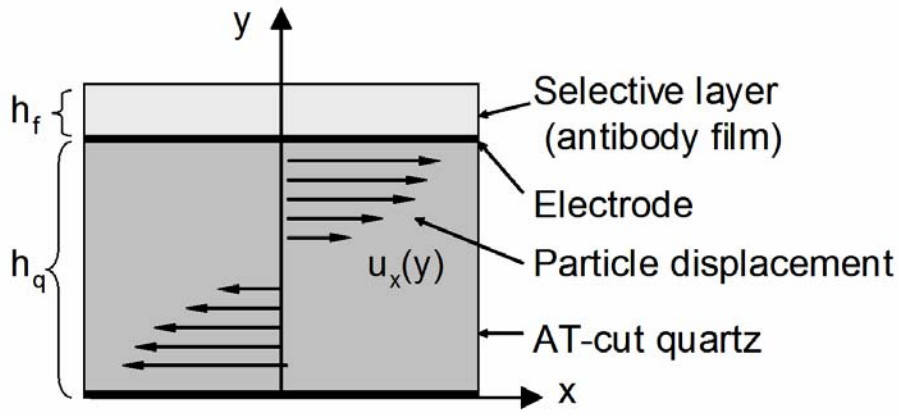

Figure 2-12. Side cross-sectional diagram of a QCM with biofilm coated (Not drawn to scale)

The next step is to integrate the partial differential equation (2.27) over the volume. Applying the divergence theorem to the left hand of (2.27) yields

$$\int_{vol}\left(\nabla\cdot\left[-\mathbf{v}_u^*\cdot\mathbf{T}_p-\mathbf{v}_p\cdot\mathbf{T}_u^*\right]\right)dV=\int_s\left[-\mathbf{v}_u^*\cdot\mathbf{T}_p-\mathbf{v}_p\cdot\mathbf{T}_u^*\right]\cdot dS \qquad (2.30)$$

The mechanical definition of fluids assumes that a shear wave is not supported. Therefore, the stress-free boundary condition $\mathbf{T}\cdot\hat{\mathbf{n}}=0$ is applied to the thickness shear mode of QCM in contact with fluid media like air or liquid. This makes the right side of (2.30) zero. Integrating the first term in (2.27) we get

$$\int_{vol}-j\Delta\omega\left\{\begin{bmatrix}\mathbf{v}_u^* & \mathbf{T}_u^*\end{bmatrix}\begin{bmatrix}\rho_u & 0\\ 0 & :\mathbf{s}_u:^E\end{bmatrix}\begin{bmatrix}\mathbf{v}_p\\ \mathbf{T}_p\end{bmatrix}\right\}dV=-4j\Delta\omega U \qquad (2.31)$$

where U is the total acoustic energy stored in the unperturbed field. Next, integrating $\Re$ over the volume gives

$$\int_{vol}\Re dV=\int_{vol}\left\{\begin{bmatrix}\mathbf{v}_u^* & \mathbf{T}_u^*\end{bmatrix}\begin{bmatrix}\Delta\rho & 0\\ 0 & :\Delta\mathbf{s}:^E\end{bmatrix}\begin{bmatrix}\mathbf{v}_p\\ \mathbf{T}_p\end{bmatrix}\right\}dV=\int_{vol}\left(\Delta\rho\mathbf{v}_u^*\cdot\mathbf{v}_p+\mathbf{T}_u^*:\Delta\mathbf{s}:^E\ \mathbf{T}_p\right)dV \qquad (2.32)$$

Considering the duality of stress-strain and stiffness-compliance, $\mathbf{T}_u^*:\Delta\mathbf{s}:^E\ \mathbf{T}_p$ in the right side of (2.32) can be replaced with $-\mathbf{S}_u^*:\Delta\mathbf{c}:^E\ \mathbf{S}_p$. Equation (2.29) indicates that in the case of QCM the only stiffness parameter applicable to this problem is c_{44} which is

a simple scalar quantity and equivalent to the Lamé constant μ. Now $\Delta\mathbf{c}^E$ can be simplified to $\Delta\mu$. For the QCM biosensor shown in figure 2-12, the immunoreaction affects the biofilm region only. Therefore, the perturbation on stiffness ($\Delta\mu$) is assumed to be nonzero only in (h_q, $h_q + h_f$) in figure 2-12. Further, since $h_f << h_q$, changes of the acoustic field quantity in the biofilm region can be ignored. Integrating (2.32) gives

$$\iint dxdz \int_{h_q}^{h_q+h_f} \Delta\rho v_{x0}^2 dy = A\Delta\rho h_f v_{x0}^2 \qquad (2.33)$$

where A is the area of QCM electrode, and v_{xo} is unperturbed shear particle velocity at the surface. The strain in $-\mathbf{S}_u^* : \Delta\mathbf{c} :^E \mathbf{S}_p$ at the surface is

$$S_{xyo} = \frac{1}{j\omega}\frac{\partial v_x}{\partial y}\Big|_{surface} = \frac{k_n}{j\omega} v_{xyo} \qquad (2.34)$$

where k_n is a wavenumber associated of the x-polarized shear wave. The volume integral of $-\mathbf{S}_u^* : \Delta\mathbf{c} :^E \mathbf{S}_p$ in (2.32) becomes

$$\iint dxdz \int_{h_q}^{h_q+h_f} \Delta\mu S_{xyo}^* S_{xyo} dy = A\Delta\mu h_f \frac{k_n^2}{\omega^2} v_{x0}^2 = \frac{A\Delta\mu h_f}{V_s^2} \qquad (2.35)$$

Combining (2.33) and (2.35), we get

$$\int_{vol} \Re dV = Ah_f v_{xo}^2 \left(\Delta\rho - \frac{\Delta\mu}{V_s^2} \right) \qquad (2.36)$$

Evaluating rest of the terms in (2.27) using the same approach, and combining all the subterms will give

$$t\frac{\partial \Delta\omega}{\partial t}\left(1 + \frac{Ah_f v_{xo}^2}{4jU}\left[\Delta\rho - \frac{\Delta\mu}{V_s^2} \right] \right) + \Delta\omega = \frac{Ah_f v_{xo}^2}{4jU}\left\{ -j\omega_u \left[\Delta\rho - \frac{\Delta\mu}{V_s^2} \right] + \left[\frac{\partial \Delta\rho}{\partial t} - \frac{1}{V_s^2} \cdot \frac{\partial \Delta\mu}{\partial t} \right] \right\} \qquad (2.37)$$

Because the film thickness $h_f << 1$ and the stored energy is expressed as $U = \frac{1}{4}\rho_q h_q v_{xo}^2 A$, equation (2.37) is simplified to an equation for $\Delta\omega$

$$t\frac{\partial \Delta\omega}{\partial t} + \Delta\omega = \frac{\omega_u h_f}{\pi\sqrt{\rho_q \mu_q}}\left\{ -\omega_u \left[\Delta\rho - \frac{\Delta\mu}{V_s^2} \right] + j\left[\frac{\partial \Delta\rho}{\partial t} - \frac{1}{V_s^2} \cdot \frac{\partial \Delta\mu}{\partial t} \right] \right\} \qquad (2.38)$$

where μ_q and ρ_q are the shear stiffness and density of the quartz crystal, respectively. Assuming that neither $\Delta\omega$, $\Delta\rho$ or $\Delta\mu$ changes with time, we get

$\Delta\omega = -\frac{\omega_u^2 h_f}{\pi\sqrt{\rho_q \mu_q}}\left[\Delta\rho - \frac{\Delta\mu}{V_s^2} \right]$, which is equivalent to

$$\Delta f = -\frac{2 f_u^2 h_f}{\sqrt{\rho_q \mu_q}}\left[\Delta\rho - \frac{\Delta\mu}{V_s^2} \right] \qquad (2.39)$$

Noting that μ_q and ρ_q are material constants, and the mass change $\Delta m = \Delta\rho A h_f$, (2.39) is essentially the Sauerbrey equation (2.11) with an additional term describing changes in the mechanical stiffness of the film. This equation predicts that a mass loading ($\Delta\rho$) will lower the frequency but an increase in stiffness ($\Delta\mu$) will induce a positive frequency shift. This relationship can be also applied to the SAW based sensors using the QCM-SAW analogy described in section 2.2.3 except for a few special cases that will be discussed in chapter 6.

If $\Delta\rho$ and $\Delta\mu$ were known as a function of time, the solution of (2.38) would be

$$\Delta\omega(t) = \frac{1}{t}\left(\int_t \frac{\omega_u h_f}{\pi\sqrt{\rho_q \mu_q}} \left\{ -\omega_u \left[\Delta\rho(\tau) - \frac{\Delta\mu(\tau)}{V_s^2} \right] \right\} d\tau + j\left[\Delta\rho(t) - \frac{\Delta\mu(t)}{V_s^2} \right] + C \right) \qquad (2.40)$$

The significance of equation (2.40) lies in the fact that it provides a potential tool for resolving the acoustic wave biosensor signature into dynamic information relating to molecular structure changes during a molecular recognition event.

2.5 Conclusion

In this chapter, various acoustic wave modes typically used for sensor applications were discussed. The application and operating environment of the sensors *e.g.* in liquid phase or gas phase are determined depending on the nature of the acoustic modes on the substrate materials. QCMs are the best choice for liquid phase detection due to their lack of vertical particle polarizations, but hardly used for vapor phase sensors due to its low sensitivity compared to their SAW counterparts. SAW devices are by far

the most sensitive to the surface loading among the acoustic sensor category, but caution is required for immunosensor applications due to the serious damping to the liquid loading except the ones with shear horizontal modes such as SSBW and STW. A material choice for the substrate was also considered. Despite the nature of weak piezoelectricity, the temperature stable ST-cut quartz is currently the dominant piezoelectric substrate for sensor applications. Also, a broad derivation using complex reciprocity relation and perturbation theory was presented which ended up with adding a new mechanical parameter to the classic equation. The new equation can now account for the positive frequency shift which is occasionally observed in a modern acoustic wave biosensor. In particular, the derived relation can be a potential tool for monitoring the dynamic information relating to molecular structure changes on the sensor surface during a molecular recognition event.

CHAPTER 3

CREATION OF THE SELECTIVE BIOLAYER

3.1 Introduction

A stable antibody immobilization on the sensor surface is required to realize the high selectivity of an immunosensor. Antibodies are a mixture of proteins with a very complex 3D structure and recognize a specific antigen unique to their target. Figure 3-1 illustrates a simplified diagram of an antibody monomer.

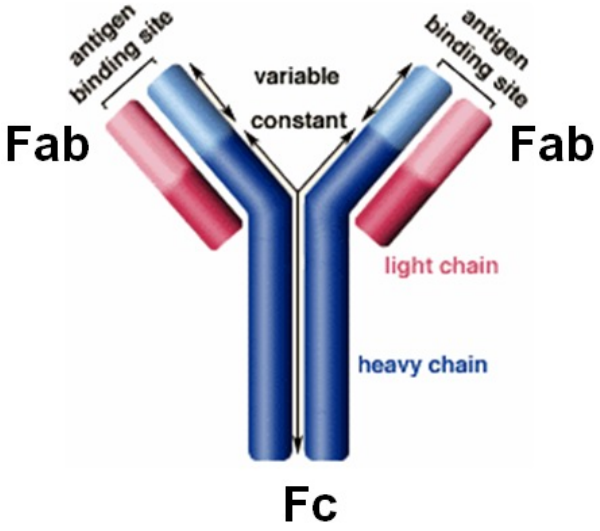

Figure 3-1. Schematic diagram of an antibody molecule and its fragments

Each antibody monomer has a molecular weight of approximately 150,000 Daltons and is composed of two identical heavy polypeptide chains and two identical light chains, covalently bonded via disulfide (S-S) linkages between cysteine residues. Each heavy chain is about 440 amino acids long; each light chain is about 220 amino acids long. An antibody molecule consists of 3 fragments; two identical F_{ab} fragments which are antigen binding sites and one F_c fragment which is a stem of the antibody and

has a carboxyl group on the end. The F_c region determines the biological properties of the antibody. Monoclonal antibodies are produced by the descendants of a single B cell and are identical with each other, as opposed to the polyclonal antibodies from multiple cell lines. They recognize only one specific epitope and have a defined specificity for the antigen. For this reason, monoclonal antibodies are of more interest for immunosensing applications because they give reproducible results.

In principle, antibodies, or more generally, proteins can be fixed noncovalently onto an inert metal surface by simple adsorption. However, antibodies immobilized by physical adsorption are not stable during the immunosensing process, especially if buffer rinses are carried out, because the physical adsorption is based on attraction forces, such as electrostatic force, rather than chemical bonds. Therefore, a covalent immobilization is desired to achieve better biomolecule activity, reduced nonspecific adsorption, and greater stability. Another major issue regarding the antibody immobilization is the orientation, which is considered to be a determinant of their effectiveness. Immobilized antibodies must be in an oriented and homogeneous manner, rather than randomly distributed on the surface. An immunoglobulin G (IgG) antibody is considered to be properly oriented and completely active when immobilized on the F_c fragment of the antibody rather than the F_{ab} fragments which contain antigen-binding sites. To achieve stable and efficient binding, it is necessary to couple the antibodies to the sensor surface via a heterobifunctional crosslinker. Here, several antibody immobilizing methods, on which the author has been working to create a selective layer for an immunosensor, are described.

3.2 Methods of Antibody Immobilization

3.2.1 Alkane-thiol Self Assembled Monolayer (SAM)

The first antibody immobilizing method involves the implementation of an alkane-thiol self-assembled monolayer (SAM) as the cross-linker between the antibodies and the metal electrode of the device. The sulfur in thiol (S-H) group has high affinity to a gold surface and the other terminal of the hydrocarbon chain binds to the stem (*i.e.* F_c region) of the antibody through a coupling agent. As a result, alkane-thiol chains orient themselves into an aligned monolayer ~30° off normal to the surface of the device as shown in figure 3-2. The 30° tilt is due to the spontaneous movement of carbon chains to maximize the Van der Waals interactions. Following chemical treatment of the carboxylic acid, the immobilized SAM layer reacts with the antibody to form a covalent bond which fixes the antibody to the acoustic wave device.

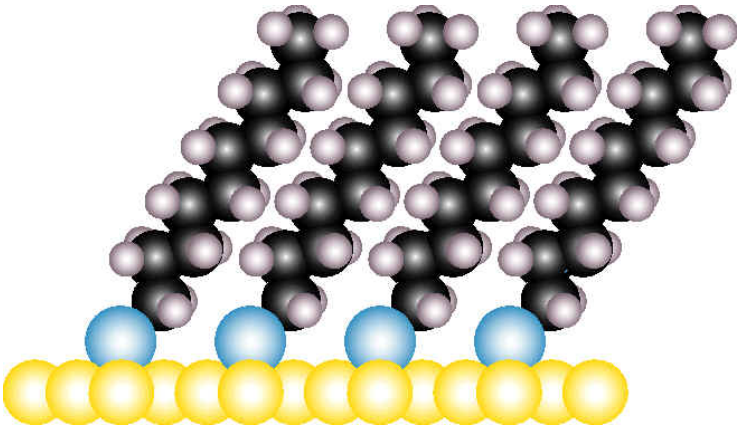

Figure 3-2. Schematic of self-assembled monolayer on a gold surface. The tail group has decane ($C_{10}H_{22}$) in this example. Illustration from http://stm1.chem.psu.edu/

It has been reported that the use of a longer (with 10 or more carbons) carbon chain is expected to provide a better-ordered and more stable SAM architecture [23]. However, from the sensitivity standpoint, too long a carbon chain may result in a reduced sensitivity because the immunoreaction or molecular recognition event can occur outside the evanescent tail of QCM energy distribution profile. The increased sensitivity from a shorter carbon chain was verified by Witt *et al* [24]. Also, the thickness of the biofilm h_f in figure 2-12 in chapter 2 is no longer ignored for the long carbon chain. In this case, the changes of the acoustic field quantities in the biofilm region should be calculated separately because the surface and antibody layer cannot be considered to move in the same phase, which would make all the derivations worked in section 2.4 invalid. Using the 3,3'-dithiodipropionic acid shown in figure 3-3, the author's research group could realize fairly stable immobilization on a QCM gold surface without sacrificing the sensitivity. [22, 25]

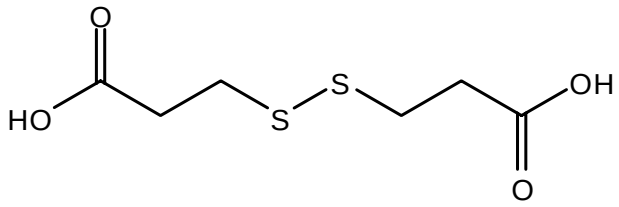

Figure 3-3. Chemical structure of a 3,3'-Dithiodipropionic acid molecule

The immobilization method specific for the QCM sensor using the 3,3'-dithiodipropionic acid are summarized here. First, QCMs were cleaned using Piranha solution (30% H_2O_2 and concentrated H_2SO_4 in 3:7 volume to volume mixture). The crystals were air-dried. 1 mg of 3,3'-dithiodipropionic acid was dissolved in 100% ethyl alcohol to make a 1 mM alcoholic solution. The monolayer was applied to the QCM gold

electrodes and allowed 2 hours to self-assemble. The crystals were then washed with 95% ethanol followed by aliquots of deionized water before allowing them to air-dry. A mixture of 1-Ethyl-3-(3-Dimethylamino-propyl) Carbodiimide (EDC) (0.0133 mg) dissolved in 0.1 ml of 1x TAE (Tris-Acetate-EDTA) buffer and 13.5mg of NHS (N-hydrocylsulfo-succinimide) dissolved in 0.1 ml of buffer was used to activate the carboxyl groups on the dithiopropionic acid for the subsequent coupling reaction with the antibody. The crystals were washed with deionized water and allowed to dry. Antibodies (3-5 µl) were diluted in 1X TAE buffer, and then allowed to incubate on the crystals' surfaces overnight before the final washing steps to remove unbound material. Ethanol-amine (0.05 M) was added to the surface to block all unbound sites before mounting in a sensor system. A simplified surface structure of antibody immobilized QCM after subjected to the target is illustrated in figure 3-4.

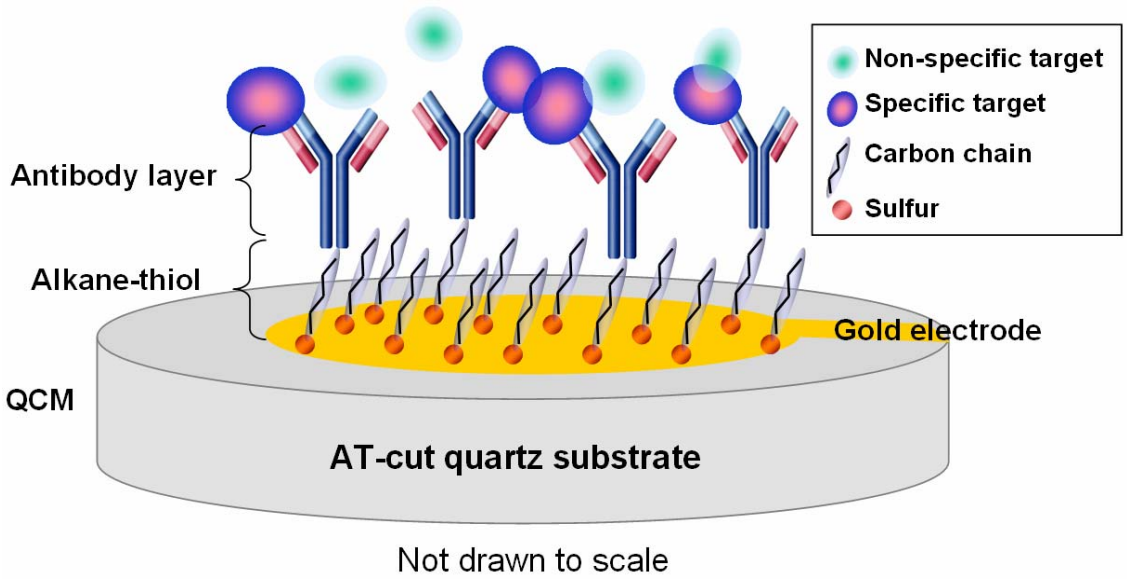

Figure 3-4. Schematic of the antibody immobilization on the QCM using a self assembled monolayer (SAM) as a cross-linker.

3.2.2 SPA (Protein A) + Hydrogel

SPA, a.k.a. Protein A, is an immunoglobulin binding protein derived from the cell wall of a bacterium *Staphylococcus aureus*. It is an effective Fc receptor that binds to the Fc portion of IgG subclass antibody leaving its active antigen binding sites free. SPA exists as a single polypeptide chain of molecular weight 42 kDa and has a very extended shape [26]. The binding between SPA and metal surface such as gold is fairly stable with high adhesion coefficient. This affinity is believed to be the result of both electrostatic and Van der Waals interactions [27]. It is reported that linking an antibody with SPA improves the antibody's binding capacity [28].

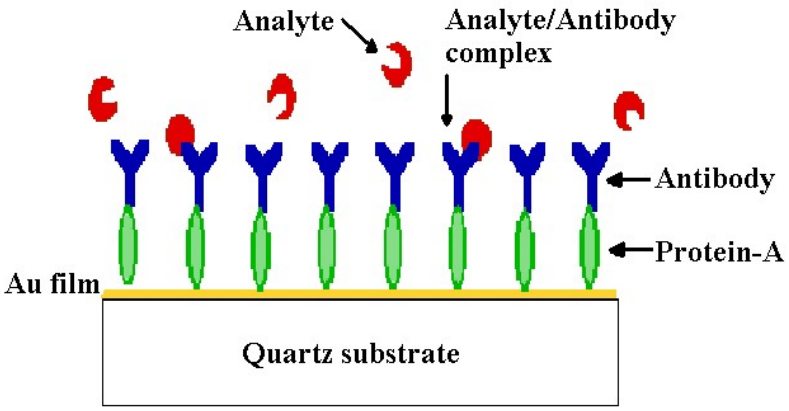

Figure 3-5. Schematic of antibody immobilization using SPA

The immobilization protocol introduced herein is based on the conventional method by Davis and Leary [27]. The antibody immobilization technique first requires polarizing the metal surface on the SAW device. This is accomplished by immersing the device in 5 ml of 1.2 M HCl for 5 minutes, and then washing with DI water, followed by

5 ml of 1.2 M NaOH for 5 minutes. The device is washed again with DI water before immersed in 3 ml of 1.2 M HCl for 2 minutes. The chip is washed twice with DI water, followed by TAE buffer solution and is allowed to air dry. SPA (0.2 mg) is dissolved in 100 μl of buffer solution at physiological pH. Then, 10 μl of antibody (0.023 mg/ml) is mixed with the buffered SPA solution and the mixture is placed in a 4°C refrigerator for 2 hours. Three microliters of the cross-linker-antibody solution is used to coat the device. The chip is allowed to air dry and the remaining solution was spun off for 30 seconds at 5000 rpm. For the sensors to be used in the vapor phase, the final preparation involves the deposition of a thin hydrogel layer to support the antibody layer and provide a semi-aqueous environment on the sensor surface. It is known that in the absence of an aqueous environment, the binding sites on the antibodies will lose their prescribed structure required for molecular recognition [6]. In fact, the properly immobilized hydrogel behaves as water in most respects except that it is a rubbery solid with a mesh structure.

3.2.3 Offset Lithography Printing

The purpose of this immobilization method is to dispense known amounts of antibodies onto desired locations on the surface of microsensors such as SAW resonators. As will be discussed in chapter 6, there are instances that immunoreactions need to be "forced" to occur only on specific locations on the device surface. This enables us to obtain more consistent responses, specifically for the SAW array sensor systems incorporating multiple SAW resonators. Conducting this method requires equipment that can drop a small amount of antibodies on the surface of SAW resonators.

The BioChip Arrayer™ (BCA) is a bench top micro dispenser which can dispense minuscule droplets with precision up to 5 micron spacing. This technology utilizes piezoelectric actuators to squeeze capillary glass tubes to dispense pre-determined numbers of picoliter sized droplets on the solid surface. The principle is similar to the offset printing technology of an inkjet printer. The difference is that instead of ink, the BCA prints biological molecules such as proteins or antibodies. Printing of antibodies using the offset printing technique has been reported [29], but using this apparatus and technology for the acoustic wave immunosensor applications is rarely introduced.

Figure 3-6(a) shows the BCA dispensing unit working on a SAW resonator sensor. Figure 3-6(b) shows an actual SAW resonator sensor surface with the printed anti-FITC antibodies. In this example, the antibody deposition is localized only between the two IDTs of the SAW resonator. Likewise, controlled concentration and volume of antibodies can be printed on desired locations of the sensor surface *e.g.*, on the transducers, reflector gratings, the acoustic cavity region, or combination of those by programming the BCA. Immunosensing experiments using the SAW devices with a selective layer created by the BCA will be introduced in chapter 6. The monoclonal antibodies pre-mixed with a crosslinker such as Protein A are loaded in the dispenser tip, and then printed on the locations pre-determined by the program. The immobilization is done by the same principle introduced in section 3.2.1.

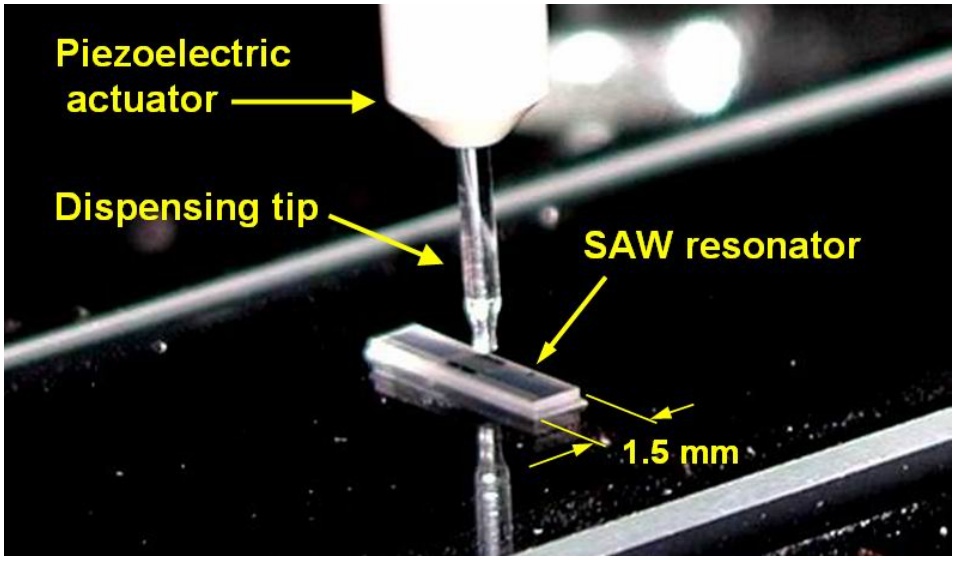

(a)

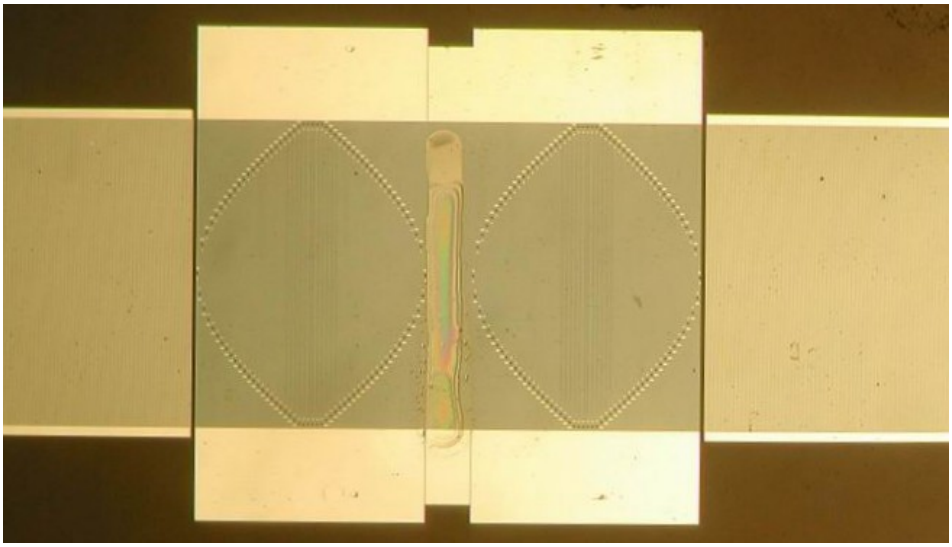

(b)

Figure 3-6. (a) BioChip Arrayer working on a SAW resonator (b) Immobilized anti-FITC antibody layer between the two IDTs. The gap between the IDTs is about 0.12 mm.

3.2.4 Electrophoretic Immobilization through Plasma Polymerized Hydrogel Film

This section introduces an electrophoretic procedure for the deposition of antibodies or other charged molecules on the SAW device surface coated with plasma polymerized hydrogel. As mentioned in chapter 1, the hydrogel layer plays an important role in the vapor-phase immunosensing as it provides a semi-aqueous environment for the immobilized antibodies. Hydrogels are water swollen polymeric networks derived from one or more hydrophilic monomers and involve interactions such as hydrogen bonding and strong Van der Waals interactions between polymeric chains [30]. Hydrogel thin films containing biomolecules such as antibodies are attractive biosensing platforms due to their outstanding properties: they are extremely thin (<200 nm), have a uniform conformation, offer good adhesion to the substrates, have mechanical and chemical stability, and possess biocompatible characteristics.

The monomer of the hydrogel used herein is N-isopropylacrylamide (NIPAAm) shown in figure 3-7. NIPAAm has been studied most frequently as a water-soluble polymer and a cross-linked network. When grafted onto solid surfaces, the physical properties can be controlled by temperature. Below the lower critical solution temperature (LCST), the surfaces are hydrophilic, swollen, and non-protein adsorptive. As the temperature increases above the transition temperature the surface suddenly dehydrates and becomes hydrophobic. Through variation of reactor conditions such as deposition pressure and substrate temperature, it is possible to tailor and control chemical properties of the films such as crosslink density and thus swelling [31].

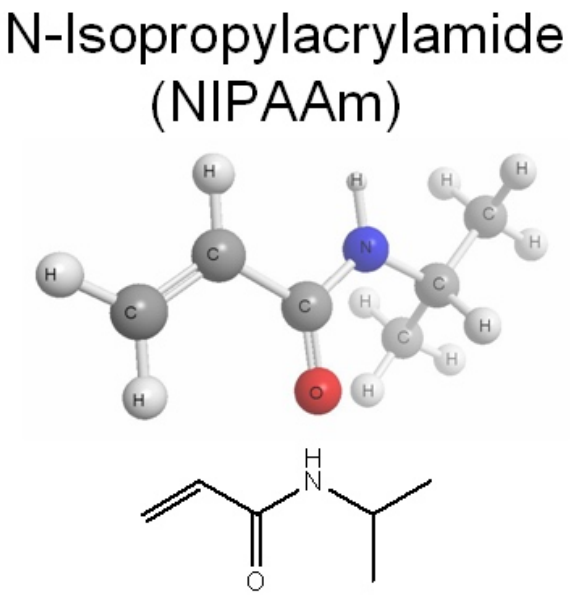

Figure 3-7. Molecular structure of a N-Isopropylacrylamide (NIPAAm) monomer

The plasma polymerized hydrogel layer has the following advantages over the conventional spin cast hydrogel:

Acoustically thin film: In addition to the increased complexity in the modeling and analysis of the sensing interface area, SAW devices will suffer from a severe attenuation if the thickness of the film becomes comparable to the acoustic wavelength. Conventional spin coating has limitations on realizing a thin film deposition due to some practical problems such as coagulation of gel during the spinning. Plasma polymerized hydrogel is about 200 nm in thickness which is less than one fiftieth of the acoustic wavelength (12.5 μm) of the SAW device used in this work. Such a thin coating is also desirable when making electrical connections to the package by wire bonding, etc.

Uniformity: The plasma polymerization process provides a uniform deposition. Specifically for the SAW device, the thickness of the coating should be uniform all over the surface; otherwise the frequency response cannot be predicted.

Consistent and controlled thickness: The plasma polymerization process is capable of making identical hydrogel layers on multiple devices. With a conventional spin casting method, the coating thickness easily becomes different from device to device even with the same spin rate. Creation of identical films with the same physical characteristics is very important when a reference sensor is employed in a sensor array. The reference sensor becomes meaningless if the film characteristics are all different among other sensors working in the same flowcell. The significance of the reference sensor will be discussed in chapter 4.

The detailed physics and methodology of the RF plasma polymerization process are not described here because they are not the scope of this thesis. Instead, the author will focus on the description of the electrophoretic immobilization procedure and some experimental results that prove the validity of this method. The electrophoretic immobilization process utilizes a similar principle to the protein electrophoresis technique. At a pH above the isoelectric point (pI), proteins carry a net positive charge and vice versa. This is valid for antibodies and potentially other charged biomolecules, and they can be incorporated from buffer solutions into hydrogel thin films by external electric field. The schematic of the experimental apparatus is shown in figure 3-8.

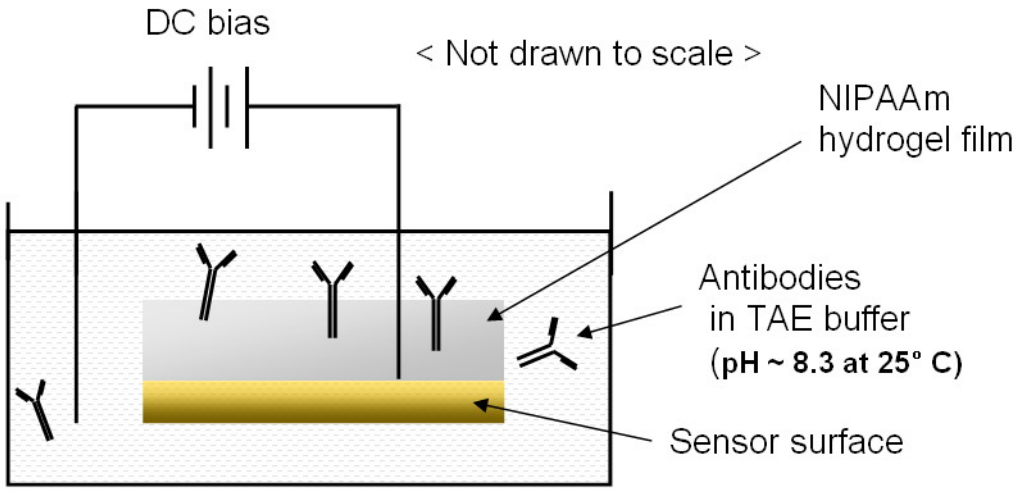

Figure 3-8. Schematic of the Electrophoretic immobilization setup

Electrophoretic incorporation of antibodies in the hydrogel films is simple to implement and can be used to control the orientation of antibodies in the hydrogel. The antibody takes on negative charge when diluted in TAE buffer with pH ~ 8.3 at 25° C, so it will migrate towards the positive electrode in an electrophoretic apparatus. In the present example, the negatively charged F_c fragment of the antibody is attracted to the positively biased device surface underlying the poly-NIPAAm film, which leaves the F_{ab} portion to bind the antigen.

There are fundamental differences between this electrophoretic immobilization method and previously introduced methods in sections 3.2.1 and 3.2.2. First, a crosslinker is not involved in this method; antibodies are immobilized directly on the hydrogel layer, not on a bare device surface. Second, the immobilization is 'compulsive' in the sense that the antibodies are pulled into the hydrogel layer by an external force, the electric field in this case. This is in contrast to the SPA or SAM immobilizations where the antibodies are spontaneously immobilized by inherent chemical affinity.

For the actual experiment of electrophoretic immobilization, anti-FITC (fluorescein isothiocyanate) antibodies and uranine, the antigen, are used for a visual verification through fluorescent immunoassay. The fluorescent immunoassay will be described in more detail in section 3.3. SAW resonator devices are coated with poly-NIPAAm by the parallel plate RF plasma reactor operating at a frequency of 13.56 MHz. To immobilize anti-FITC, the hydrogel coated quartz substrates were immersed in the 1X TAE buffer solution containing anti-FITC antibodies. Subsequently, the metal film underlying the poly-NIPAAm film was positively biased (1 V DC) with respect to the buffer (electrolyte) for 5 min. The amount of the applied voltage and processing time are determined by numerous experiments, and specific to the author's experimental setup and device parameters.

The actual photographs of the immobilizing process are shown in figure 3-9. Two different methods have been tried to apply a DC voltage to the devices. In figure 3-9(a), the electrical contact was achieved directly through two micro-DC probes. In figure 3-9(b), the SAW device was mounted and wire bonded on a TO-8 package, and the voltage is applied through the package pins. One practical difficulty with the method in figure 3-9(a) is the electrical connection for the immobilization or measurement as the coated hydrogel layer prevents the probe tips or DC probes from making electric contacts with the electrode. It is necessary to peel off some hydrogel layer to expose the electrodes for the measurement. In this sense, the method in figure 3-9(b) provides a more stable connection for measurements, and the DC voltage is more easily applied. On both cases, the process was continuously monitored through the microscope to see possible connection failure or device damage.

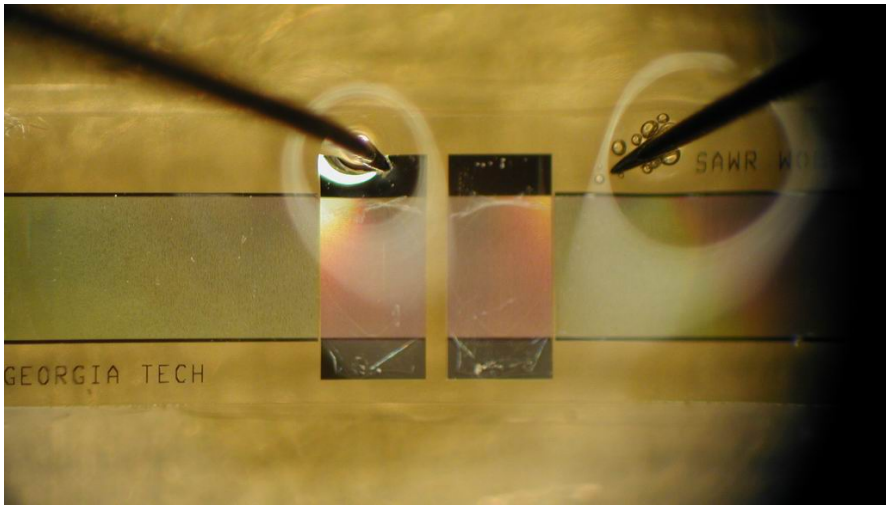

(a)

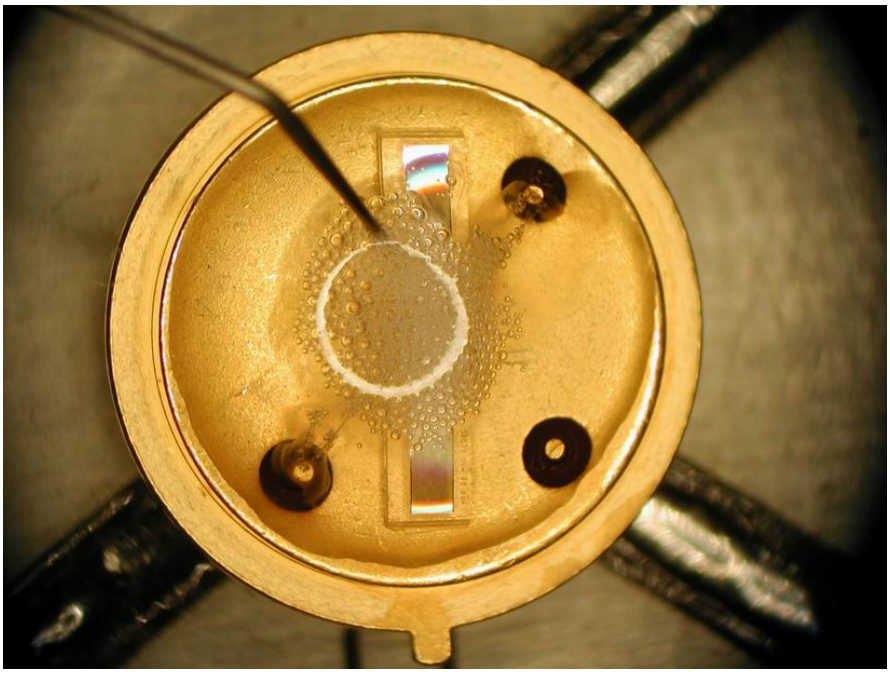

(b)

Figure 3-9. Antibody immobilization process on a 250-MHz SAW resonator coated with 200 nm NIPAAm PPF. (a) Direct immobilization on a SAW resonator chip using two DC probes (b) Immobilization on a TO-8 packaged SAW resonator after wire bonding.

About 1 nM aqueous solution of the fluorescein salt (uranine) was present to the device surface by bubbling nitrogen at through the solution at 0.3 SLPM for 20 seconds, followed by 10 seconds of air-purging at 1.85 SLPM. The air-purging helps remove any unbound (simply adsorbed) analytes from the surface. The chips were then viewed using a Zeiss LSM510 confocal fluorescent microscope (CLSM). The results are shown in figure 3-10. In these CLSM images, a significant amount of the bright spots in figure 3-10(a) indicate the presence of the captured uranine molecules which are attributed to the antibody-fluorescent antigen complex and hence a confirmation of the incorporation of antibodies. Two control samples, the first coated with poly-NIPAAm film without antibodies and the second a bare SAW device were also studied and compared with the result shown in figure 3-10(a). A few fluorescent spots in figure 3-10(b) are presumably the antigens simply adsorbed to the surface due to the sticky nature of the hydrogel. The bare device did not show any fluorescent attached on the surface as expected.

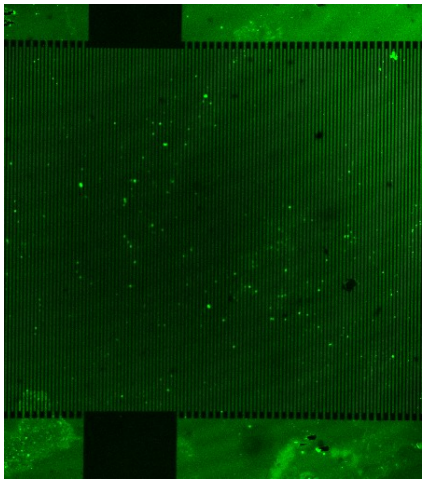

(a)

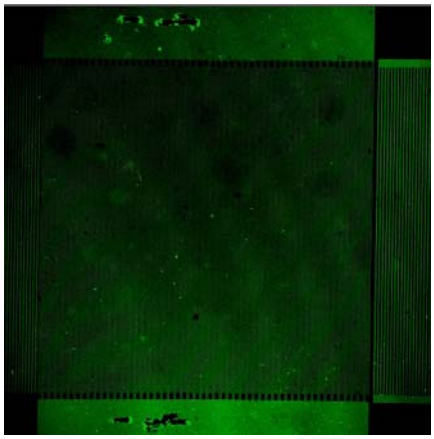

(b)

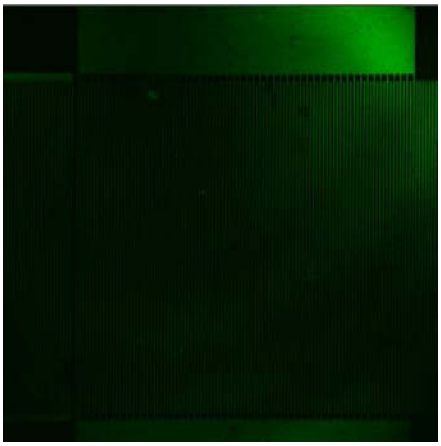

(c)

Figure 3-10. CLSM image of SAW resonator surface after exposure to fluorescent antigen. (a) NIPAAm coated surface with anti-FITC immobilized (b) NIPAAm film without immobilized antibodies (c) Bare SAW device

3.3 Fluorescent Immunoassay

The antibody immobilization process for immunosensors should include an independent assessment of the predicted molecular recognition event. A novel fluorescent immunoassay protocol was developed to provide a method for a visual confirmation of the occurrence of molecular recognition as well as to verify the stable antibody immobilization [32]. SAW devices with and without anti-FITC (fluorescein isothiocyanate) antibody films were tested against two different fluorescent analytes: uranine (a.k.a., fluorescein sodium salt) and Alexa Fluor®, or Alexa. Uranine is selected as a FITC analyte because a FITC is not dissolved in water but in an organic solvent which, during testing, might denature the immobilized antibodies. The structural formulas for these molecules are presented in figure 3-11.

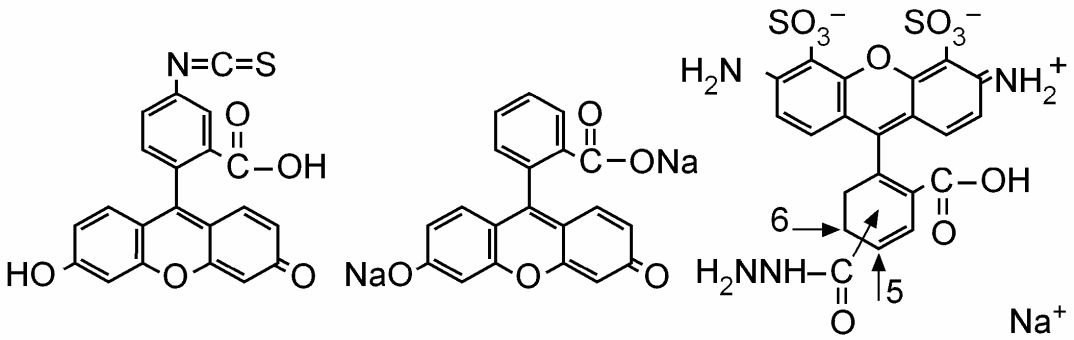

Figure 3-11. Structural formulas for (a) FITC; (b) uranine; and (c) Alexa Fluor.

The uranine is water soluble and binds to the anti-FITC antibodies [32]. It should be noted that, at the physiological pH which was used for the uranine solution, the Na^+ ions would be dissociated from the uranine molecule. In the similar pH range, the FITC

molecule will lose the hydrogen atoms attached to the hydroxyl and carboxyl groups. Under these conditions, the two molecules will be identical except for the isothiocyanate group (N=C=S) on the FITC molecule. Also, a good binding affinity of the uranine molecule to the anti-FITC antibody, which will be shown later, indicates that the epitope on the FITC antigen does not include the isothiocyanate group.

As in any immunoassay technique, it is important to test the device against a control analyte. To accomplish this, an aqueous solution of Alexa was used. Alexa is also a fluorescent dye and has a similar chemical structure to FITC in that it has four linked phenyl groups. However, the introduction of negatively charged sulfite groups attached to the outer portion of the molecule significantly changes the binding characteristics and prevents recognition by the anti-FITC antibody.

The protocol consisted of presenting the analyte to the SAW resonator devices by bubbling nitrogen through a 1 nM aqueous solution of the analyte compound. After brief exposure to the analyte vapor, packaged devices were pulled from the system, washed with buffer to remove unbound analyte, and then viewed using the Zeiss LSM510 confocal laser scanning microscope (CLSM). As the laser (λ = 488 nm) excites fluorescence both from uranine and Alexa, any fluorescence observed in the CLSM images is taken as evidence of captured fluorescent analytes. Figures 3-12(a) shows the CLSM images at 20X magnification of an anti-FITC coated SAW chip after exposure to the uranine vapor. In this image the bright fluorescent spots are the areas where uranine molecules have been captured, indicating that over the brief exposure to the uranine vapor, binding did indeed occur. Figure 3-12(b) shows the CLSM image for the anti-FITC devices after exposure to Alexa and subsequent washing to remove unbound

analytes. There is no trace of fluorescence, indicating that Alexa did not bind to anti-FITC. This result can be alternatively verified by monitoring the actual time-dependent signatures of the corresponding sensors. In this case, the binding events will translate into a distinct frequency shift in the SAW resonator response, which will be demonstrated in chapter 5. In summary, a series of experimental results from the fluorescent immunoassay proved the validity of the aforementioned antibody immobilization protocols as well as the antibody's binding affinity to the specific target.

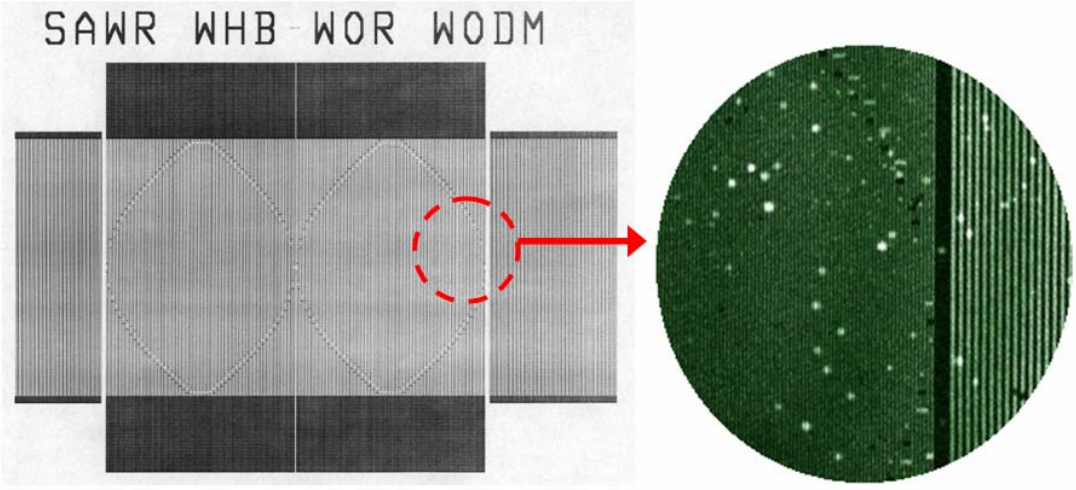

(a)

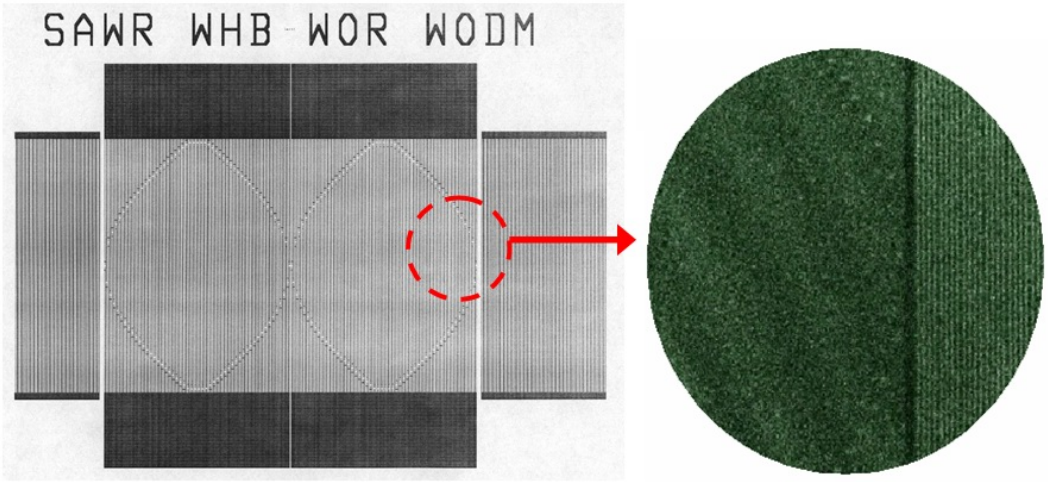

(b)

Figure 3-12. Layout of the actual SAW devices and the CLSM images of an anti-FITC coated SAW resonator after exposure to (a) uranine vapor and (b) Alexa vapor.

3.4 Conclusion

Establishing a repeatable method of immobilizing antibodies is of major importance as it allows achievement of *in vitro* molecular recognition. In addition, the use of antibodies incorporated in biosensors allows for real-time monitoring giving some insight on binding kinetics of various molecules. Although there are many immobilization methods for piezoelectric biosensors, there is still no absolutely ideal method that gives the highest immobilization yield and the best stability. Furthermore, the complexity and diversity of biological compounds that can be used for different purposes make it even harder to come up with an optimal method. Therefore, it is necessary to find a suitable immobilization method for each particular application. The selection of an effective method requires study of different immobilization methods in detail.

CHAPTER 4

LIQUID PHASE DETECTION USING A QCM IMMUNOSENSOR

4.1 Quartz Crystal Microbalance (QCM) as a Sensor

Quartz plate resonators utilizing a TSM (thickness shear mode) have been used as sensitive microbalances since the late 1950's. Their usage during the early stage was to monitor the thickness of metals being deposited on wafers in evaporation systems [7], but there is a rapid increase in new applications such as biochemical sensing, medical diagnostics, and environmental monitoring. The improved sensitivity and detection limit from the advanced instrumentation techniques of modern QCM sensors result in the new term 'quartz crystal nano-balance'. As described in chapter 2, the underlying physics of the QCM sensing is based on perturbation of the sensor surface when the detection occurs that leads to the change in the resonant frequency. The perturbation arises from a mass attached on the sensor surface or changes of physical properties of the contacting medium, or both.

In this chapter, detailed experimental procedures and the results of a bacterial spore detection using a dual channel 10-MHz QCM sensor system are demonstrated. From these experiments, the author obtained a measured mass sensitivity of ~4.1 ng/Hz-cm^2, which was in good agreement with a reported sensitivity of the QCM of the same specification [19].

4.2 Bacterial Spore Detection Using a Dual Channel QCM Immunosensor

With support of the Centers for Disease Control and Prevention (CDC) in Atlanta, GA, the author conducted a series of experiments for rapid identification of *Bacillus subtilis* (non-pathogenic simulant for *Bacillus anthracis*) spores by constructing a dual quartz crystal microbalance (QCM) immunosensing system [33]. A set of 10-MHz AT-cut QCMs operating in thickness shear mode are employed in a high precision flow-through enclosure, or flowcell. Specificity is maintained through the use of a detection layer consisting of monoclonal antibodies raised against spores of a single *Bacillus* species. The fidelity of sensing parameters is ensured by the presence of a control sensor coated with an antibody that is not specific for the target antigen. Associating the QCM response signature with the specific binding of a particular species of *Bacillus* spore to an antibody has implications for future identification of pathogenic substances.

4.2.1 Background

The genus *Bacillus* is of particular importance because it can adapt by changing to a dormant life form known as an endospore, which is capable of surviving severe environmental conditions, and stringent decontamination procedures that would destroy a vegetative cell. These spores may contaminate food, water or may be transmitted as aerosols via air-conditioning, in either case they can be the source of animal and human infections. More recently, pathogenic endospores such as *Bacillus anthracis*, the causative agent of anthrax, have become feared as a potential threat for biological warfare and bio-terrorism. The availability of monoclonal antibodies specific to a single spore type (recognizing particular epitopes on the endospore protein coat) along with the design

of a QCM system forms the building blocks for a highly sensitive, highly specific biosensor. It is known that the monoclonal anti-spore antibodies do not cross-react with the vegetative cells from which they are derived [34], and are species-specific; spores of other species are not recognized [35]. Early detection of spores in, for example, public water systems, is important since it permits rapid responses that can isolate sources of contamination and thus prevent the dissemination of a pathogen. Current immuno-detection methods require periodic sampling and assay by an investigator, with results emerging in minutes or hours. Monitoring by this method is thus discontinuous and limited by the frequency of sampling. Given the swiftness with which sporophytic pathogens can be administered to water supplies, populations would be at risk in the intervening periods. Rapid detection implies that the existence of target is identified without time-consuming biochemical post-process such as ELISA (enzyme-linked immunosorbent assay) or microscopy analysis. Further, the presence of an appropriate nanobiosensor in a water system would provide continuous monitoring for pathogens.

In the experiment herein, monoclonal antibodies raised against the spores of *Bacillus subtilis* (referred to as *B. subtilis* hereafter) were employed. They were obtained from Dr. John Kearney of the University of Alabama at Birmingham. The *B. subtilis* is a Gram-positive, spore-forming bacterium commonly used as a non-pathogenic simulant for *B. anthracis*. Figure 4-1 shows optical microscope pictures of the *B. subtilis* cells and spores. The sizes of a spore and a vegetative cell are approximately 1 μm and 4 μm respectively. Because the biological behavior and physical characteristics of *B. subtilis* are very similar to those of the anthrax [36], the protocols used for the detection of *B. subtilis* can be applied for the detection of anthrax spores.

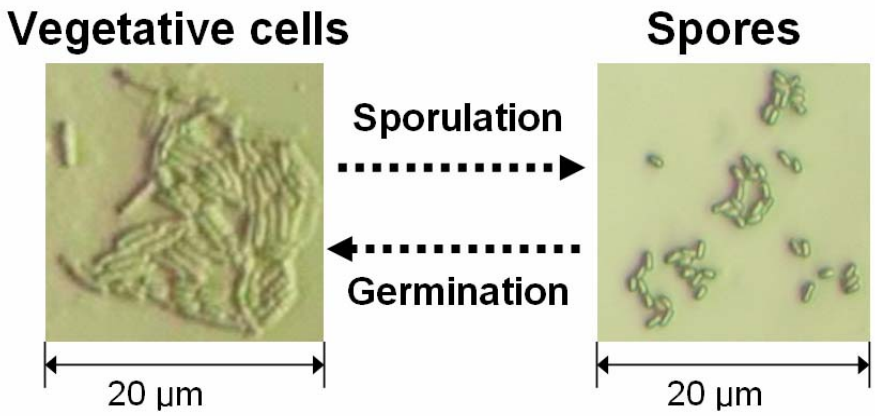

Figure 4-1. *Bacillus subtilis*: A benign "surrogate" for *Bacillus anthracis*. Optical microscope images taken by the author at Hunt Lab, Georgia Tech

4.2.2 Sensor System Setup

Commonly used liquid phase immunosensing systems employ a flowcell where a target solution is injected into at a certain flow rate. The QCM sensor system used herein consists of three main parts as shown in figure 4-2: Injection, Sensing, and Data Collection. The injection part has high precision syringe pumps from Harvard Apparatus, loaded with medium and target solution. The injection of the medium (buffer solution here) along with the target plays a significant role and will be described later. The sensing part includes two QCMs, two oscillators that drive the QCMs, and a dual QCM flow cell. The QCM crystal is sandwiched between two rubber o-rings to prevent leaks. The photograph in the upper-left corner of the figure 4-2 shows the actual image of the sensing part. The data collection part has a frequency counter and a laptop PC. The sensor data is transferred from the frequency counter to PC thru RS232C serial ports and collected in real-time by LabVIEW^{TM} program installed on the PC. The sampling period

and the resolution of the frequency counter are 0.5 second and 0.1Hz, respectively. All the experiments were done at room temperature.

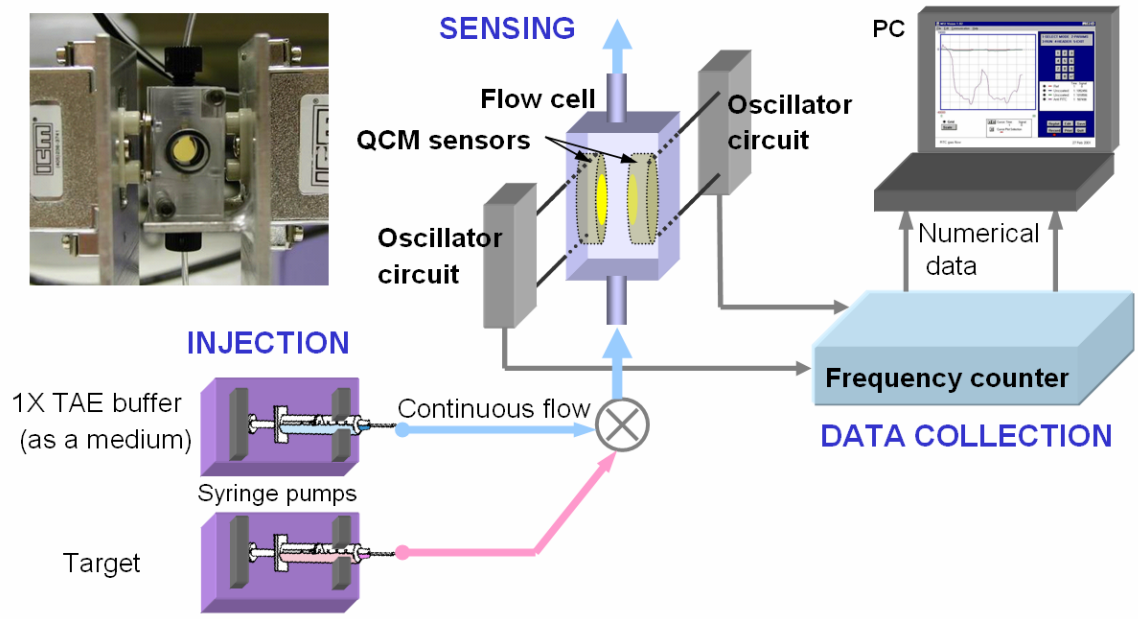

Figure 4-2. Schematic of the dual QCM sensor system setup. The upper-left picture shows the actual Sensing part; flowcell with the QCMs and oscillators mounted.

The specification of the QCM used in this experiment is shown in Figure 4-3. The oscillator units and the 10-MHz QCMs with AT-cut quartz were from International Crystal Manufacturing Co, Inc. The thickness of the quartz substrate is 0.17 mm which requires careful handling when mounting in the flowcell. The electrode (active sensing area) of the QCM is 0.22 cm^2 and coated with a gold film with a thickness of 100 nm. Reviewing equation (2.13) in chapter 2, the acoustic wavelength of this QCM in the fundamental mode is 0.34 mm. The electrode thickness is less than 0.03 % of the wavelength and thus can be safely ignored for the analysis.

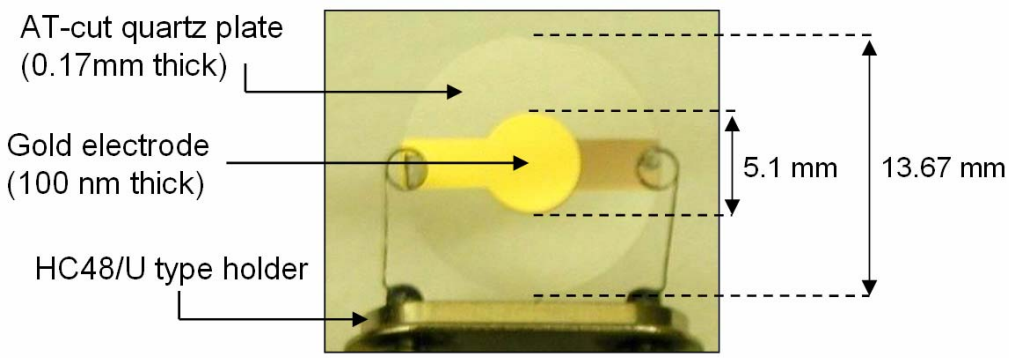

Figure 4-3. Picture of a 10-MHz AT-cut QCM mounted in a HC48/U package.

There are two notable configurations in this QCM sensor system setup. First, the liquid flowcell is designed so that it can hold two QCM sensors facing each other. These two QCM sensors undergo virtually the same physical changes, *e.g.* hydraulic pressure, temperature variation, and external vibrations. Also one sensor is coated with antibodies specific to the target and the other with antibodies that do not recognize the target. This enables us to monitor unnecessary signals that are not related to the target detection, as well as to exclude non-specific ligand-antibody interactions from genuine binding interactions and thus to perceive a true signature of the detection. Second, in addition to the target injection, the syringe pump also injects a continuous stream of 1X TAE buffer solution into the flowcell at a small flow rate of 0.1 ml/min throughout the experiment. The targets are added onto this buffer stream. The role of this *continuous* buffer stream is to efficiently remove unbound and/or non-specific accumulation of analytes near the QCM surface that can hinder the immunoreactions between incoming targets and the antibodies. The buffer stream also eliminates the flushing steps at the end of injection which facilitates faster analysis of the results. Further, a moving, rather than stationary sample medium more closely approximates the state of a 'real world' medium in which

the biosensor would be deployed. Because the size of a spore is too large (~1 μm) compared to an antibody (a few nanometers), the flow rate of target injection is important. A high flow rate will result in the spores being swept out without having a chance to bind to antibodies. Too low a flow rate will result in unnecessary accumulation of unbound analytes near the sensor surface, which hinders the binding events. Of course, the choice of optimal flow rate depends on the structure of a flowcell and the size of tubes. After numerous tests, the author found out a combined flow rate of 0.5 ml/min would be acceptable for this specific system.

4.2.3 Experiment Results Part I: Detection of *B. subtilis* spores

As mentioned above the flowcell houses two sensors which are subjected to the same environment to extract the real signature from the sensor responses. To achieve this, there needs be further requirement; the surface condition or the characteristic of the coating on each QCM before subject to the target should be the same. For example, if one QCM is coated with antibodies specific to a target, the other QCM also should be coated with certain antibodies, rather than left uncoated, by the same immobilization method. The control antibody used for this experiment was mouse monoclonal anti-FITC antibodies purchased from Sigma Chemical Company. Purified *B. subtilis* spore suspension purchased from STERIS Company was diluted in 1x TAE buffer solution making approximately 18000 spores per injection. Figure 4-4 presents the raw data of the frequency shift from each QCM sensor. Initially 1x TAE buffer solution was continuously flowing through the flowcell at a flow rate of 0.1 ml/min. At t=200, 0.3 ml of target solution containing the spores at a flow rate of 0.5 ml/min was added to the

stream of the TAE buffer. After the target injection was done and the system was stabilized, the anti- *B. subtilis* spore coated sensor made a permanent frequency shift of ~21 Hz which is indicative of the detection. The response of the anti-FITC coated sensor, however, returned to the baseline.

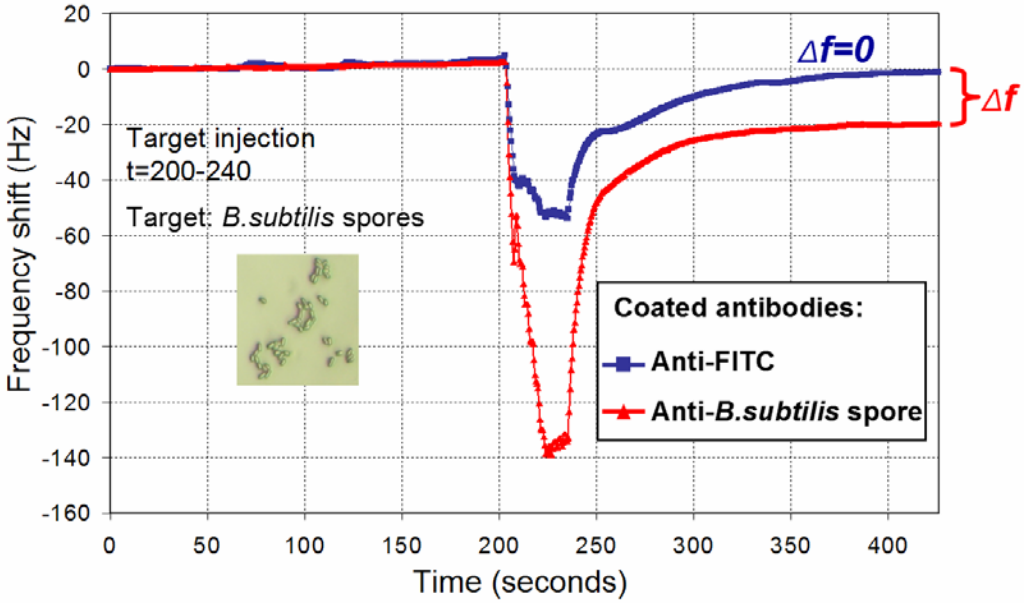

Figure 4-4. Response of the anti-FITC and anti-*B. subtilis* spore coated QCM sensors to the *B. subtilis* spore injection

This mass sensitivity was calculated from the result of this experiment. Assuming that the weight of a single spore is one picogram [37] and that the amount of immobilized antibodies is large enough to capture all the 18000 spores, the frequency shift of 20 Hz on 0.22 cm^2 electrode area results in the mass sensitivity about 4.1 ng/Hz-cm^2, or equivalently, 244 Hz/μg-cm. Although it is hard to measure, the actual sensitivity is expected to be slightly higher because some of the spores should not have bound to the antibodies.

As an independent confirmation of antibody capture of spores, the surfaces of the two sensors just undergone the experiment were examined. After *B. subtilis* spores detection experiment, the quartz plate of each QCM was disconnected from the package and rinsed with DI water and air dried for microscope observation. In figure 4-5(a), a noticeable amount of spores were still attached on the gold electrode surface of anti-spore coated QCM while spores can be hardly seen on the surface of anti-FITC coated QCM in figure 4-5(b). This result is indicative of the antibody-antigen binding as well as the specificity of the antibody to the *B. subtilis* spore.

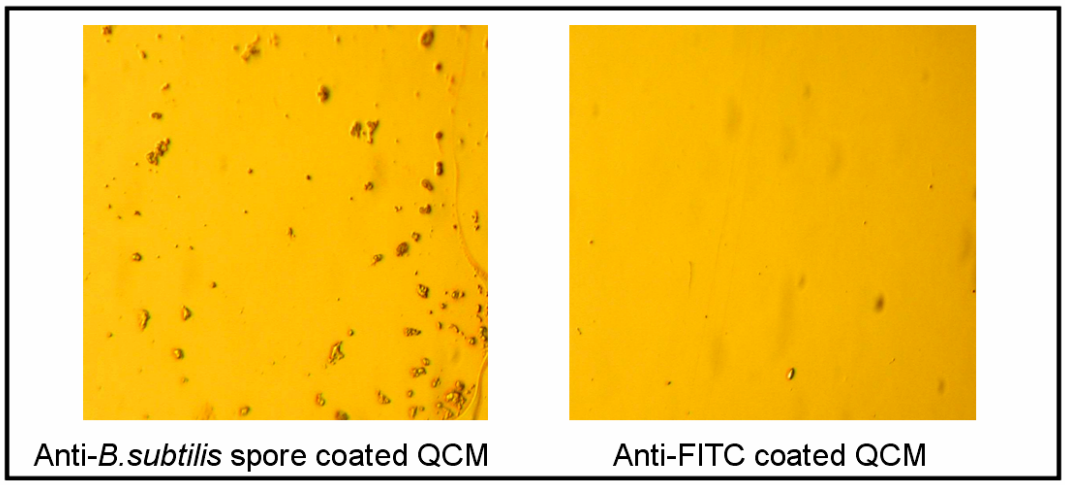

Figure 4-5. Optical microscope images of QCM surface after spore detection experiment. Anti-*B. subtilis* spore coated QCM (left) and anti-FITC coated QCM (right).

Even when the sensor system has been stabilized long after the target injection, a small random fluctuation of the frequency was still observe which can be considered as a system noise. This is the combined noise from the oscillator, frequency counter, and the mechanical vibration of the syringe pump. (Note that the syringe pump keeps injecting the medium through the flowcell). Actually, this noise is superimposed on the sensor

response over the entire sampling period. In order to be distinguished from the system noise, the amount of frequency shift of the sensor arise from the target detection should be greater than the amplitude of the system noise. Herein, the lowest detection limit is defined. In figure 4-6, the QCM response in Figure 4-4 is zoomed-in near the end of the sampling period (t=380-425). To estimate the lowest detection limit of our spore detecting sensor system, the final frequency shift in figure 4-4 (21 Hz for the 18000 spores) is mapped to the observed noise level in figure 4-6 (0.5 Hz). This gives an approximation of the lowest detection limit to be 428 spores.

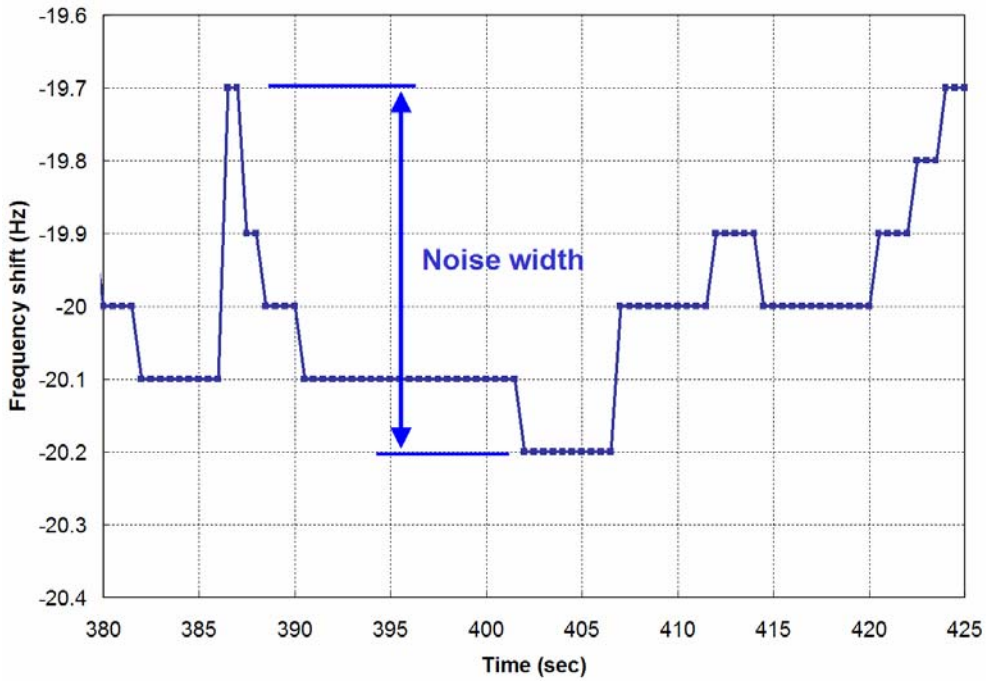

Figure 4-6. Frequency fluctuation when the system is idle; defining the noise level of the sensor

As a reference, the US Army estimates the number of anthrax spores that can infect people to be 8000-50000 although there is no supporting theory or background for this estimation. Table 4-1 summarizes the specifications and measured sensing

performance data of the dual-channel QCM sensor system from the author's spore detection experiment results.

Table 4-1. Specifications of the dual-channel QCM biosensor system used for the bacterial spore detection experiments.

Specs	Data	Remarks
Orientation, operating mode	AT-cut, TSM	0.17 mm-thick
QCM resonant frequency	9.995 MHz	Fundamental mode, unloaded
Effective sensing area	0.22 cm^2	Area of the gold electrode
Measured mass sensitivity	~4.1 ng/Hz-cm^2	1 spore ~ 1 picogram [ref. 37]
Measured system noise level	0.5 Hz	In idle mode
Lowest detection limit	~428 spores	Equivalent to ~428 picograms
Sampling rate of $\Delta f(t)$	0.5 second	
Medium flow rate	0.1 ml/min	1X TAE buffer
Target injection rate	0.5 ml/min	
Injecting apparatus	Syringe pumps	

4.2.4 Experiment Results Part II: Response to *B. subtilis* Vegetative Cells

Because the monoclonal antibodies immobilized on the QCM were raised against spores of a single *Bacillus* species, they are conceptually supposed to bind to the specific spores only. Therefore, the interested affinity of the antibody was to the spore of the target bacterium, not to the vegetative cell which is relatively easy to be eliminated with mild treatment. In this section, the author verifies that the antibody used in the spore detection experiment is indeed spore-specific, and does not cross-reacts to the vegetative cells from which it is derived. A sample of *B. subtilis* vegetative cells (unknown concentration) was obtained from School of Biology, Georgia Institute of Technology. To perform this experiment, the system setup in figure 4-2 needs to be slightly modified as shown in figure 4-7 because two different targets, spores and vegetative cells, are to be injected simultaneously. Instead of a dual flowcell, two identical single flowcells were

used with the same length of tubing to connect to the syringe pump. At this time, both QCM sensors were coated with anti- *B. subtilis* spore antibodies. The spores and vegetative cells in separate syringes but mounted on the same syringe pump were injected simultaneously to each single flowcell. The injected amount of the spore is the same as in the previous experiment.

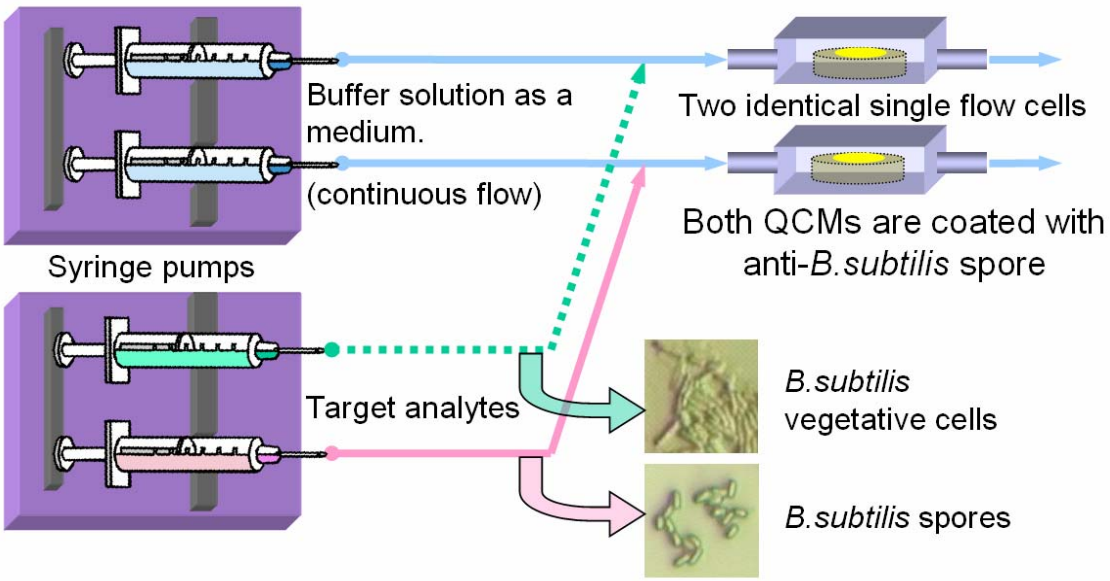

Figure 4-7. Modified QCM sensor system setup for the "spores vs. vegetative cells" experiment

In figure 4-8, the greater initial frequency shift in the response to the vegetative cells during the injection period seems to be attributed to their large size and/or mass compared to spores. As the vegetative cells are swept away by buffer stream, the frequency returns close to the base line. Because the sample is not purified vegetative cells, a small amount of sporulated cells that might have existed in the sample resulting in the baseline not completely returning to zero. In the case of spore injection, the response was similar to that in figure 4-4; the spores are bound on the QCM surface and made a

permanent frequency shift about 24 Hz, which is comparable to the 21-Hz shift in figure 4-4.

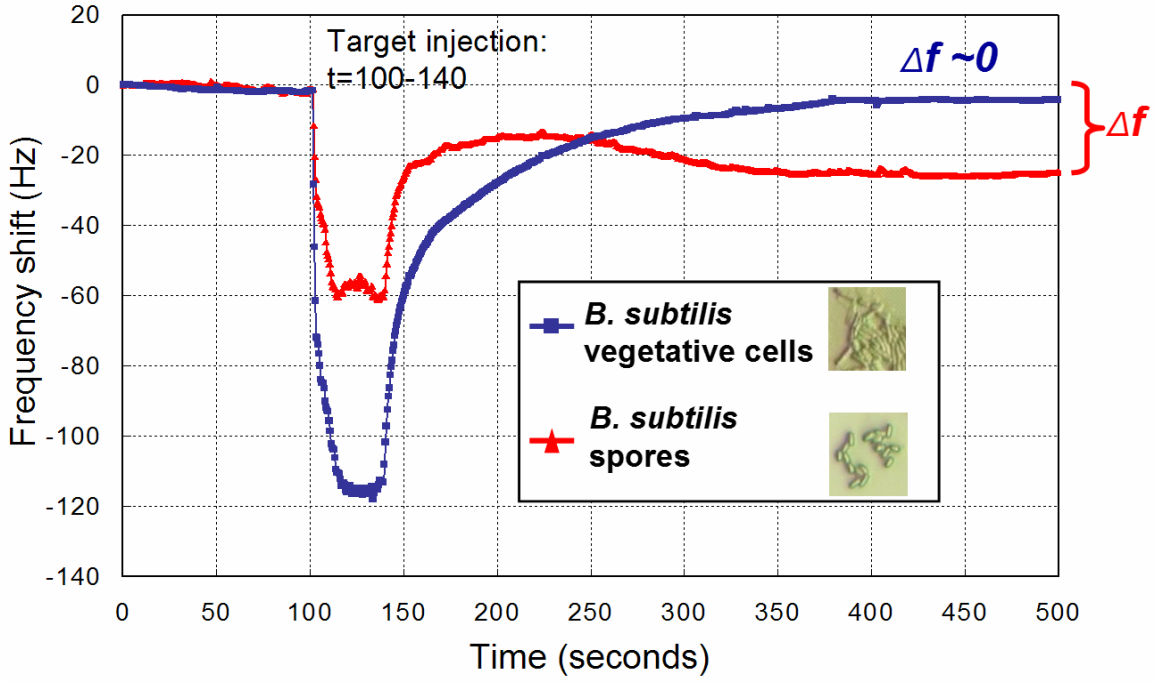

Figure 4-8. Response of the anti-*B. subtilis* spore coated QCM sensors to the *B. subtilis* spores and vegetative cells.

This result indicates that the QCM sensor system utilizing the anti- *B. subtilis* spore antibodies can distinguish the form of the potential pathogen; discriminating between the relatively benign vegetative stage of *Bacillus* and the potentially virulent spore form.

4.3 Conclusion

The data from a series of experiments presented a detection of bacteria spores by utilizing monoclonal antibodies specific to the target. The target was identified without time-consuming post process by using a dual QCM sensor. The QCM sensor was responding only to the target spores not to the negative controls. The results were further verified by taking optical microscope images of QCM surfaces that had just undergone

the experiment. The author concludes that QCM liquid phase immunosensors have the potential to become a valuable tool in detecting relatively large targets such as bacterial spores or proteins with rapid detection, high sensitivity, and ease of use. Recently, the author's research group was able to detect cancer marker proteins in cell line supernatant using the same dual QCM sensor system [38]. The requirements to achieve a QCM sensor include a proper system setup, stable immobilization techniques, and the availability of the specific antibodies.

CHAPTER 5

VAPOR PHASE DETECTION USING A SAW IMMUNOSENSOR ARRAY

5.1 Introduction

Vapor sensors, a.k.a. electronic noses, are becoming an increasingly popular analytical tool for detection and identification of targets in the gas phase. In this chapter, the author presents the results of a series of experiments demonstrating real-time vapor phase detection using a sensor system employing antibody coated two-port SAW resonators.

It is well understood that for antibodies or other biomolecules to maintain their tertiary (three-dimensional) structure and hence their prescribed functionality, they must operate in an aqueous environment. For this reason, vapor phase detection based on SAW immunoassay has been believed to be unlikely to occur due mainly to the liquid–unfriendly nature of SAW sensors. However, as a result of recent advances in acoustic device technology along with the development of better procedures for immobilizing more durable biolayers, there has been a steady influx in reports of SAW vapor phase immunosensor. For the study of SAW vapor phase sensors, the author designed and fabricated different types of two-port SAW resonators on ST-cut quartz substrates, and performed numerous detection experiments. This chapter briefly introduces the SAW resonator basics and the design procedure of the two-port 250-MHz Rayleigh SAW resonators specific to this study. Then the vapor phase detection experiments both in the laboratory and field conditions are presented.

5.2 Design and Fabrication of Two-Port SAW Resonators

SAW devices can be categorized in terms of the device structure, type and geometry of the IDT, and the number of ports (and hence the number of IDTs). There are two main configurations of the two-port SAW devices: delay lines and resonators. In both types the influence of the measurand on the acoustic wave phase velocity is utilized for the sensor effect, but the resonator structure provides lower noise levels and lower detection limit than similarly coated devices based on the delay lines [4]. The delay line structure has been previously shown in the figure 1-1 of chapter 1, which consists of two IDTs on the surface of a piezoelectric substrate, one to launch the SAW and the other to detect it. Because the excited SAW propagates in both directions from the IDT, there is an inherent 6 dB loss of power (3 dB at the input and 3 dB at the output) in the delay line structure. Using a resonator structure, this loss can be reduced or, ideally, eliminated.

Figure 5-1(a) presents a simplified diagram of a two-port SAW resonator. One IDT acts as an input transducer which converts the driving RF signal into an acoustic wave. The other IDT converts the acoustic wave back into an RF signal which is fed back into the attendant oscillator circuitry that drives the input IDT. The gratings on both sides of the IDTs form a resonant acoustic cavity. At the resonant frequency, the wave is trapped in the form of standing waves between the two reflector gratings. One of the fabricated resonators used for this thesis research is shown in figure 5-1(b). It has a center frequency of nominally 250 MHz with Al electrode metallization on a ST-cut quartz substrate. The mechanical properties of the ST-cut quartz have been described in section 2.2.4. More importantly for sensor applications, the ST-cut quartz is known to provide very high temperature stability near room temperature [18], which minimizes the need for

an additional temperature control unit. In this study, SAW resonators are used instead of the delay lines due to the aforementioned merits as well as their reported advantages [39,40] over the delay line counterparts. One practical drawback of the resonator structure, however, is that it requires strict accuracy of the spacing parameters, *e.g.* d_g and d_m in figure 5-1, in order to maintain the standing wave. The determination of the two-port SAW resonator spacing parameters is shown in section 5.2.3.

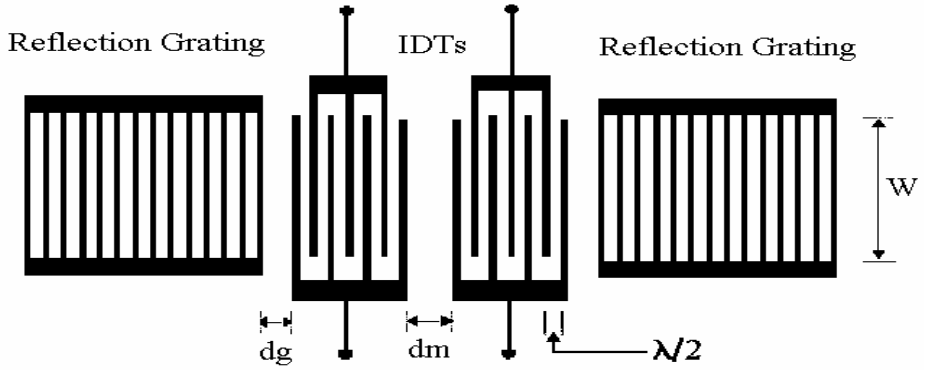

(a)

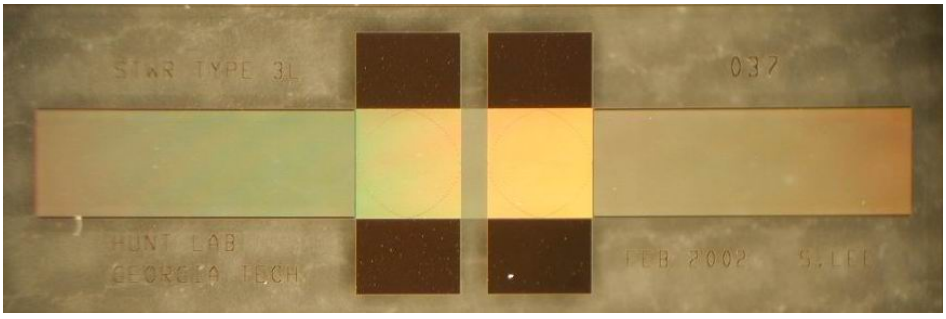

(b)

Figure 5-1. Two-port SAW resonator. (a) Simplified diagram. (b) Actual SAW resonator on a ST-quartz substrate fabricated at Hunt lab, Georgia Tech.

5.2.1 Interdigital Transducers (IDT)

The operating frequency of a SAW resonator is determined by the periodicity of the IDT fingers which is equivalent to the wavelength (λ) and is fixed by lithography. The phase velocity (V_a) of an unperturbed Rayleigh wave on a ST-cut quartz substrate is 3158 m/sec. From the relation $f_o = V_a / \lambda$, the required periodicity or wavelength to get the 250-MHz center frequency is about 12.5 μm. Figure 5-2 illustrates different types of the IDT design in common use. The acoustic aperture (W) is defined as the overlapping length of the electrode pair.

If the metallization ratio (η) is 50%, *i.e.*, the finger width is equal to the space between fingers, the width of each finger for the uniform IDT with single-electrode in figure 5-2(a) would be λ/4. The single-electrode transducers are widely used because of its structural simplicity and lower lithographical resolution. However, the structure is virtually equivalent to a grating with periodicity of λ/2 which satisfies the Bragg condition [15]. In this case, a portion of acoustic wave reflects from the edge of the IDT fingers and this can degrade the characteristic of the device especially when the number of the IDT finger is large. Therefore it is more common to use split-electrode or double-electrode transducers as shown in figure 5-2(b) to suppress Bragg reflections. It has been verified that the phase of the reflected wave from each split-electrode pair cancels out at center frequency [41]. However, the split-electrode requires increased lithography resolution for the same operation frequency. For example, the finger width of each IDT finger would be λ/8 for 50% metallization ratio. Hence, the IDT finger width is reduced to ~1.5 μm for the 250-MHz center frequency and this is the minimum feature size of the SAW resonators designed for this thesis work.

The electrode overlaps or the acoustic aperture (W) in figure 5-2 can be spatially varied to shape the frequency response using a technique called 'apodization', suggested by Tancrell *et al*. [42]. Figure 5-2(c) shows an apodized IDT. It is well known that the IDT of SAW devices can be modeled by delta function [43,44]. Following the delta-function model, the apodized IDT can be regarded as a sequence of equally-spaced sources whose amplitudes (proportional to the overlaps) can be arbitrary, and the spatial shape of these overlaps, given by the apodization, is essentially a scaled version of its impulse response [44]. This implies that an IDT can be designed simply by Fourier transformation of the desired frequency response, using the resulting time-domain function to determine the electrode weights, or apodization. This property was demonstrated by Hartemann *et al* [45]. In a uniformly overlapped IDT, the frequency response will be a sinc function, which is the inverse Fourier transform of a rectangular function. The IDT with a Gaussian apodization in figure 5-2(c) would result in a Gaussian shape in the frequency response. The apodization inevitably results in spaces outside the overlapping region between electrodes and the opposite bus bar, and these cause wavefront distortions due to the nonuniformity of the IDT pattern. In 1971, Tancrell and Williamson first suggested the use of 'dummy electrodes' to improve the uniformity of SAW velocity [46]. These passive electrodes do not generate SAW because the adjacent electrodes are of the same polarity, but maintain the uniform electrostatic profile and thus a constant phase velocity across the aperture. The efficiency of the dummy electrodes has been further verified by Hunsinger and Datta [47]. For the vapor phase detection experiments herein, SAW resonators with split-electrode and apodized IDTs with dummy electrodes were employed, but all the three types in figure 5-2 were fabricated and tested for comparison.

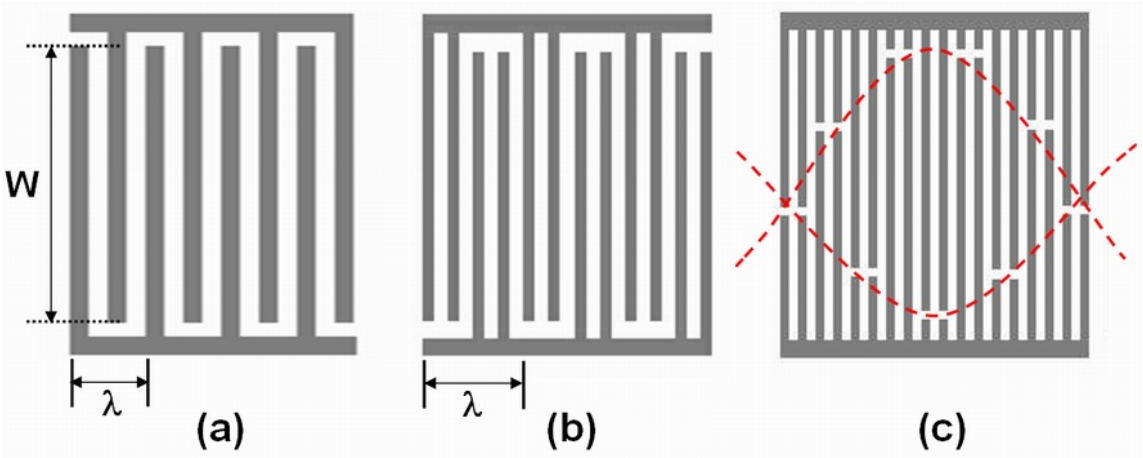

Figure 5-2. Types of IDTs. (a) Single-fingered, uniform aperture (b) Split-electrode, uniform aperture (c) Split-electrode, apodized IDT with dummy fingers.

5.2.2 Reflector Gratings

The reflector gratings in SAW resonators plays an important role as they reflect the acoustic wave and form a standing wave in the cavity region. Without reflectors, a SAW resonator would behave as a delay line filter. With the gratings included, the effect of a grating around the center frequency will be superimposed on the delay line response. Unlike the electromagnetic waves in the transmission line where a total reflection can be achieved by single reflecting element, an acoustic wave has a more complicated reflection mechanism. This is because multiple components are coupled to give a total flow of acoustic power and the signs or phases of the reflection coefficients from each component are not the same [44]. For example, the Rayleigh wave has both longitudinal and shear components with 90° phase difference, and hence a single metal strip cannot realize a total reflection of both components. Consequently, a reflection of SAW requires multiple numbers of periodically spaced metal strips where the contribution of each finger's reflection adds constructively to yield higher reflectivity. The reflection coefficient of SAW is commonly referenced to the surface potential (φ) [43] because the

field quantity φ can be treated as the amplitude of the wave and can be detected by the IDT.

It is known that wave fields reflected at each metal strip are in phase and will sum up when the period of the grating satisfies the Bragg condition [15]

$$2p = n\lambda \text{ or } \frac{2\pi p}{\lambda} = n\pi \qquad (5.1)$$

where p is the grating period and n is an integer. For the simplest case (n=1), the Bragg condition is satisfied when the grating period is half a wavelength. The magnitude of the total reflection coefficient (R) at the center frequency can be approximated as [43]

$$|R| \simeq \tanh(N|r|) \qquad (5.2)$$

where N is the number of metal strips and r is the reflection coefficient from a single metal strip. The overall reflection from the grating structure can be treated as if the reflection is done by a single ideal reflector. Because the wave decays into the reflector array, the point of this virtual reflection is located at a certain distance from the edge of the reflector. This distance is defined as the *effective center of reflection* and can be approximated to [43]

$$L_e \simeq \frac{\lambda}{4|r|} \qquad (5.3)$$

It is a function of the amplitude of the reflectivity, hence a function of the piezoelectric coupling; a SAW resonator on a substrate with a high K^2 coupling factor would have the effective center of reflection close to the reflector edge, and vice versa. The effective center of reflection is very important because it is used for the calculation

of the effective cavity area which is equivalent to the effective sensing area if used as a sensor.

The metal strips in the reflector can be placed either unconnected (open circuited) or connected (short circuited) as shown in figure 5.3. Both types can serve as a reflector but the magnitude of the reflection coefficient is not the same for the same substrate and the phase can be significantly different for strong piezoelectric material such as lithium niobate. The reflectivity of each metal strip (r) for the short-circuited grating is calculated for two different piezoelectric materials [43]

$$r = j(-0.75\frac{K^2}{2} - 0.51\frac{h}{\lambda}) \quad \text{for ST-quartz} \qquad (5.4a)$$

$$r = j(-0.75\frac{K^2}{2} - 0.24\frac{h}{\lambda}) \quad \text{for YZ-LiNbO}_3 \qquad (5.4b)$$

where K^2 is the piezoelectric coupling coefficient and h is the aluminum film thickness. Considering that the film-to-wavelength ratio (h/λ) are usually very small (<0.01), the grating reflectivity on a strong piezoelectric material is not so much affected by the h/λ ratio, whereas the reflection on a weak piezoelectric material like quartz is almost dominated by h/λ ratio.

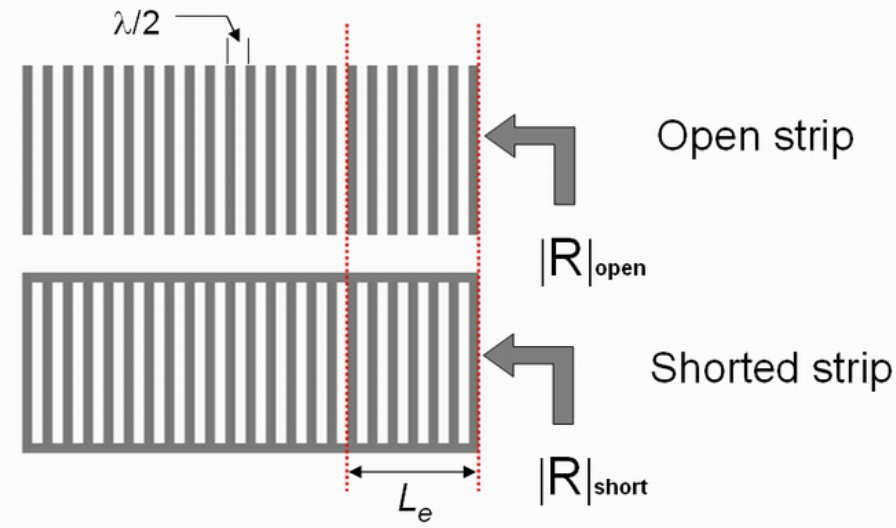

Figure 5-3. Open- and short-circuited reflector gratings.

The reflection coefficient in equation (5.4) was calculated for ST-X quartz and YZ-lithium niobate and summarized in Table 5-1. For these calculations, typically used values for the metallization ratio and the film-to-wavelength ratio were used, which are η=0.5 and h/λ ~0.01 respectively.

Table 5-1. Calculated reflection coefficient for the aluminum grating with η=0.5 and h/λ ~0.01 (After references [43,44,48])

Substrate material and type of the reflector	Relative magnitude of *r*	Phase of *r*
ST-X quartz (open circuited)	0.705	-π/2
ST-X quartz (short circuited)	1	-π/2
YZ lithium niobate (open circuited)	2.55	**π/2**
YZ lithium niobate (short circuited)	3.52	-π/2

The main reason for the radical change in phase for the open-circuited reflectors on the lithium niobate is due to its high electromechanical coupling coefficient (K^2). If

the strips are not shorted to each other, a voltage is induced which alternates in polarity from strip to strip just as in IDT. On a strong piezoelectric substrate, this causes additional regeneration reflection [48] that should be considered. In the specific case of lithium niobate, this spurious reflection has the opposite phase but a larger magnitude making the overall reflection phase reversed. However, there is no such problem in a short-circuited reflector. This enables us to use the same resonator design and spacing parameters for the fabrication of SAW resonators both on weak and strong piezoelectric substrates. For example, the lithium niobate resonator in figure 2-11(b) was fabricated with the same photomask used for the quartz SAW resonators. As can be seen in the table 5-1, for the same substrate material the reflector with shorted strips gives a larger reflectivity. Because of the aforementioned advantages, the short-circuited reflector is preferred for the practical design, and was also chosen for this thesis work. For the SAW resonators herein, 501 fingers are placed in each of the gratings and these are equivalent to 250λ with $|R|$=98.8%. The effective center of reflection L_e = 41.2λ from the reflector edge.

5.2.3 Determination of Spacing Parameters

As discussed in the previous sections, a two-port SAW resonator requires strict accuracy of the spacing parameters to maintain the standing wave. In this section the determination of important spacing parameters is described. Two important parameters in the design of the SAW resonator are d_g and d_m (shown in figure 5-1a), the distance between grating and IDT and the distance between two IDTs respectively. The IDT-IDT gap will be considered first. Like in the previous section, the metallization ratio η=0.5 is

assumed. Figure 5-4 is a sagittal diagram of the IDT area of a SAW device showing the amplitude of the standing wave at the resonant frequency.

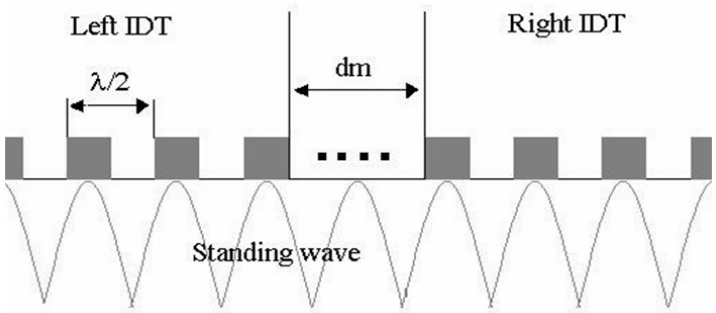

Figure 5-4. Determination of d_m, the spacing between the two IDTs.

The first requirement is that the two IDTs should be spaced so that the fingers are positioned above maxima of the standing wave. Considering the wave pattern and geometry in figure 5-4, the minimum possible distance is easily found as λ/4. The IDT position can be moved out by an integer of half-wavelengths (or the wavelength of the standing wave) such that

$$d_m = \lambda/4 + n\,\lambda/2\ ,\ (n = 0,1,2,3\ldots) \qquad (5.5)$$

The gap between IDT and reflector grating can be determined in similar way but there are more things to be considered. The physical reflection begins at the edge of the first grating element. The *j* term in equation (5.4) can be eliminated if the leading edge of the first element is chosen as a reference plane of reflection [49]. By doing this, the reflection coefficients in equation (5.4) and Table 5-1 now become real values and the analysis is much easier by treating the acoustic standing wave like a voltage or current

wave in transmission lines. Figure 5-5 is a sagittal diagram of the SAW device showing only the left reflector and IDT with the reference plane being the leading edge of the reflector. Because the SAW resonators are symmetric, the determination of the spacing parameters for the other side can be done in the same way.

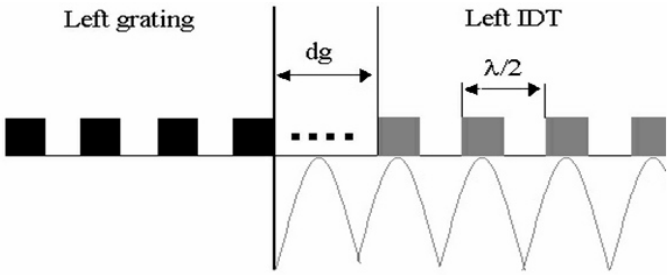

Figure 5-5. Determination of d_g, the spacing between the reflector and IDT.

Examining the wave pattern in figure 5-5, the first maximum of the standing wave is located λ/4 away from the reference plane, which gives the minimum possible distance between IDT and reflector to be λ/8 for η=0.5. Again, the spacing can be extended by an integer of half-wavelengths such that

$$d_g = \lambda/8 + n\,\lambda/2\ ,\ (n = 0,1,2,3\ldots) \qquad (5.6)$$

Note that the spacing parameters d_g and d_m are measured between inner edges, not center-to-center.

Because this configuration, termed *optimal* spacing, is based on the standing wave reflection and the sign of the reflection coefficient at the boundary, it provides minimum insertion loss for a given design. However, the d_g can be alternatively determined such that the metal strips of the reflector and IDT are placed in homogeneous fashion. This

configuration is termed *synchronous* spacing and first proposed by Cross *et al* in 1979 [50]. In this synchronous structure, the IDT fingers are placed in spatial synchronism with the grating strips. This can be done by extending d_g by another λ/8. The same reference reported that the synchronous gap suppressed spurious longitudinal modes and achieved Q-values of over 10000 in a SAW resonator with relatively large number of IDT and reflector strips. However, the frequency response is not symmetric and the resonant frequency drops from the designed value. The insertion loss is also increased because the slight displacement of the gap from the optimal configuration compromised the efficiency of the reflection. Herein, the optimal d_g was chosen for the vapor phase experiments because the observed spurious modes were not significant enough to degrade the sensor performance. Also the symmetric frequency response is favorable for the sensor system to keep track of the resonance peak when the acoustic wave is damped by biolayer coating or target detection.

For the SPA antibody immobilization protocol described in chapter 3, the antibodies are supposed to attach to the metal electrodes but not to the quartz surface. Therefore, it is desired to minimize the amount of bare quartz in the cavity region as shown in figure 5-6(a). This would achieve a uniform distribution of biomolecules in the SAW resonator's most sensitive region as well as to keep the homogeneity on the surface. Selecting the minimum possible value for d_m can aid in the achievement of this goal. In case the immobilization needs to be done between the IDTs, d_m can be increased as shown in figure 5-6(b), but the location of IDTs and gratings should be calculated with high accuracy to avoid signal degradation. The design parameters of the SAW resonators used in this experiment are summarized in Table 5-2.

Table 5-2. Design parameters of the 250-MHz Rayleigh SAW resonator

Wafer material and orientation	ST-cut quartz, X-propagation
Acoustic aperture (W)	850 μm
Number of grating fingers	501 per reflector
Number of IDT finger pairs*	50 per IDT
IDT-grating gap (d_g)	7.8 μm (optimal spacing: see section 5.2.4)
IDT-IDT gap (d_m)	3.1 μm (minimum)
IDT pitch ($\lambda/2$)	6.2 μm
IDT finger width (split-electrode)	1.5 μm
Grating pitch ($\lambda/2$)	6.2 μm
Effective center of reflection (L_e)	41.2 λ
Metal film thickness	1400 Å
Film-to-wavelength ratio (h/λ)	0.011
Metallization ratio η	0.5
Diced chip size	8100 x 1980 μm

* One finger pair consists of *four* fingers because of the split-electrode configuration.

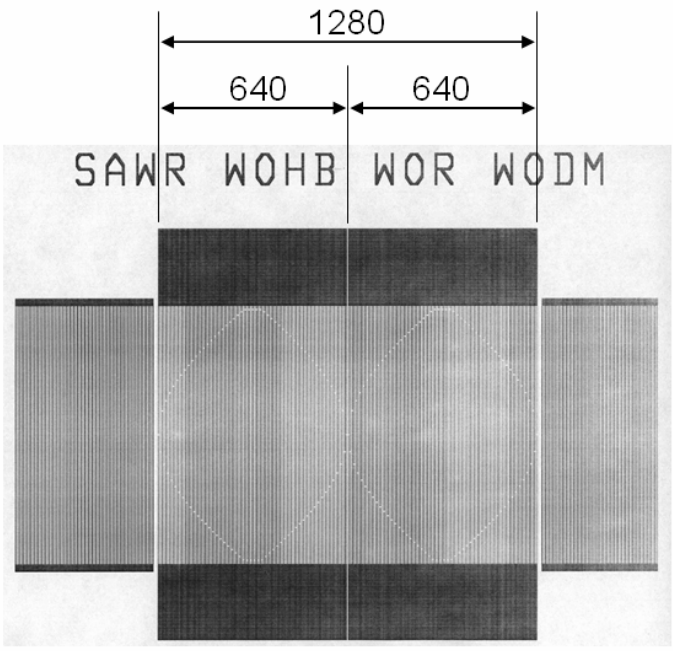

(a)

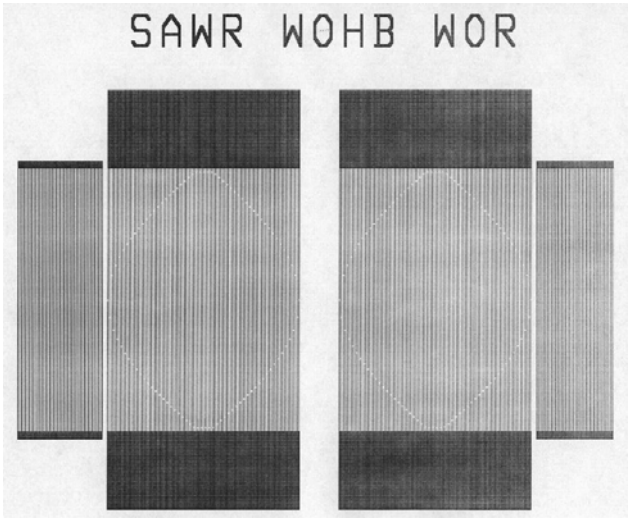

(b)

Figure 5-6. Actual layout of the 250 MHz Rayleigh SAW resonators. (a) Minimum d_m. (b) d_m=10 λ. The reflector gratings are truncated in the picture. Measurements are in microns.

5.3 SAW Vapor Phase Sensor Array

5.3.1 Significance of a Reference Sensor

In the acoustic wave sensors utilizing the frequency shift as an indication of the detection, any mechanical perturbations can result in frequency changes. For resonators and other devices where the entire bulk is used as a sensing interface, this process is technically irreversible. This means that many parameters may contribute to the frequency changes, but the reverse determination of each perturbating source from a measured frequency shift is very ambiguous, if not impossible. Therefore, the analysis of the sensor signatures obtained only from a single sensor unit may incur incorrect results and thus should be avoided. A simple but effective solution of this problem is the use of a reference sensor. A reference sensor is physically identical to the measuring sensors but treated not to be sensitive to the perturbation of main interest and exposed to the exactly same environment. In the dual QCM sensor setup described in chapter 4, a complementary QCM sensor coated with antibodies not specific to the target was employed to monitor any spurious perturbations. This schematic can be applied in the same way for the vapor phase SAW sensor array. Suppose a signature $\Delta f_{test}(t)$ was obtained from a SAW immunosensor as shown in figure 5-7(a), where $\Delta f_{ref}(t)$ was a signature from the reference sensor in the same environment. In addition to the real binding events of interest, $\Delta f_{test}(t)$ includes the effect of pneumatic pressure and external vibrations which were being monitored by the reference sensor. The frequency shifts from those unwanted perturbations are excluded by subtracting $\Delta f_{ref}(t)$ from the signature $\Delta f_{test}(t)$. The result is shown in figure 5-7(b), where the frequency changes caused by all the spurious influences were removed.

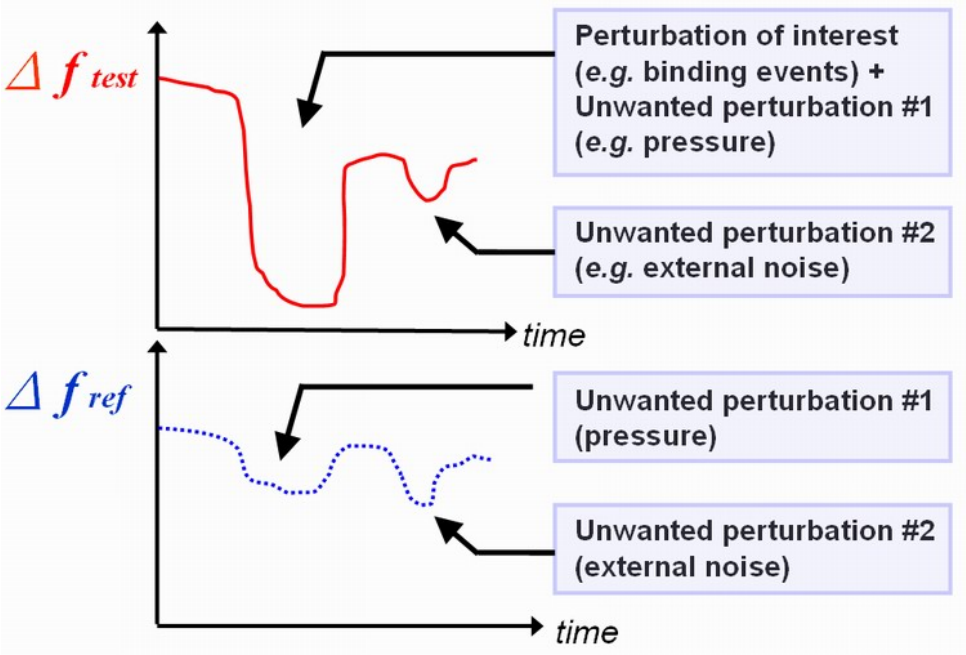

(a)

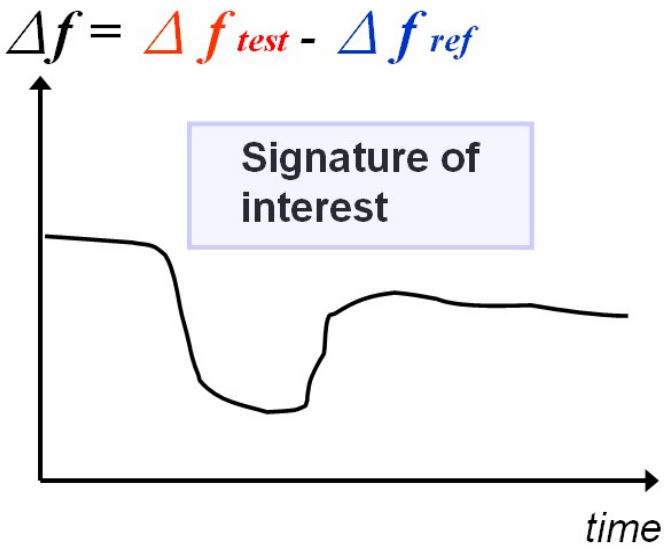

(b)

Figure 5-7. Role of a reference sensor. (a) Example signature from a measuring sensor (top) and a reference sensor (bottom) (b) Compensated signature where the frequency changes from spurious influences cancelled out by the reference sensor.

This configuration of the reference sensor will be used in the SAW resonator sensor array for the vapor phase experiments. However, there is a requirement for this reference sensor schematic to be valid; the manufacturing of the flowcell should be high-precision such that all the sensor housings in the array are physically identical.

5.3.2 SAW Sensor System Setup

Figure 5-8 schematically illustrates a single channel vapor phase biosensor with an immobilized monolayer of antibodies on the surface of a SAW device. The diagram shows a SAW delay line with the biolayer coated between the IDTs, but the actual sensing element herein is a two-port SAW resonator and the biolayer is uniformly coated on the entire surface. The device is then mounted together with other SAW sensors into an oscillator circuit, and frequency changes are precisely measured.

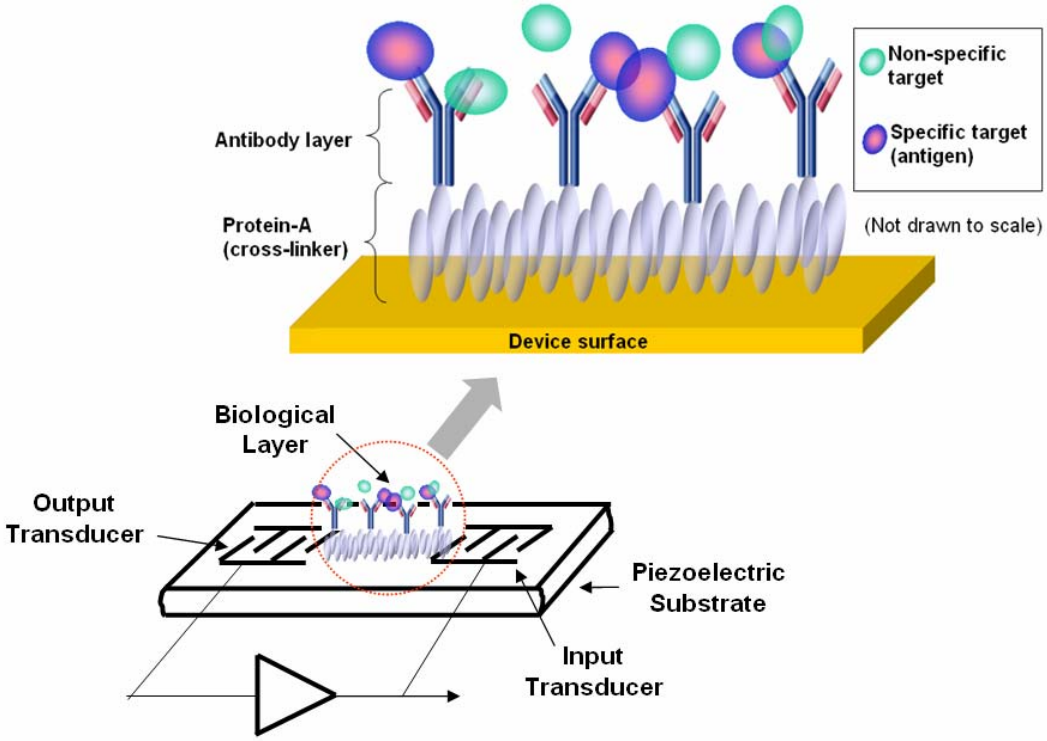

Figure 5-8. SAW immunosensor with a detecting biolayer immobilized.

The SAW sensor system setup for the vapor phase detection shown in figure 5-9 is analogous to the QCM sensor system in figure 4-2. The pneumatic flowcell housing can hold up to four identical SAW resonator sensors mounted on TO-8 packages with one sensor being the reference. The real-time frequency data from each sensor is transferred to the PC through RS232C serial ports. As discussed in section 5.3.1, the frequency data from the reference sensor are subtracted from each detecting sensor's response. The 250-MHz two-port Rayleigh wave SAW resonators were designed and fabricated by the author following the procedure described in section 5.2 and the antibodies were immobilized using the SPA crosslinker as seen in section 3.2.2. The air flow rate of the built-in pump is 180 ccm. Flowcell and oscillator circuitry were purchased from Microsensor Systems, Inc.

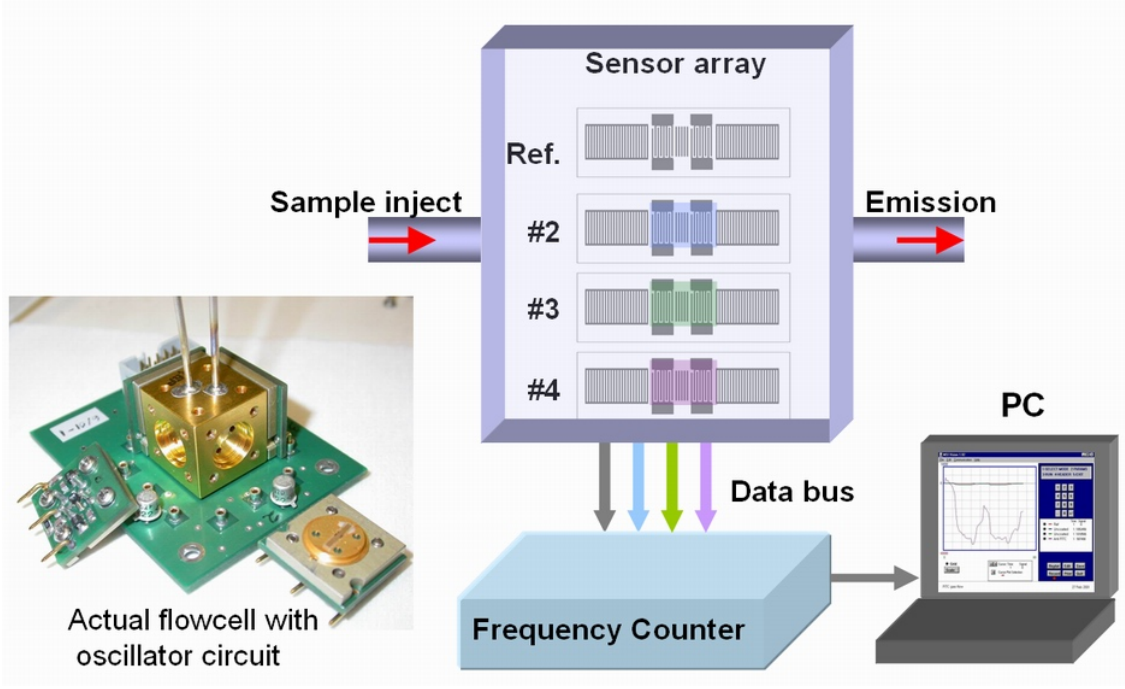

Figure 5-9. Schematic of the SAW resonator array vapor phase sensor system.

5.4 Experimental Results

5.4.1 Uranine Vapor Detection

As an initial test of functionality of the sensor system, the experiments were done with the anti-FITC antibodies and uranine vapor. The specificity of the anti-FITC antibodies to the uranine molecules has been verified by the fluorescent immunoassay described in section 3.3. The anti-FITC/SPA complex was immobilized onto the SAW resonator #4 in figure 5-9 while the two control sensors #2 and #3 were coated with hydrogel only. The uncoated reference sensor #1 was mounted in the same flowcell with other sensors and subjected to the same physical environment. The SAW resonators in the sensor array differ only in the nature of the film coated onto the surface. In every other way they are identical.

For vapor presentation, nitrogen gas was bubbled through a 1 nM solution of the analyte at a flow rate of 0.5 SLPM. The built in pneumatic pump sampled the vapor twice at t=20 and t=40 for 15 seconds of cycle each. Figure 5-10 shows the simultaneous response of an anti-FITC coated sensor and two control sensors to the uranine vapor. With the introduction of the uranine vapor, the device responds with a dramatic downward frequency shift and when the pump is turned off the response settles to a baseline which is shifted from the original device frequency. The second presentation of the vapor further decreases the frequency resulting in a permanent baseline shift about 10 kHz. This represents direct evidence of molecular recognition in the vapor phase. The control sensors show neither a dramatic response to the uranine nor do they show any baseline shift. This is a typical response for a non-specific control device and the return to

baseline indicates that little of the analyte has permanently attached itself to the surface of the SAW device.

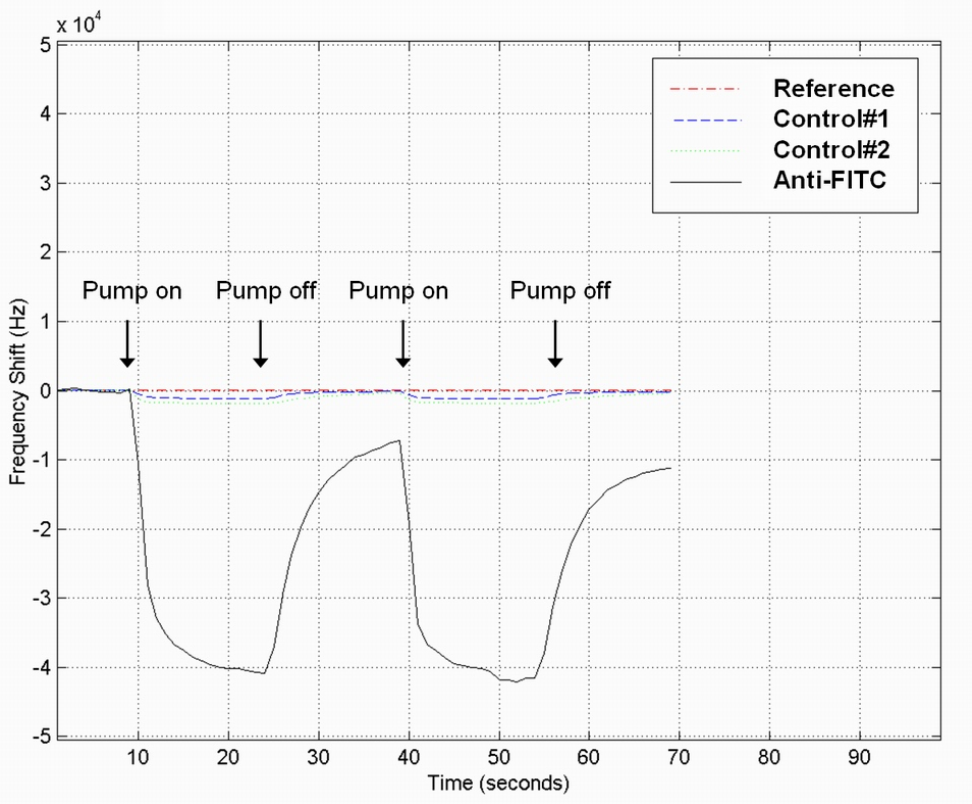

Figure 5-10. Response of SAW resonator sensors to uranine vapor. Control sensors are not coated with anti-FITC antibodies.

One of the author's findings from the fluorescent immunoassay in chapter 3 was that the anti-FITC antibody did not capture the Alexa molecules which are similar in structure to an uranine molecule. Because the immunoassay in chapter 3 was mainly intended to assess the antibody immobilization protocol, the frequency response was not monitored during the experiments. At this time, SAW devices with and without anti-FITC antibody films are tested against the Alexa vapor and the sensor signatures are recorded in real-time. The same method and concentration of the analyte as in the

previous experiment were used for the vapor generation. The Alexa vapor samples were drawn for two different 15 second periods (20 to 35 seconds and 100 to 115 seconds). Figure 5-11 shows the response of an anti-FITC coated SAW resonator and a control SAW resonator to the Alexa vapor. Neither of the devices shows a dramatic response to the analyte (initial Δf is about 500 Hz compared to 40 kHz for uranine) and both the control device and the anti-FITC coated device show no evidence of a marked baseline shift. This would indicate there is no binding of the Alexa to either of the device surfaces.

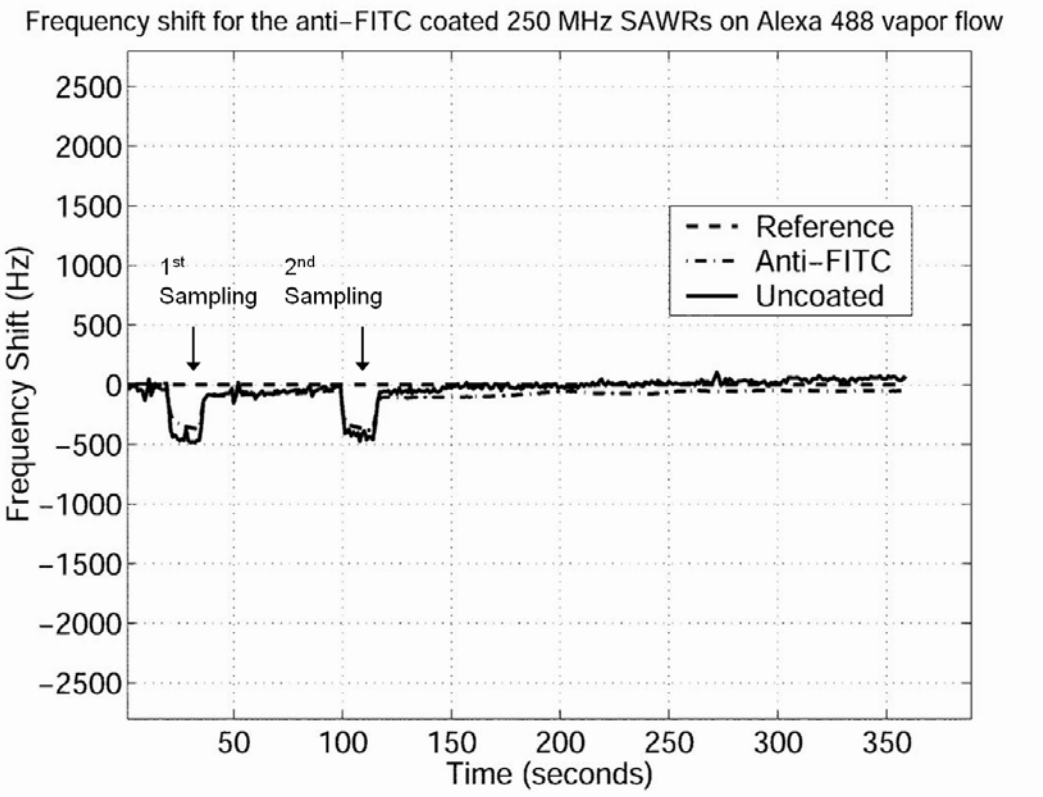

Figure 5-11. Response of SAW resonator sensors to the Alexa Fluor® vapor showing minimal frequency changes.

5.4.2 Cocaine Detection Part I: Laboratory Test

Subsequent to confirmation of the sensor system's functionality using the fluorescent analytes, the experiments were performed using cocaine vapor as a target. For these experiments, anti-benzoylecgonine (BZE) antibodies were utilized for the detection of cocaine molecules. Cocaine and BZE are structural analogs with the latter being the predominant metabolite breakdown product of the former. They differ only by a methyl group that forms a methyl ester with C'12 in cocaine that is cleaved when hydrolyzed to form the acid derivative in BZE. The chemical structure of a BZE molecule is compared with a cocaine molecule in figure 5-12.

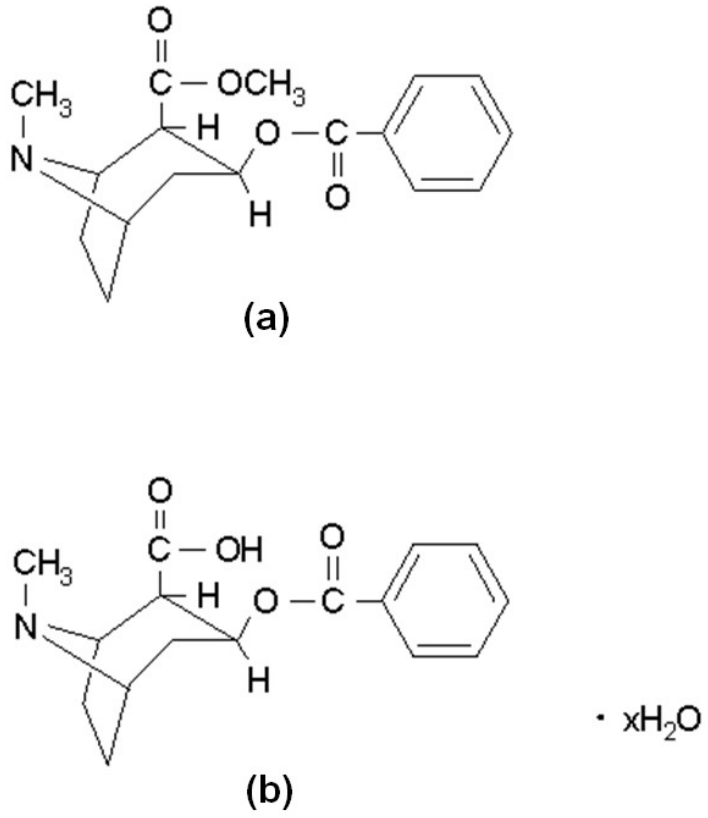

Figure 5-12. Structure of (a) cocaine molecule, and (b) benzoylecgonine (BZE), a metabolite of cocaine

The location of the structural difference between the two molecules does not appear to be a part of the epitope recognized by anti-BZE. As a control, both anti-FITC coated and hydrogel-coated devices were employed. One motivation for using anti-FITC as a negative control is that both anti-BZE and anti-FITC monoclonal antibodies are specific for small molecules which have molecular weights in the range of 300 Daltons. In addition, the two molecules, cocaine and FITC, may possess a hydrophobic epitope.

Using anti-BZE antibodies immobilized onto SAW resonators, it was possible to consistently detect cocaine presented using the INEEL (Idaho National Engineering Laboratories) vapor generator designed specifically for the purpose of testing analytical equipment. The INEEL vapor generator is calibrated to release a specific amount of cocaine when a particular temperature, flow rate and pulse time is entered (Data available at Houston's Research Labs). The cocaine pellets housed within a separate compartment are heated at a constant temperature that corresponds to a known amount (~1 ng in this case) of cocaine molecules that can be pulsed into the sensor array containing four SAW resonators with oscillating circuits.

Figure 5-13(a) presents the response of the SAW resonator sensors to 1 ng of cocaine from the INEEL vapor generator. The anti-BZE sensor response shows a radical increase of frequency in the pulse duration and gradually decays after pulse is off, finally resulting in a permanent baseline shift about 4.5 kHz. Note that the slope of $\Delta f(t)$ after pulse duration is much less than the slope at the beginning of the pulse. This is because the unbound molecules exit from the sensor array only by diffusion. For this reason it takes considerable time for the sensors to return to the equilibrium. The responses of the control sensors were minimal. The anti-FITC coated sensor had some small frequency

changes but the baseline shift was not observed, indicating that there was no binding of cocaine molecules to the anti-FITC coated sensor. The uncoated sensor did not make any marked response.

To check the functionality of the anti-FITC coated sensor that was not reactive to cocaine, the experiment was performed again with the same sensor array but uranine vapor was injected instead of cocaine. After air-purging of the system, the built-in pneumatic pump sampled uranine vapor. Figure 5-13(b) presents the response of anti-BZE, anti-FITC, and uncoated sensors to uranine vapor sampled twice from 1 nM of uranine solution over 100 second intervals. The frequency shift during the exposure to uranine was very dramatic for the anti-FITC coated device and only a slight response for the anti-BZE device is observed. The result of this experiment verified the specificity of the antibody that can discriminate between the small molecules with similar weight. It also proved that the anti-FITC coated devices are a good choice as a reference or control sensor in the immunosensor array for cocaine detection.

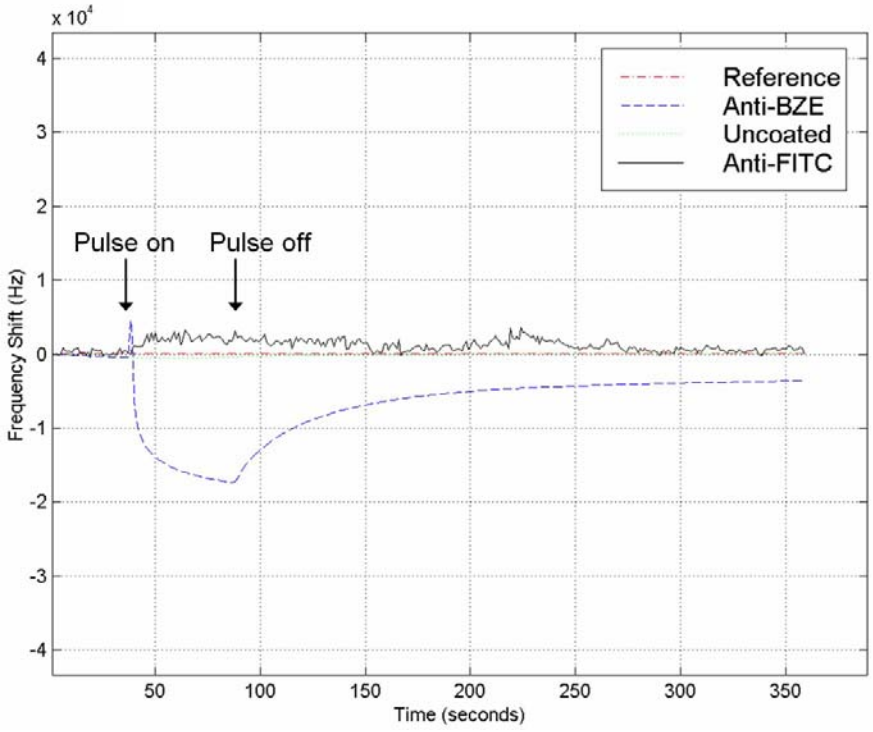

(a)

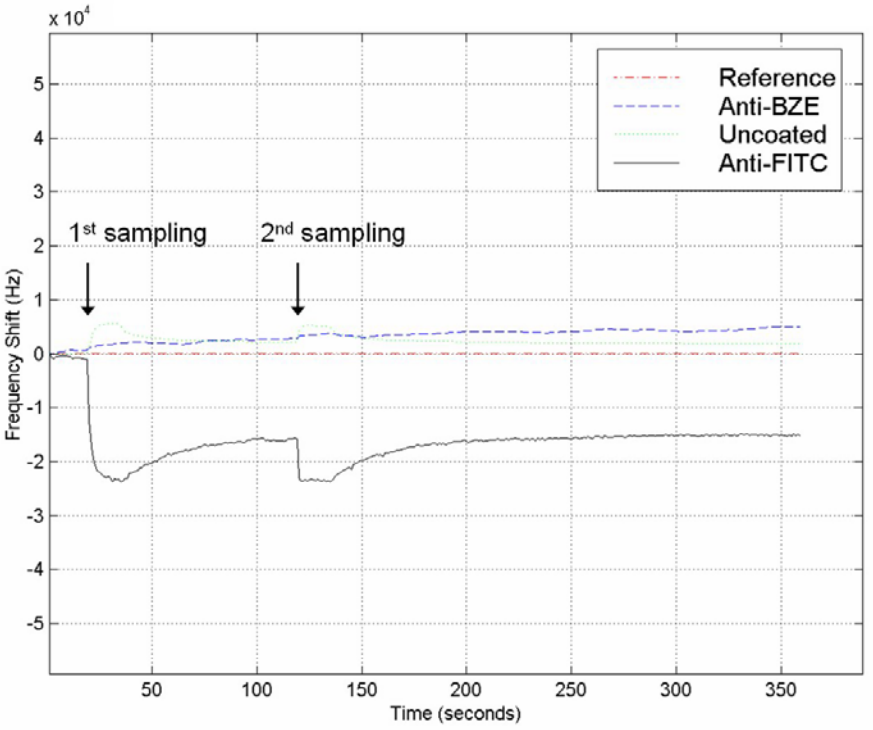

(b)

Figure 5-13. Response of the SAW immunosensor array to (a) pure cocaine pulse from the INEEL vapor generator, and (b) sampled uranine vapor

The INEEL vapor generator has an auxiliary connection that can supply clean air to purge the air path, check air leaks, or perform system maintenance. The author experimentally found out that if the clean air is supplied through the system with a constant and appropriate flow rate as a background, a distinct type of sensor signature can be obtained.

The previous cocaine detection experiment in figure 5-13(a) was done without the constant air flow, *i.e.,* the air flow exists only for the pulse duration. This was the reason for the gradual slope of the signature $\Delta f(t)$ and slow recovery to the baseline frequency after the pulse is off. This setup is good for observing how the baseline shift is formed and how the devices are saturated after each pulse is over because the system is free of external disturbances after the sampling is done. With the air supply is connected, clean air always flows at a constant rate regardless of the pulse being on or off. When the pulse is on, the cocaine vapor, with a minimal flow rate, is simply added to the air stream and carried through the nozzle to the sensor array. This schematic is analogous to the constant buffer medium flow in the flowcell of the QCM sensor system in chapter 4.

One of the important observations is that the flow rate and the pressure gauge level of the air flow were held constant regardless of the pulse. In other words, the addition of cocaine molecules to the air stream during the pulses did not modulate the flow rate or caused a significant variance in pressure values. This enables us to assert that any frequency shift after the initial onset of airflow cannot be attributed to changes in aerial quality, but is solely due to the perturbation of the device surface by the cocaine molecules mixed in the airflow. This implies that there is no need for considering the pressure changes as a factor of the frequency shift. Figure 5-14 presents the response of

anti-FITC, anti-BZE and hydrogel-coated sensors to a 1 ng pulse of cocaine over 5 second intervals. The flow rate of the air supply was setup to 180 ccm which is similar to the flow rate of the built-in pneumatic pump in the sensor system. Two pulses of cocaine vapor were injected into air-stream that flows to the sensor array.

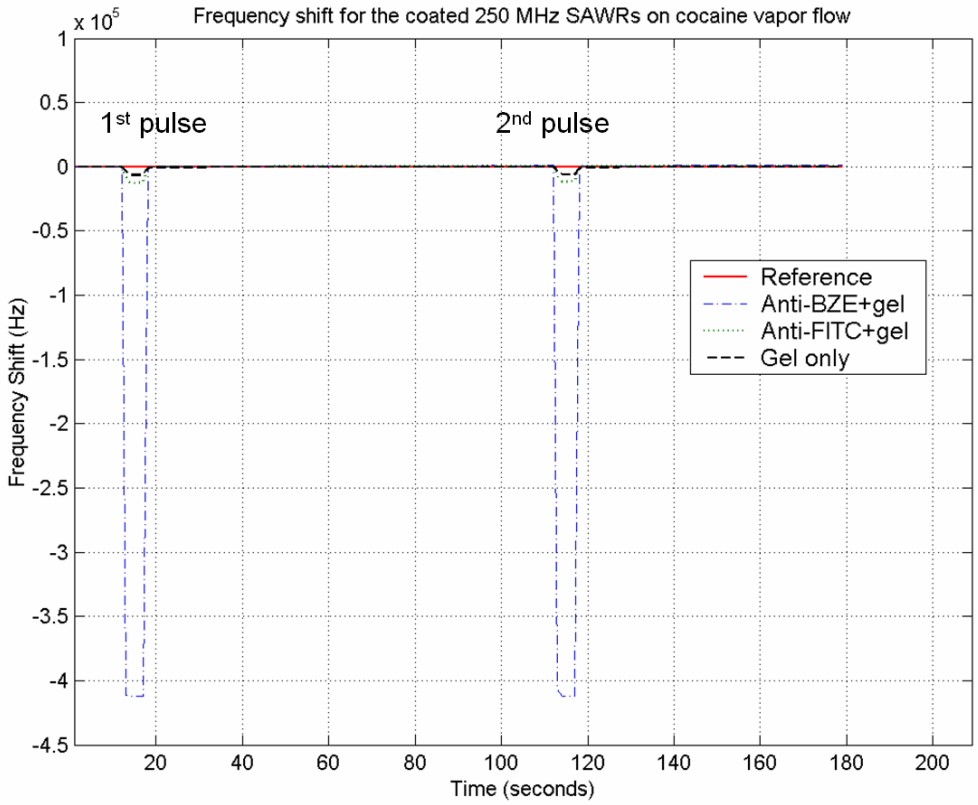

Figure 5-14. SAW immunosensor response when the cocaine vapor is added to the circulating air stream.

In figure 5-14, the anti-BZE device has a far more dramatic instantaneous response than the anti-FITC device does, while there is little or no difference between the gel-only and anti-FITC device responses. Several experiments with the same configuration and devices led to a consistent relationship between the sequence and the amount of frequency shift (Δf) during the pulse cycle on the presentation of cocaine vapor.

Δf (during pulse cycle): Uncoated < Gel only < Anti-FITC/gel << Anti-BZE/gel

This result suggests that during the pulse cycles, the differences in the magnitude of the frequency shift between anti-BZE and other sensors are significant. This fact may be utilized for the establishment of a decision criterion for the real-time cocaine detection.

There are other advantages of the configuration with the constant airflow. It can minimize the non-specific bindings and/or simple attachment of other unwanted molecules or dust on the sensor surface. Thus, it gives the 'right' target more chances and space to bind to the corresponding antibodies but makes even harder for the non-specific antigens or dust to attach on the device surface. This can be conjectured by the dramatic increase (~20 fold) of Δf from the anti-BZE device and about 10 fold decrease from the control devices, compared to the responses in figure 5-13(a). Also, the airflow eliminates the purging step after each sampling and it can prevent possible moisture condensation inside the nozzles, flowcell, and on the device surface. One drawback of this configuration is that the determination of the flow rate is very specific to the sensor system and dimension of the flowcell and nozzle. Also there may be a possible drying effect on the hydrogel layer for a long term use.

5.4.3 Cocaine Detection Part II: Field Test

In the previous experiments, the target was purified cocaine vapor generated from a calibrated dispenser. Also, the experiments were conducted with extreme care under laboratory condition with known data of the sample and the minimal background noise. Herein, such experimental conditions are not maintained to see the sensor's capability to

work in a 'real' world, *i.e.,* the experiments are done under field condition. In collaboration with the Georgia Bureau of Investigation (GBI) chemical analysis scientists, a similar experiment was performed with a seized cocaine sample being processed. The whole sensor system was brought to the GBI Crime Lab in Decatur, GA. The sample was believed to be cocaine free-base, commonly called "crack". Figure 5-15 presents the response of the sensors to a sample drawn from the headspace. Sampling was done twice using the internal pump with a flow rate of 180 ccm at t=20 and t=120.

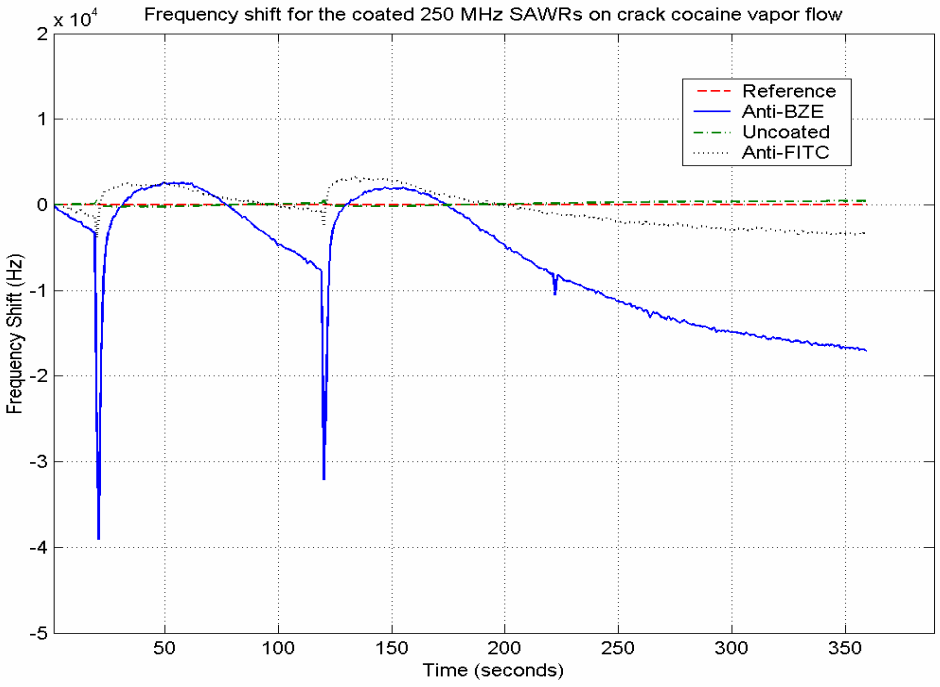

Figure 5-15. Response of the SAW immunosensor array to "crack" cocaine.

The sensor responses shown here and elsewhere in this thesis are the raw frequency shift data from the system without using any smoothing algorithm or post signal processing. In figure 5-15, the signature from the anti-BZE coated sensor consists of a sharp initial transient followed by a baseline shift. The difference in terms of the

response profile between this GBI experiment and the previous experiment using the INEEL vapor generator is attributed to the following reasons. In the case of GBI experiment, the sampling method was different; the sample was "drawn" using a built-in pneumatic pump, rather than "injected" with an external apparatus. Also, the sample is not purified and the concentration of the target is a complete unknown. Considering these experimental conditions and the sampling methodology, the GBI experiment can be considered as a close simulation of a "field" test. As a control, the anti-FITC coated device was used again and exposed to the sample of crack cocaine. There was no such dramatic response from the anti-FITC or uncoated sensors, which is indicative of a successful detection of the target.

5.5 Summary

In chapter 5, a series of actual detection results for the vapor phase acoustic wave immunosensors were demonstrated. The detection experiments were performed using the targets of practical importance such as illicit drugs. They showed evidence of target detection both in the laboratory and field condition. The targets were instantly identified without time-consuming post process or microscope analysis which is a key requirement for practical applications. As is the characteristic of an immunosensor, high specificity was observed for the molecules with similar size or weight. The variation of the vapor delivery setup resulted in a distinct change in the sensor signatures. For example, when the target vapor was injected to the stream of clean air running with a constant flow rate, the target was identified instantaneously during the sampling period and the responses were dramatically amplified. Without the constant air flow, the data assessment was

more easily done by virtue of the baseline shift in the SAW resonator response after the sampling was complete and the system is idle. These findings have implications on how to design the practical devices for rapid detection of a target. As a summary, the experimental results in this chapter proved that if biomolecules or antibodies are utilized for the detection of specific analytes in the vapor phase, a powerful sensor can be developed capable of real-time molecular recognition of airborne analytes of interest.

CHAPTER 6

EFFECT OF LOCALIZED SURFACE PERTURBATIONS ON THE SAW RESONATOR SENSOR

6.1 Motivation and Background

In the SAW vapor phase experiments presented in the previous chapters, the biofilm or the selective layer was coated uniformly on the entire SAW resonator device surface either by spin casting or electrophoretic technique. When performing those experiments, two assumptions are generally made: (1) the receptor molecules or antibodies in the biofilm are uniformly distributed and immobilized on the sensor surface and consequently (2) the perturbation resulted from the occurrences of the antibody-antigen immunoreactions are also uniform over the entire surface.

As the sensing layer and its immobilization process become complex in the modern biosensors, however, it is practically possible that the surface perturbation of a certain location becomes dominant, *i.e.*, the mass loading or perturbation can occur on particular areas of the device surface. This situation happens when the perturbations that arise from the target detection are accidentally concentrated in a specific area and/or the thickness of the sensing film is excessively unbalanced over the surface due to the limitation of current coating methods.

In acoustic wave sensors, the sensitivity or the characteristic of response to the mechanical perturbation is closely related to the acoustic energy distribution. If the energy distribution is not uniform on the device surface, the effect of a surface perturbation will exhibit a positional dependence. In other words, the sensor signature will be a function of location as well as the degree of perturbation. Sauerbrey has shown

that the mass sensitivity of a QCM has a radial dependence from the center of the electrode [7]. A two-port SAW resonator, however, is a fairly sophisticated device that consists of isolated but functionally dependent building blocks such as transducers, reflectors, and a waveguide (or a center grating). Although most of the acoustic energy is contained between the two reflectors, the distribution is non-uniform and thus the spatial dependence is even more complicated. This is highly undesirable especially for the multiple SAW resonator array sensors where the uniformity between sensors is of paramount importance. For example, in the extreme case, one would get a different response from each sensor in the array even if all the sensors have the same detection layer with the same receptor molecules.

One way to resolve this problem is to "force" the perturbation to occur on the same place for all the sensors in array so that the positional dependency can be ruled out for the appraisal and analysis of the signature. This can be realized if the detection layer is partially immobilized only on a specific location. Prior to the immobilization, it is necessary to identify the appropriate immobilization points by investigating the characteristic of the sensor response for different locations of perturbation. Despite its significance, an experimental study of this problem is hard to find in the literature. The only one that the author could find related to this issue was the aerosol experiment conducted by Bowers *et al* [51]. They used an aerosol nozzle to make perturbations on several different spots of a SAW resonator surface. The same amount of aerosol impact was applied to a calibrated QCM to compare the sensitivity by measuring the peak frequency shift. They identified the SAW resonator's positional dependency but the experiments were not performed on the entire area of the device, *e.g.*, their results lacked

data for the reflector region which is one of the significant points of interest. Also, the peak frequency change was the only information from each perturbed location. For this study, it would be better to examine the frequency response over the entire range.

In figure 6-1, the spatial energy distribution on the SAW resonator was predicted based on the standing wave reflection and structural characteristic of the device.

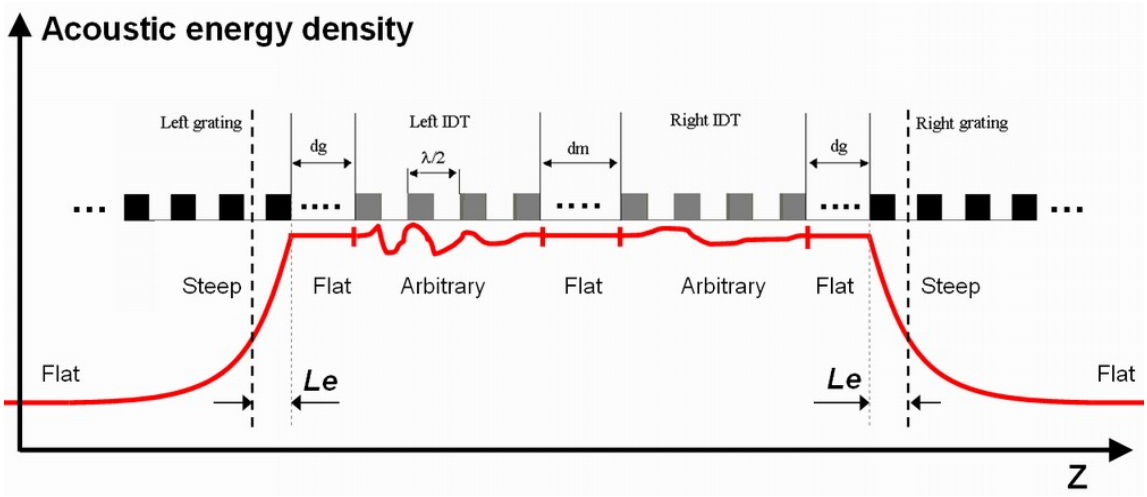

Figure 6-1. Expected acoustic energy distribution on a two-port SAW resonator surface

On the reflector gratings, although the physical reflection occurs at the edge of the first grating element, the standing wave pattern extends beyond the reflector edges. It exponentially decays into the reflector array toward the effective center of reflection L_e which has been defined in chapter 5. It has been also shown in chapter 5 that the L_e is close to the beginning edge of the reflector. Therefore, the acoustic energy exhibits a steep gradient within L_e. The acoustic energy profile on each IDT depends on the apodization pattern. The regions between the two IDTs, between the reflector and IDT, and far outside the effective center of reflection seem to have a relatively flat energy distribution.

When immobilizing a biolayer, it is reasonable to avoid deposition on the structural discontinuities where the energy distribution abruptly changes. For the deposition on separate regions, they need to be done symmetrically from the center. Most importantly, in all cases, the test biolayer should cover the entire width of the acoustic cavity to avoid wave diffractions. By doing this, the straight-crested nature of the wave front is maintained over the entire device surface. Experiments on the region between the IDT and reflector were excluded because the SAW resonators for this study have a minimum possible value of *dg* which is too narrow to immobilize a biofilm.

6.2 Localized Immobilization of Biofilm

The test locations determined based on the discussion in the previous section are on the reflector gratings, on the IDTs, and between the IDTs as shown in figure 6-2. In this study, the same SAW resonator designs utilized for the work done in chapter 5 were used.

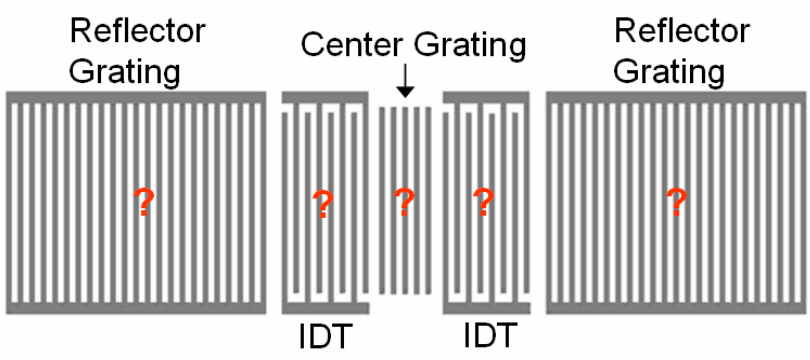

Figuer 6-2. Schematic of a two-port SAW resonator with the test mass-loading locations for this study.

Conducting this experiment requires a tool or equipment that can precisely dispense a small amount of antibodies onto desired locations on the surface of SAW resonators. The BioChip Arrayer™ (BCA) was used to create localized immobilization. As introduced in section 3.2.3, the BCA is a bench top micro dispenser which can dispense minuscule droplets with precision up to 5 micron spacing. In this study, the same type of biolayer used for the vapor phase detection experiment in chapter 5 was immobilized for the purpose of immediate application after the evaluation. The monoclonal antibodies pre-mixed with SPA crosslinker are loaded in the dispenser tip, and then printed on the desired locations. The immobilization of the antibody is achieved by the same principle described in section 3.2.1. This study, however, will focus on the effect of localized mass loading rather than the immobilization process or immunoassay.

6.2.1 Mass Loading Between the IDTs

Using the BCA, a test biolayer was carefully placed between the two IDTs as has been shown in the figure 3-6(b) in chapter 3. Deposition of a selective film on the acoustic wave path between the IDTs is common in SAW delay line based chemical sensors but there is a practical difficulty on SAW resonators due the small gap between the IDTs. It has been discussed that a SAW resonator requires strict requirement of accuracy of the spacing parameters to maintain the standing wave which is essential for the operation of the device. Therefore, it is not a good idea to make large gaps between the SAW resonator elements because the wave velocity used for the calculation of the spacing parameters gaps is technically an approximate value. The consequence of which is that the larger the gaps, the more incorrect the calculated spacing parameters are. Large

gaps also increase the device size. The SAW resonators fabricated herein have a gap d_m~ 126 μm (10 λ) between the two IDTs on which it is possible, with care, to deposit a biolayer without encroaching upon the region of IDTs.

The SAW resonators were also fabricated with and without center gratings. These metal strips, having the same period as the IDTs, provide a homogeneous surface. For a Rayleigh wave, it is reported that the center gratings, termed 'velocity correctors', placed between the IDTs can aid in maintaining a more stable standing wave pattern [52]. Comparing figure 6-3 (a) and (b), the major characteristics (insertion loss, center frequency, signal-to-noise level, etc.) of the both resonators have no significant differences before mass loading. This means that for unloaded two-port SAW resonators, the Rayleigh standing wave is well maintained without the support of the center gratings, provided that the IDTs are precisely placed with an accurate spacing parameter. Once the biolayer is deposited, *i.e.*, the surface is perturbed, the existence of the center grating made a conspicuous difference. Figure 6-3(a) shows that the response after mass loading on the center grating still keeps the sharp resonance peak which ensures high signal-to-noise ratio and reduces the risk of oscillation failure in the sensor array. There is also a distinct frequency shift which tells that the area provides enough sensitivity to detect the target. However, as can be seen in figure 6-3(b), the same amount of mass loading on bare quartz area without the metal grating made marked signal degradation including much higher insertion loss and a deteriorated resonance peak, which obviously will result in a lower Q and a possible oscillation failure in the sensor array. This experiment signifies that for coherent sensor signatures, the homogeneity of the sensing surface is of great importance as well as the uniform energy distribution.

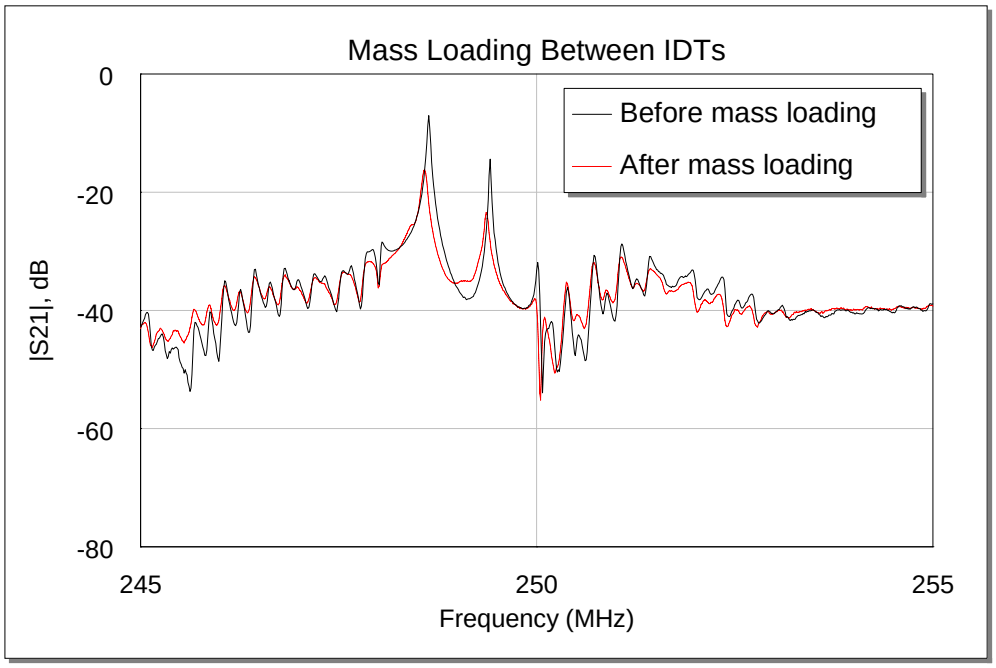

(a)

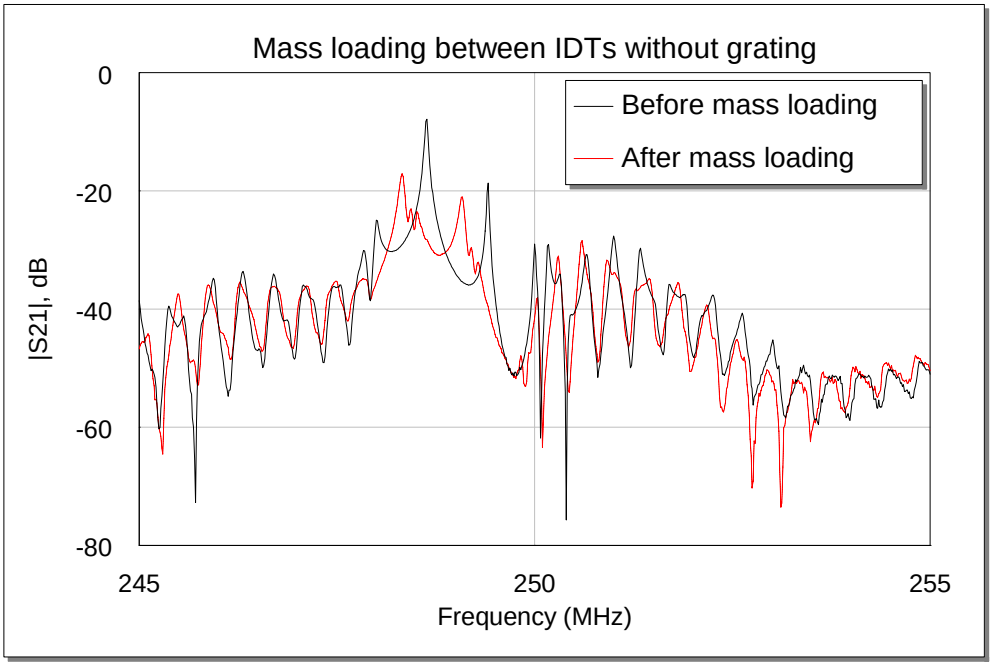

(b)

Figure 6-3. Effect of mass loading between IDTs. (a) SAW resonator with center grating between IDTs. (b) SAW resonator without center grating.

6.2.2 Mass Loading on the IDTs

The same amount of biolayer was deposited symmetrically on both IDTs. As shown in figure 6-4, a large change in the peak frequency accompanied by severe attenuation in the passband region was observed. The resonance peak was barely kept but the signal-to-noise ratio was severely degraded. In terms of the degree of the perturbation effect, the IDT seems to be a more sensitive area than the gap between the IDTs.

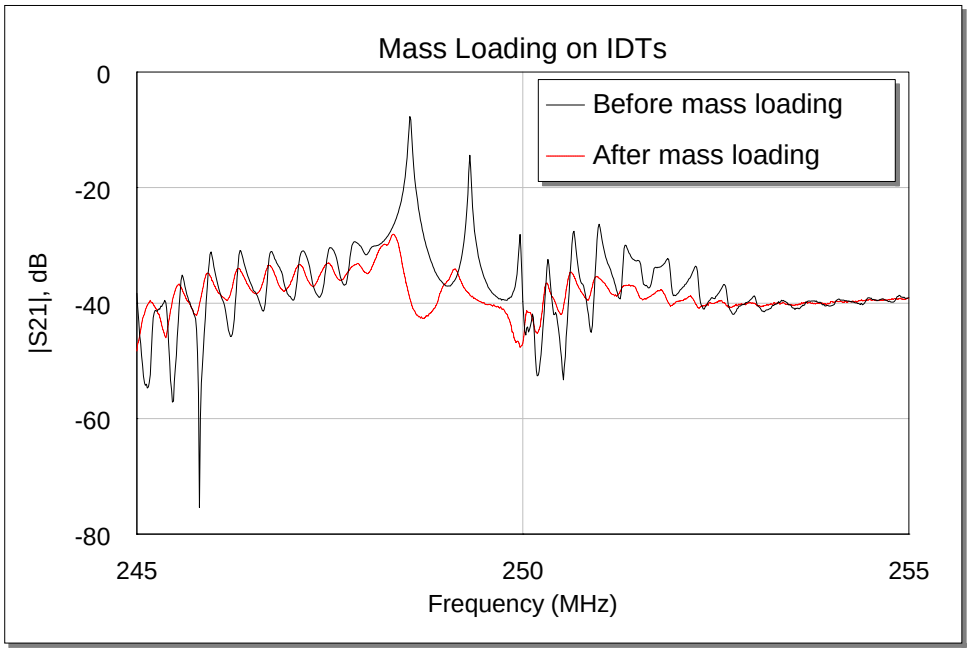

Figure 6-4. Response of two-port SAW resonator with mass loading on IDTs

Although the attenuation problem might be overcome by controlling the amount of deposition, the author asserts that immobilization on the IDTs is not desirable for the following reason. The IDTs are an interface with the external RF signal that drives the resonator and hence an electromechanically active region. The IDTs determine the characteristic of the acoustic wave in the resonator. For example, it has been discussed in

chapter 5 that the variation of the finger overlap of the IDT, termed apodization, directly characterizes the frequency response profile by weighting the electric fields generated by the finger pairs. In that sense, the apodization can be considered as a type of perturbation which is analytic and intentional for the shaping of the signal. However, arbitrary perturbation on the IDTs would result in an unpredictable response or deterioration of the signal. Additional mass loading on IDTs that arises from the capture of analytes, for example, would give rise to the same effect as a random apodization on IDTs.

6.2.3 Mass Loading on the Reflector Gratings

The experiments were done for two different locations on the reflector: inside and far outside of the effective center of reflection as shown in figure 6-5.

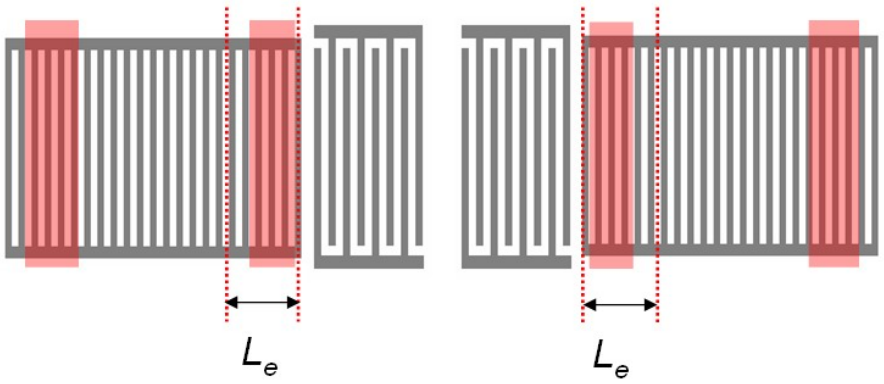

Figure 6-5. Mass loading on the SAW reflectors. Experiment was done for both inside and far outside of the effective center of reflection (L_e).

In the acoustic energy profile in figure 6-1, a significant amount of energy exists near the leading edge of the reflector. This is also the location where the gradient of the acoustic energy profile is the steepest. Figure 6-6 presents the frequency response of the

resonator when the test biolayer was immobilized inside of the effective center of reflection (L_e) on the reflector. This location was more susceptible to the perturbation than any other area. The same amount of mass loading in this narrow area caused total degradation of signal over the entire measured frequency range. The resonance peak is completely destroyed and there exists severe attenuation which obviously will result in an oscillation failure in the sensor array. This is because the Bragg condition and the spacing parameters required for the induction of constructive interference are no longer valid and consequently the standing wave is not maintained. In a word, the reflector has lost its functionality.

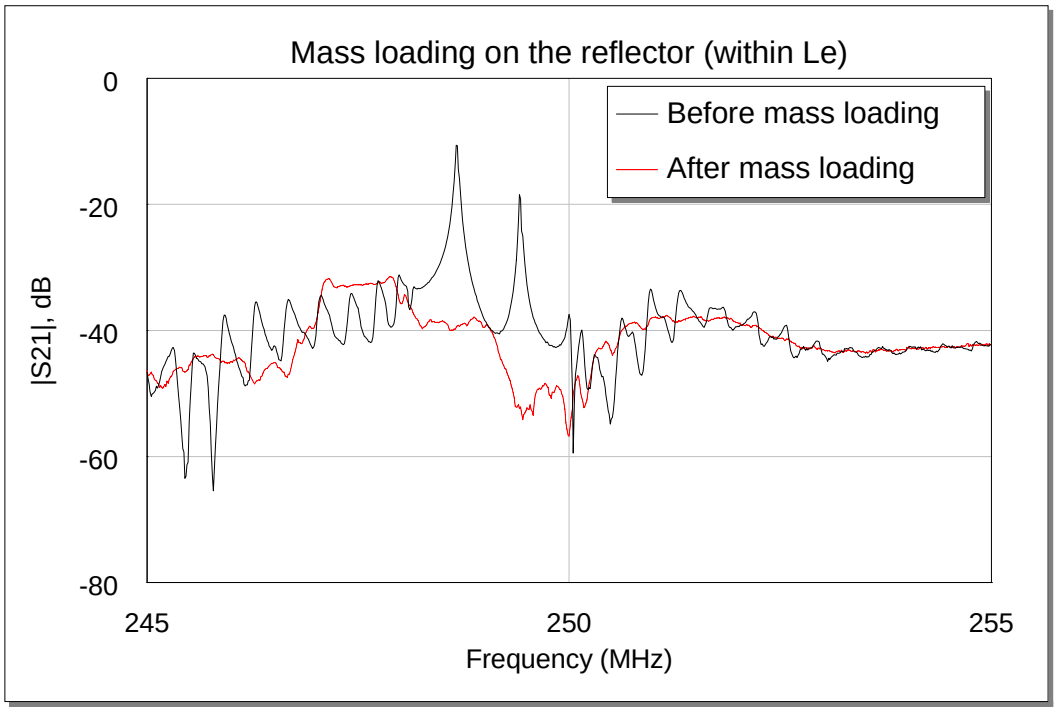

Figure 6-6. Response of two-port SAW resonator with mass loading on the reflectors within the effective center of reflection (L_e).

The other test location on the reflector is far outside of the effective center of reflection. In this area, the energy distribution is relatively flat but as shown in figure 6-1, the level of the acoustic energy is very low. As expected, the difference after the deposition of biofilm was too small to be identified. Such a low energy concentration results in low sensitivity and poor detection limit.

6.3 Summary and Conclusion

In this chapter, a novel method was used to empirically investigate the dependence of SAW resonator signature on specific perturbation spots. Mass-loadings were applied on several significant locations on two-port SAW resonators using the BioChip Arrayer. Frequency characteristics were measured for each SAW resonator sample with a different deposition location for the receptor molecules which represent an acoustic perturbation to the SAW resonator cavity. It was observed that the sensor signature is strongly dependent on the location of these perturbations as well as the concentration of the receptor molecules. The degree of impact seemed to be closely related to the non-uniform acoustic energy distribution on the SAW resonator surface. The results of this study would give insight into how to strategically create the detection layer for the modern SAW resonator sensors by locating the areas where the sensing layer should or should not be deposited.

Significant signal degradation was observed when the biofilm was coated where the energy distribution has a steep gradient or spans over the structural discontinuities. The author found out that the best place for the selective layer deposition was between the two IDTs with a shorted center grating structure employed. There have been no clear

rules for the location of detection layer on the SAW resonator sensors and also very little published data on the positional dependency of SAW resonators currently exists. Therefore, these experimental results should prove to be valuable in the development of a detection layer coating protocol to minimize signal failures and enhance the sensor performance for SAW resonator array biochemical sensors.

CHAPTER 7

SEMI-ORTHOGONAL SIGNAL STATE-SPACE MAPPING

From the previous chapters, it is shown that frequency-offset immunosensors based on acoustic wave devices provide high sensitivity and selectivity where the target is detected and identified based on the amount of frequency shift. For the final topic of the thesis, a novel method [53] to further classify chemically similar molecules is presented, which extrapolates on the concept of in-phase (I) and quadrature-phase (Q) domain used for the detection of orthogonal M-ary signals in digital telecommunication systems. Experiments were performed using samples of explosives such as RDX and TNT containing nitrous oxide groups, and chemically analogous substances. This detection scheme involves semi-orthogonal monoclonal anti-TNT and anti-RDX antibodies immobilized on two sensor surfaces. After the measured frequency data are remapped onto a new I-Q domain, all the substances were detected and mapped out to distinct regions. This result indicates a strong similarity between digital radio system quadrature detection techniques and the I-Q mapping scheme of the immunosensor signatures.

7.1 Introduction

One of author's previous publications [3] demonstrated the ability to detect and differentiate among analogous molecules using an acoustic immunoassay vapor sensor termed "dog-on-a-chip". Practically, this analytical tool was limited by the availability of an antibody toward a specific target molecule. However, this issue can be addressed

by exploiting the intrinsic promiscuity common to all antibodies. Behring, a physicist who won the Nobel Prize in 1901, and Kitasato, his long time colleague, first introduced the theory of antibody-antigen binding specificity [54]. Later that century another Nobel laureate, Karl Landsteiner published the structure and mechanisms involved in antibody-antigen interactions. These works formed the canon of antibody-antigen reactions, which can be succinctly expressed as the precise fit model. This model has been subsequently revised following innovative work by Cameron and Erlanger who introduced the cross reactivity phenomenon between antibodies, antigens and their structural homologues [55]. The mechanism is said to be comprised of both electrostatic and hydrophobic interactions due the large number of hydrophobic residues in the antigen binding site. In addition, some promiscuous antibodies can cross-react through hydrogen bonding with antigens that are not structural homologues of the target antigen. James and Tawfik concluded that the promiscuous nature of antibodies suggests that each protein may have its own unique pattern of multispecificity and each activity stands alone and may be highly specific [56]. This pattern of promiscuous activity is identified as a molecular signature that is unique and quantifiable. Herein, the author presents evidence of multispecificity in an anti-TNT clone when exposed to vapors of 2,4,6-trinitrotoluene (TNT) and hexahydro-1,3,5-trinitro-1,3,5-triazine (RDX: Royal Demolition Explosives) by introducing a novel method for the treatment and visualization of the data using digital telecommunication theory to unveil the real-time dynamics of antibody/antigen interactions.

7.2 Semi-Orthogonal Biosensor System

A biosensor detection system is constructed from two channels with each channel consisting of a separate semi-orthogonal SAW immunosensor shown previously in chapter 5. This semi-orthogonal biosensor detection system is illustrated in Figure 7-1a where the X channel output is from oscillator X implementing the SAW immunosensor coated with biolayer X and the Y channel output is from oscillator Y implementing the SAW immunosensor coated with biolayer Y.

There also exists a multi-dimensional communication system that implements orthogonal frequency domain modulation (OFDM). Here, the digital data is split amongst a multitude of narrowband channels such that the data in channel (n) is "orthogonal" to the data in channel (n+k), where (k) is a number greater than 1. The greater the (k) value, the more orthogonal the data in each channel will be with respect to each other and hence can be described as interacting less with each other. Hence, the biosensor system can be extended to a general n^{th} dimensional system as shown in figure 7-2(b). Here, the degree of chemical similarity between analytes of individual channels decreases as (k) increases.

Just as each narrowband channel of the OFDM system would have a defined bandwidth and the difference between adjacent channels would define adjacent channel interference, the multi-dimensional biosensor system also has similar traits. The affinity of each channel's biolayer (bandwidth) can be defined along with the degree of multispecificity between the adjacent channel antibodies (interference). The grouping of any two biosensor channels would produce a 2-dimensional map and the grouping of any three biosensor channels would produce a 3-dimensional map. The system can then be designed such that there is a minimal amount of cross-reactivity between channels.

Although a direct visualization of data beyond 3-channel sensor system is not possible, the characteristics and correlation between the target molecules can be determined by analyzing the numerical data obtained from each channel of the sensor system.

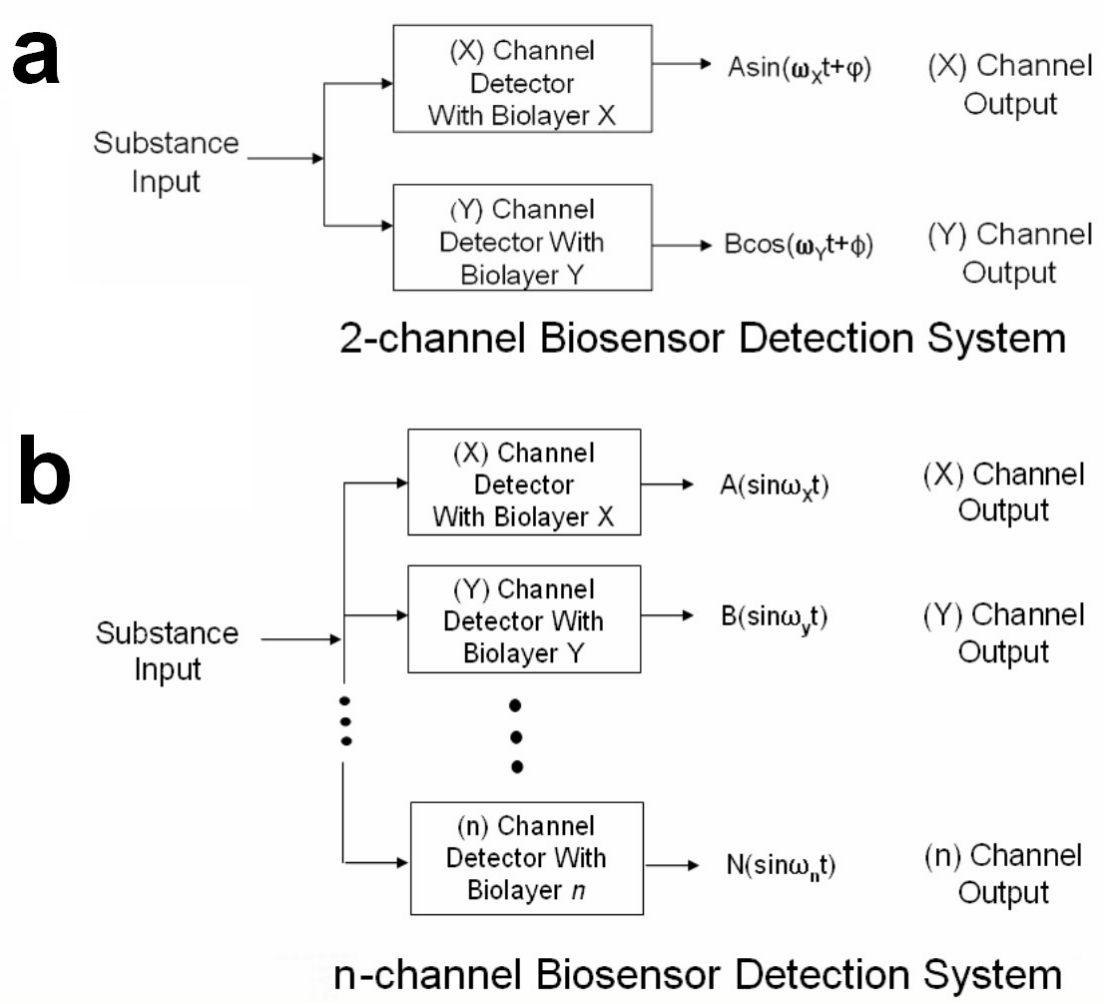

Figure 7-1. Semi-orthogonal biosensor detection system. (**a**) Schematic of 2-channel biosensor system. (**b**) N-channel biosensor system. The two-channel system can be expanded to a general n-channel biosensor system by introducing additional semi-orthogonal channels.

7.3 Analogy to the Digital Telecommunication Systems

There is a strong similarity between the detection techniques of a quadrature digital communication system and that of the semi-orthogonal biosensor system. Figure 7-2a shows the constellation plot of 8-ary QAM (quadrature amplitude modulation) system. The first two bits of the tribit binary data define the phase position and the least significant bit (LSB) defines the amplitude position. For a QAM signal, the binary data is combined into two separate carriers, *i.e.*, two channels, each having the same frequency but mathematically orthogonal in phase with respect to one another. At the radio receiver, the received signal is separated based on its orthogonal phase information into two separate orthogonal channels. The binary data is then characterized from each channel and mapped according to the phase and modulation information. Likewise, one can construct a state-space map from the immunosensor system to characterize and map the target analytes. Just as the binary data defines its position on the constellation plot, the analyte data also defines its position on the state-space map by the degree of affinity between each analyte and the system antibodies. Figure 7-2b represents an example signal state-space map for a two-channel biosensor system. The separation among clusters reflects the degree of chemical similarity between analytes. The magnitude of a cluster is dependent on the analyte characteristics such as concentration and/or vapor pressure. On the signal state-space map in figure 7-2b, sample **A** is specific to the anti-Y antibody, thus can be considered as the substance Y, but also has a little affinity to anti-X antibody. Samples **B** and **C** are virtually the same substances with different concentrations. Sample **D** can be considered as the substance X, and **E** has a very similar chemical structure to **D** but has different concentration or vapor pressure. Sample **F** is in

totally different category and not an analogue of X or Y. This analysis scheme greatly reduces the mathematical complexity which is required for most chemometric methodologies. The analogies between the interaction of the antibody/antigen binding event and the detection techniques of a quadrature digital radio receiver system are summarized in **Table 7-1**.

The domain conversion algorithm from a time-frequency domain to a semi-orthogonal state-space map is described in Figure 7-2c. Each separate time-frequency characteristic of the X and Y oscillators are mapped onto a single quadrature frequency domain, with both axes having the units of Hz. First, in the time-frequency domain, the amount of the frequency shift (Δf) from each channel is calculated in real-time by subtracting the frequency of the reference sensor from the absolute frequency value of each channel. The frequency shift at each sampling point on the time axis becomes a coordinate of the new domain. For example, the sampling points 1 through 4 in the time-frequency domain in Figure 7-2c are mapped to (x1, y1) through (x4, y4) in the quadrature phase domain. The sampling points of the time-frequency domain can be strategically controlled depending on the system parameters such as the time duration of the analyte injection.

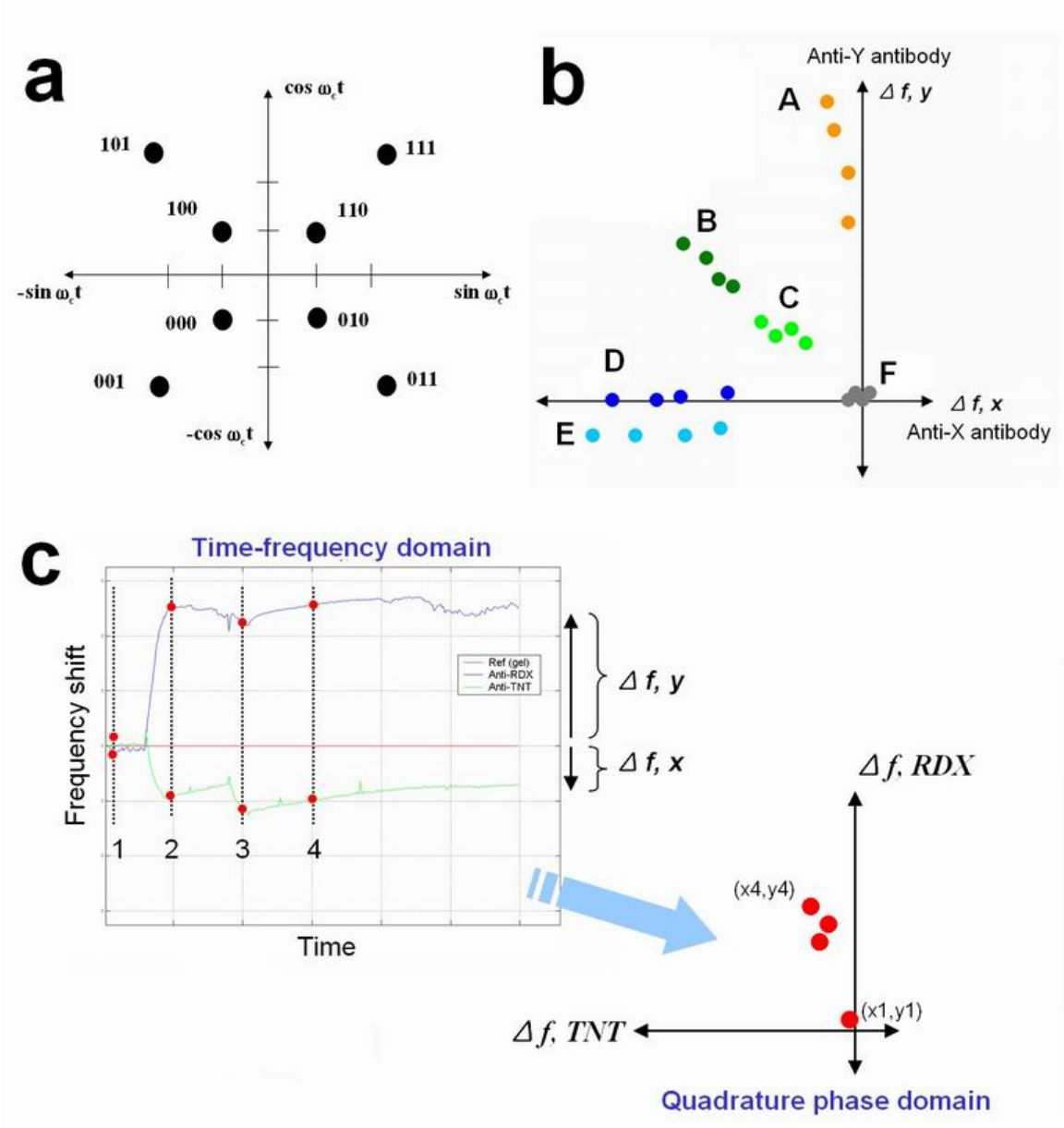

Figure 7-2. Analogy between digital telecommunication systems and semi-orthogonal immunosensing schematic. (**a**) 8-ary QAM constellation diagram. (**b**) Example of two channel immunosensor signal state-space map. (**c**) Conversion from the time-frequency domain to the quadrature phase domain.

Table 7-1. Comparison table between digital radio systems and semi-orthogonal state-space immunosensing.

Parameters of interest	**Digital Radio Systems**	**Semi-orthogonal state-space immunosensing**
Map	Group showing the relationship between binary data and the signals magnitude and phase	Group showing the relationship between analyte data and the signals frequency
Axes of the map	Two orthogonal signal channels with embedded phase and magnitude information dependent on binary data	Two orthogonal or semi-orthogonal signal channels with embedded frequency information dependent on analyte data
Separation between data clusters within the map	Degree of similarity between the binary coded signals	Degree of chemical similarity between analytes
Magnitude of data clusters within the map	Dependent upon binary data characteristics such as bit value	Dependent upon analyte characteristics such as concentration and/or vapor pressure
System selectivity	Dependent of front-end and baseband filtering to reject close-in signals	Dependent on the antibodies inherent ability to distinguish antigenic differences to reject similar analytes
System sensitivity	Ability of the system to respond to weak RF signals (measured in microvolts)	Ability of the system to respond to low concentrations (measured in parts per billion)
Channel interference	Semi-orthogonality of pairwise signals and/or cross channel rejection characteristics	Immunoglobulin multispecificity of antibodies to analytes
System link budget	Receiver's energy per bit to the noise power spectral density ratio, E_b/N_o, dependent on data rate, transmit power, and path loss	Sensor's bound antigen concentration (*b*) to total antibody concentration (*a*) ratio per concentration of total antigen (*c*) ratio, *b/ac* (Scatchard equation), dependent on analyte concentration, vapor pressure and path loss

7.4 Experiments

A biosensor detection system was constructed from two channels with each channel consisting of a separate semi-orthogonal SAW immunosensor. The devices are housed in a sealed flow cell, and then connected into an oscillator circuit, and the frequency changes of both channel outputs can be precisely measured in real time. For the sampling of the target, the experimental setup included a pneumatic apparatus that drew vapor from the various substances into the biosensor system. Figure 7-3 illustrates a diagram of actual two-channel sensor system setup in Figure 7-1a. In this experiment, the X channel detector implemented the anti-TNT antibody layer and the Y channel detector implemented the anti-RDX antibody layer. The antibodies are immobilized using the protocol described in section 3.2.2

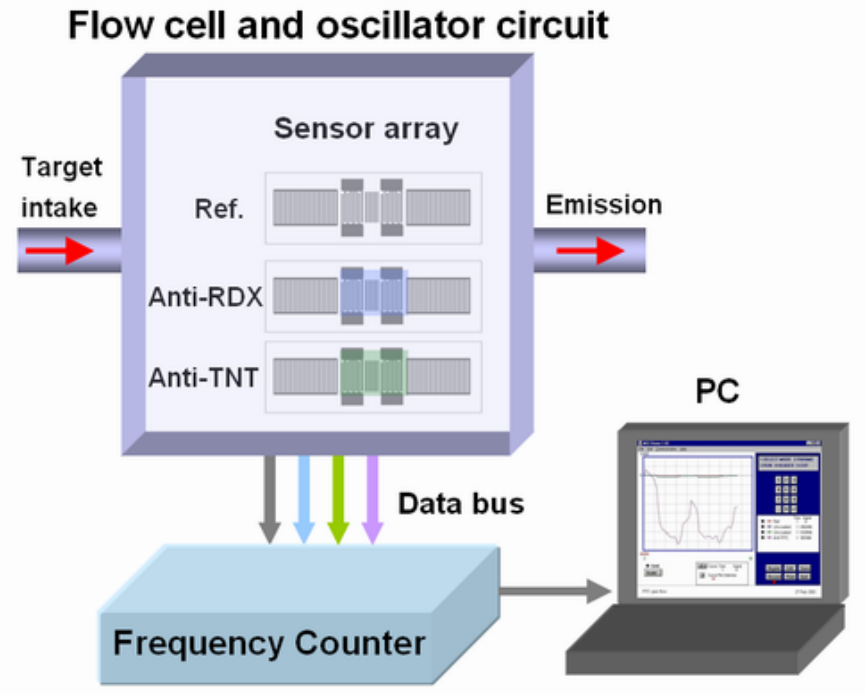

Figure 7-3. Two channel SAW immunosensor system setup

To minimize possible spurious responses arise from the undesirable perturbation such as air pressure or temperature changes, a non-specific reference sensor is employed and subjected to the exactly same physical environment as the detecting sensors. This configuration enables us to exclude unnecessary signals that are not related to the target detection, and thus to perceive a real signature of the detection. Actually, the frequency data from the reference sensor are subtracted from each detecting sensor's response.

7.4.1 Two-Channel Biosensor System: TNT Analogous Chemicals

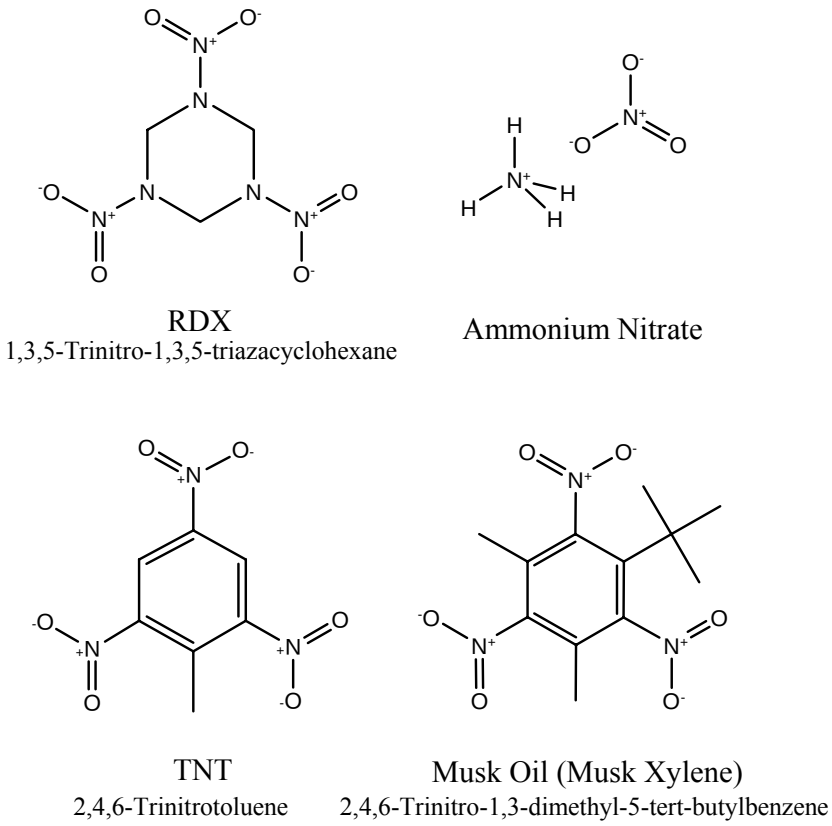

Figure 7-4. Explosive substances and analogues used for the experiments

Figure 7-4 shows the explosive substances and the analogues that were presented to the two-channel biosensor system. Zeck *et al.* reported higher binding affinities among the TNT analogs with nitro-groups on the ring suggesting an electrostatic binding mechanism maybe the key to its molecular specificity [57]. The substances in this case are related via an NO_2 branch. Our experiments have shown that these substances, TNT, RDX, Musk Oil or Musk Xylene, and ammonium nitrate all bind differently with respect to anti-TNT antibodies and anti-RDX antibodies. Both the mouse anti-TNT clone (lot #107415) and the mouse anti-RDX (lot #200202-3-4) were obtained from Strategic Biosolutions. This lot of anti-TNT was reported to cross-react to other TNT analogs [57, 58, 59].

The targets were presented to the flow cell by using the vapor generators, or by direct sampling the headspace of an immobilized target using a built-in pneumatic pump in the sensor system. The TNT vapor was introduced using the INEEL vapor generator, with a flow rate of 150 cc/min at 13.2 ^{o}C, and released 50 pg of TNT per pulse with duration of 0.3 seconds. The RDX vapor was introduced using the same type of generator, with a flow rate of 150 cc/min at 53 ^{o}C, and released 50.3 pg of RDX per pulse with duration of 3.2 seconds. The C4 data was obtained in an open lab with an unheated 5 micron filtered sampling head positioned 2.0 inches from the material at the bottom of a sample bottle. The Musk Oil data was similarly recorded with the filtered sampling head positioned 3.5 inches from the sample. The ammonium nitrate data was derived at the same distance. In the case the sensor uses its built-in pneumatic pump, sampling was done at 30 sec and 90 sec with 15 seconds of pulse width and a flow rate of 180 cc/min.

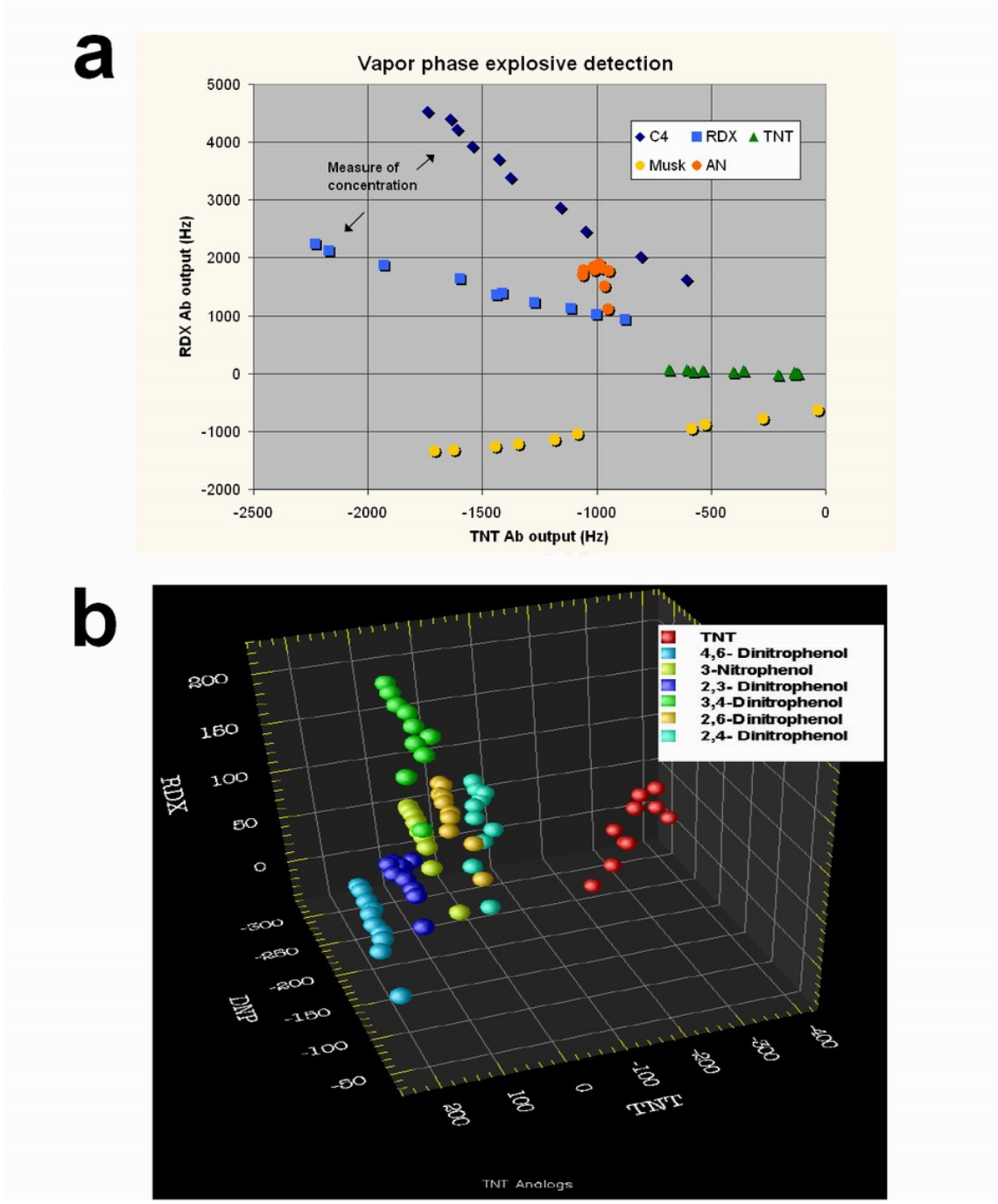

Figure 7-5. (a) A two-dimensional signal state-space map of the samples generated from the signature of two channel biosensor system. (b) A three-dimensional signal state-space map generated from the signature of three channel semi-orthogonal immunosensors system.

After sampling of the frequency offset data from each substance and applying the domain conversion, a signal-state map was constructed. The signal state-space map of Figure 7-5a illustrates the grouping or clustering of substance data. It is clearly shown that each substance is distinctively mapped onto a region of the signal state-space map.

7.4.2 Three-Channel Biosensor System: DNP Analogues

As discussed in section 7.2, the dimension of the signal state-space can be expanded by introducing additional semi-orthogonal channels. As an example, we show a 3-dimensional cluster map which was produced from three semi-orthogonal immunosensor channels. The sensor system setup and the domain conversion schematics remain the same, but an additional sensor coated with anti-dinitrophenol (anti-DNP) antibody was employed to the sensor array. Each individual sensor was coated with anti-TNT, anti-RDX, and anti-DNP antibodies respectively. For this experiment, soil samples containing TNT and several nitrophenol analogues obtained through the EPA (Environmental Protection Agency) were examined as a target. The result is a three dimensional map as shown in figure 7-5(b), defining the characteristic signature of each of the chemical analogs.

7.5 Conclusion

In summary, the observed multispecificity of anti-TNT and anti-RDX towards nitro (NO_2) groups of molecules was presented. The immunoglobulin multispecificity, termed promiscuity, is common occurrence in biological systems. The ability to cross react with multiple antigens is believed to be due to the conformational diversity

("conformation isomerism") among antibody clones [60]. The polyspecific nature of antibodies has been linked to the occurrence of high background noise during an immunoassay termed interference and is closely correlated to its binding affinity. As an analytical tool, the concept of semi-orthogonal signaling used in digital radio systems is extended into the detection process of immunosensors. At least two immunosensors are used such that the channel X antibody and channel Y antibody displays certain promiscuity to chemically similar molecules. The degree of affinity of each channel is then mapped onto a signal state space map to exhibit distinct regions of chemically analogous substances. While conventional methodologies focus on the specificity of a single antibody to bind with and identify a certain substance, this new concept allows for cross reactivity between substances and antibodies to assist in the identification and classification of analogous chemicals with minimal computational effort.

CHAPTER 8

CONCLUSIONS

8.1 Summary of the Thesis Work

The object of this thesis research was to facilitate the appraisal and analysis of the signatures of the modern acoustic wave biosensors, as well as to improve the experimental methodology to enhance sensor performance. As a theoretical approach, extended relationships beyond the classic mass loading theory were derived. They were able to account for some abnormal signatures that could not be explained by the classic theories and also verified that dynamic information related to molecular recognition events between antibody and antigen can be extracted from the time-dependent sensor signature.

In chapter 3, some of the commonly used biolayer immobilization protocols were introduced and their functionality was corroborated by fluorescent immunoassay and microscopic analysis. Especially, the viability study of the electrophoretic immobilization of antibodies on the hydrogel PPF (plasma polymerized thin film) coated surface is hardly found in the literature. In the following chapters, a series of actual detection experiment results for the vapor and liquid phase acoustic wave immunosensors were demonstrated. These results were from numerous experiments using the targets of practical importance such as narcotics, bacterial spores, and explosives. They showed evidence of target detection both under laboratory and field condition. The author believes that the vapor phase detection of small molecules using the antibody coated SAW immunosensor is one of the pioneering works in this field. In addition, the

characteristics of the SAW resonator sensor signatures depending on specific mass loading locations were empirically investigated, which suggested several implications for a creation of biolayer on the SAW resonator sensors. Finally, a novel method to classify and visualize chemically analogous substances was introduced to aid in the practical use. This approach goes beyond the conventional detection schematics that simply detect the existence of the target; it also provides information about how the targets are chemically close to each other based on the multispecificity of antibodies.

As a summary, the author expects that the thesis work herein may contribute to the study of the modern acoustic wave biosensors which includes but is not limited to: the establishment of underpinning theory that will aid in the evaluation of the signatures; the practical aspects of design and fabrication of SAW devices specific to the vapor phase immunoassay; the development of efficient experimental methodologies; the strategic immobilization of a biolayer on SAW resonator based biosensors; and, the acquisition of reference data for the development of commercial acoustic wave sensors.

8.2 Future Work

One of the most demanding and imminent subjects of the work that can be extended to this thesis is the development of a viable purging protocol for the reuse of the immunosensors. The major challenge with this technology is associated with the effective dissociation of the antigen-antibody bound or antibody-crosslinker complex. The former is more time and cost-effective because it eliminates the additional antibody immobilization process and the current antibodies can be reused. The theory of the binding mechanism is well known, but practically the antigen-antibody complexes are not

easily dissociated. This makes the reusable immunosensor development very difficult. It is reported that the antibody-SPA complex can be dissociated by a Glycine-HCl buffer solution (0.1 M, pH=3.0), but requires that the SPA and antibody are not cross linked to each other [61]. The dissociation of antigen from antibody has been reported by Davis and Leary [24]. According to their experimental results, decreasing the pH to 3 released the bound IgG but not the SPA. However, further reports on the antigen purging techniques for the practical reuse of immunosensors are rarely found. Therefore, significant research needs to be conducted in order to make advancements in this area. Once this technology is developed, the next task will be the miniaturization of the sensor system to lead toward a small, low-cost handheld unit capable of real-time detection of a variety of targets.

APPENDIX A

Two-Port 250 MHz SAW Resonator Fabrication Steps for the Vapor Phase Detection Experiments

The procedure below describes the processing steps the author used to fabricate, package, and probe-test the two-port SAW resonators on quartz substrates. A major part of the recipe and measuring procedures has been developed from the author's experiences, and consequently it is very specific to the author's thesis research. Although the recipe introduced herein might be a reference for other photolithography process of devices with the similar minimum feature sizes (*e.g.*, ~1-5 um), it may not be a standard procedure for the SAW resonator fabrications and measurement. The general SAW device fabrication procedure is shown in figure A-1.

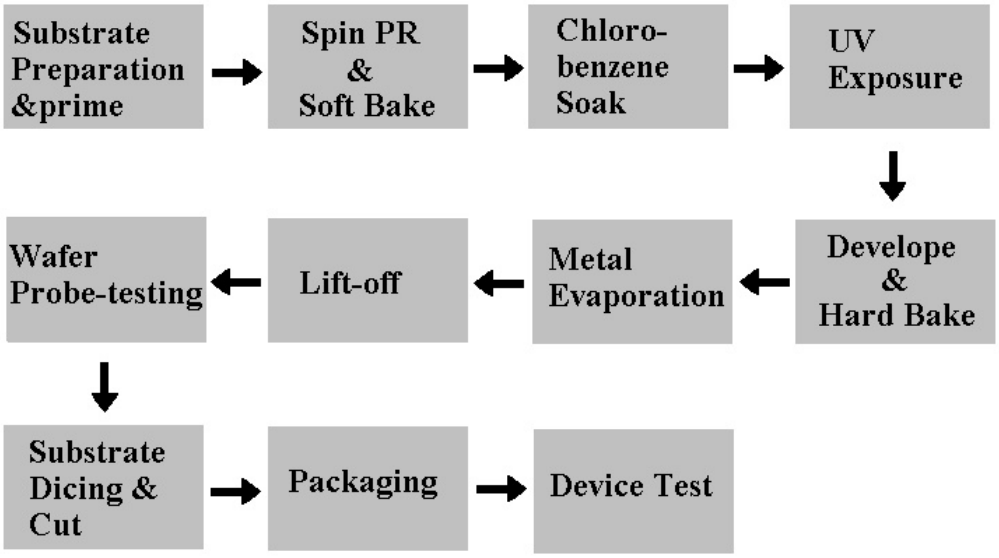

Figure A-1. General photolithography procedure for a SAW device fabrication.

1. Prepare 0.5 mm-thick, 3-inch ST-cut quartz wafers with single-side polished, seed free.

   NOTE: The double-side polished quartz wafers are also commercially available (usually more expensive), but the reason for the choice of a single-side polished wafer is that the unpolished side can efficiently scatter out the coherently generated fast bulk modes on the back side. If the back side were also mirror-like, the bulk modes would bounce back to the output IDT which results in spurious peaks and noise above the center frequency region.

2. Rinse the wafer with the following sequence. TCE (Trichloroethylene) - Acetone - Methanol - Isoprophanol - DI water. A TCE washing can be skipped if the wafers do not have excessive oily contamination, *e.g.* fingerprints or wax.

3. Completely dry using a nitrogen gun and, if necessary, put it in the oven or on a hotplate.

4. Pour HMDS (hexamethyldisilazane) in a Pyrex bowl about 1 cm depth and lay two small beakers on side (or any thing on which the wafer can be laid stably) inside the bowl and heat on the hotplate and close the lid. When the HMDS boils, carefully place the wafer "facing up" on the two beakers and close the lid. After 1 minute, get the wafer out and cool it down.

   Caution: The wafer surface should be exposed to the HMDS "vapor" only. Do not let the HMDS liquid droplets splash on the wafer surface.

5. Spin the PR (Shipley S1805) on the wafer at 4000 rpm (with the maximum acceleration) for 30 seconds. This will make the PR thickness about 0.5-0.7 μm. The PR thickness should be smaller than the minimum feature size of the device.

6. Softbake the PR coated wafer on a hotplate at 130°C for 60 seconds.

7. Mount the wafer on the mask aligner and expose the UV light (365 nm, 8 mW) through the mask for 8 seconds. Adjust the exposure time according to the UV power.

   NOTE: To excite a Rayleigh wave, the reference flat must be perpendicular to the wave propagating direction. (See figure 2-7 in chapter 2)

8. Soak the wafer in the chlorobenzene for 1 min 30 sec. This surface modification process will harden the upper PR layer so that the top surface of the photoresist can be developed at a slower rate than the underlying resist. More technically, the chlorobenzene diffuses into the photoresist causing it to swell. A gel is formed to the depth of the diffusion, which has a slower development rate than the rest of the resist. The purpose of this process is to make a reentrant (a.k.a. undercut) profile. This reentrant profile makes the lift-off easier and also reduces the effects of overdevelopment by keeping the PR aperture size unchanged.

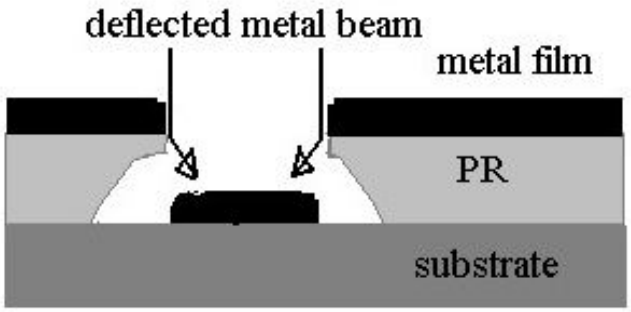

Figure A-2. Diagram of reentrant (or undercut) profile after the chlorobenzene treatment.

9. Completely dry out the chlorobenzene with a nitrogen gun. WARNING: Do not rinse out the chlorobenzene with DI water or any other chemicals.

   NOTE: Technically, the step 7 and (8+9) can be swapped. But the sequence above is preferred because it provides enough time for the wafer to be cooled down before it is soaked in the chlorobenzene. The author found that soaking the hot wafer in the chlorobenzene spoiled the PR surface with unknown residues.

10. Prepare 5:1 Microposit MF351 developer solution (5 volumes of DI water : 1 volume of MF351 concentrate) in the Petri dish and put the wafer in the developer solution and slowly agitate. In 12-15 seconds, the red dye in the PR begins to burst out. Keep agitating. At 20 seconds, immediately get the Petri dish to the running DI water and rinse the wafer surface for 30 seconds. For efficiency, turn on the DI water before the develop process begins.

11. Completely dry the wafer with a nitrogen gun.

12. Hard bake the wafer at 130°C for 30 seconds to remove any solvent and water.

    NOTE: The hard bake sometimes complicates the lift-off result. It can be omitted if the wafer indeed is completely dried.

13. Load the wafer in the e-beam evaporator. Pump down until the chamber pressure reads below $1x10^{-6}$ torr. Deposit 300Å of Cr, then 1200Å of Al, making 1500Å of total thickness.

    NOTE: The metal film thickness (h) is of course dependent on the wavelength (λ), acoustic modes, and choice of the metal. For Rayleigh devices on quartz, h/λ=1-2 % is acceptable. For STW or other SH devices, an exact calculation is required as the dependency of the SH waves on the film thickness is higher than the Rayleigh SAW. Refer to references to find a correct film thickness.

14. Prepare acetone in a petri dish. Take the wafer out from the evaporator and soak in the acetone. The unwanted Al film will be lifted-off within 10 minutes.

15. If the unwanted Al film does not completely come off after 10 minutes, soak the wafer in the acetone and use the ultrasonic bath for about 20 seconds. (The timing depends on the power of the ultrasound bath.) An excessive use of the ultrasound bath will damage the entire film on the devices.)

16. To prevent a re-deposition of the Al flakes to the wafer surface, rinse the wafer immediately after the lift-off process using the procedure in step 2. Completely dry using a nitrogen gun.
17. Perform a full two-port calibration of HP 8753C network analyzer with 250 MHz center frequency, 40 MHz span, and 801 or 1601 number of points using two wide-pitch (1200-1250 μm) probe tips (Use two Cascade ACP1250 GS).

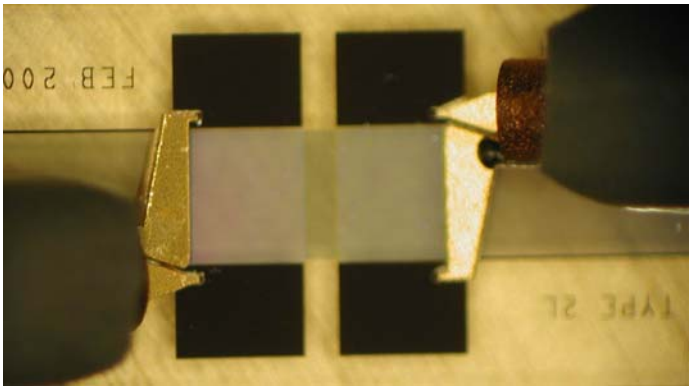

Figure A-3. Wafer probe test of 250 MHz two-port SAW resonators on a quartz wafer.

NOTE: In order to conform to the configuration of the SAWPRO-250 oscillator circuit, the ground (G) and signal (S) of each port are facing diagonally, as shown in figure A-3. In this case, make sure G connects to G, and S connects to S when doing the THRU calibration. To do this, use a calibration substrate that can support this configuration. When using the SG and GS probes and a regular calibration kit, the 180° phase difference at the output should be considered.

18. Measure the S_{21} parameter in a log-magnitude mode. A typical response of a SAW resonator is shown in figure A-4. The peak frequency is supposed to be between 249.5 MHz and 250 MHz. The absolute value of the y-axis at the peak should be around 13 dB or less (*i.e.* the insertion loss (IL) should 13 dB or less). If the IL is greater than 18 dB, it will hardly oscillate in the SAWPRO sensor system.

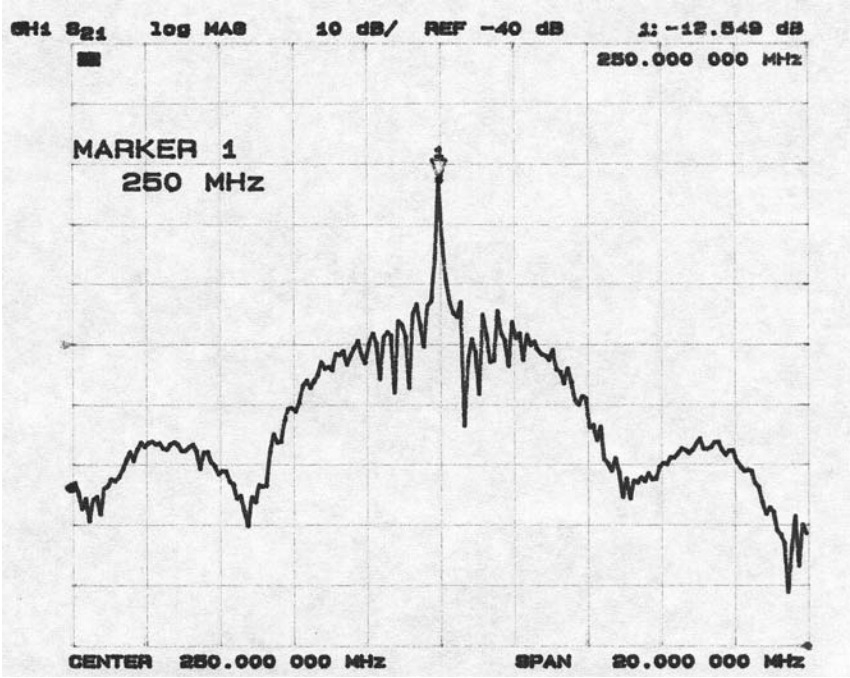

Figure A-4. Measured frequency response $|S_{21}|$ of a 250 MHz two-port SAW resonator.

19. Dice the wafer into individual chips using the MAI-1006 dicing saw. For quartz wafers, use a 6-10 mil-thick diamond coated resin blade rotating at 30,000 rpm with 4 mm/sec of feeding speed. (Details on the dicing technique are available on the blade manufacturer's websites)

20. Deposit a hydrogel/Ab layer on the device surface (using the protocol introduced in chapter 3)

21. Mount the coated chip on a 3-pin 1-ground TO-8 package using adhesives.
    NOTE: A small amount (1-5 μl) of PR can be used as a good adhesive, but in our specific case for immunosensors, nontoxic school glue is a better choice because the organic solvent in PR can denature the immobilized antibodies and thus damage the biolayer.

22. Using a Westbond 7400 series manual wirebonder, wirebond the SAW chip to the TO-8 package using a 1-mil Al wire as in figure A-5.

NOTE: The wirebonding herein is not common; the wire will go through the hydrogel/Ab layer. Adjust the ultrasonic power and time of the wirebonder until a stable bonding is achieved. It may take considerable time to find out the right parameters.

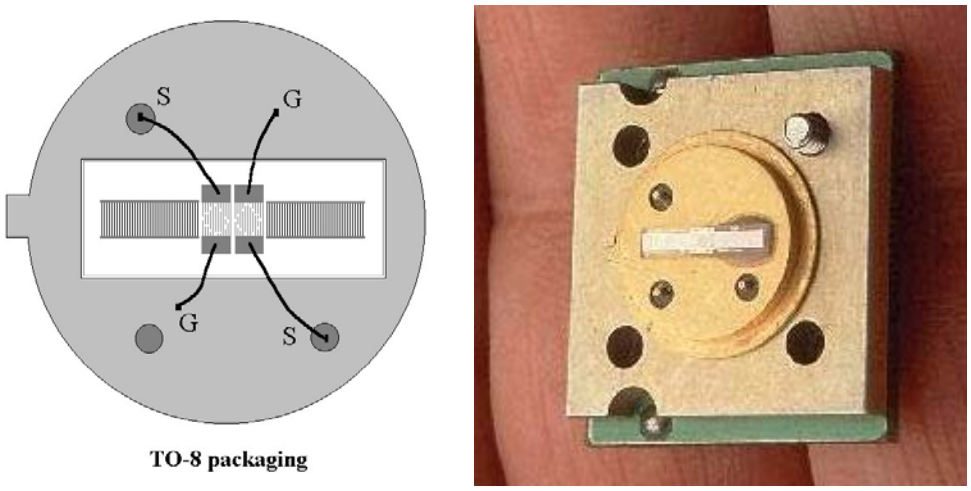

Figure A-5. Packaged SAW resonator. (a) Diagram of a wirebonded SAW resonator on a TO-8 package. (b) The actual SAW resonator mounted on the oscillator circuit board.

23. Test the packaged devices using a TO-8 test board connected to the network analyzer to make sure the wirebonding is done correctly. Calibration of the network analyzer is required before performing the on-board test using the specially designed TO-8 calibration kit. (see NOTE)

    NOTE: The TO-8 calibration kit for SHORT and THRU can be simply made by wirebonding S to G (body) for SHORT and S to S for THRU. For LOAD calibration kit, a 50 ohm chip resistor is soldered between S and G. The MAKK Corporation in Canada fabricated a TO-8 LOAD calibration kit for us.

24. Mount the tested SAW devices in the SAWPRO sensor array and perform the experiments.

APPENDIX B

Selected Publications and Presentations (As of June 2006)

Sang-Hun Lee, Eric W. Massey, and W.D. Hunt, "A Novel Method to Investigate Dependence of SAW Resonator Sensor Signatures on Localized Surface Perturbations," *2006 IEEE Sensors Conference,* Daegu, Korea.

Sang-Hun Lee, D.D. Stubbs, W.D. Hunt, and P.J. Edmonson, "A Method to Differentiate and Identify Analogous Chemical Substances Based on Orthogonal Signal State-Space Mapping," *IEEE Sensors Journal*, 2006

Christopher D. Corso, Desmond D. Stubbs, Sang-Hun Lee, Michael Goggins, Ralph H. Hruban, and William D. Hunt, "Real-time detection of mesothelin in pancreatic cancer cell line supernatant using an acoustic wave immunosensor," *Cancer Detection and Prevention Journal*, Vol 30, Issue 2, pp. 180-187, 2006

Sang-Hun Lee, D.D. Stubbs, J. Cairney, and W.D. Hunt, "Rapid Detection of Bacterial Spores Using a Quartz Crystal Microbalance (QCM) Immunoassay," *IEEE Sensors Journal*, vol. 5, no. 4, pp. 737-743, 2005

Desmond D. Stubbs, Sang-Hun Lee, and William D. Hunt, "Vapor Phase Detection of a Narcotic Using Surface Acoustic Wave Immunoassay Sensors," *IEEE Sensors Journal*, vol. 5, no. 3, pp. 335-339, 2005

Sang-Hun Lee, D.D. Stubbs, W.D. Hunt, and P.J. Edmonson, "Vapor Phase Detection of Plastic Explosives Using a SAW Resonator Immunosensor Array," *2005 IEEE Sensors Conference,* pp. 468-471, Urvine, CA, 2005.

Sang-Hun Lee, D.D. Stubbs, and W.D. Hunt, "Electronic Nose Technology Using SAW devices," *Georgia Graduate Student Interdisciplinary Conference 2004*, Feb. 2004

Sang-Hun Lee, D.D. Stubbs, J. Cairney and W.D. Hunt, "Real-time detection of bacterial spores using a QCM based immunosensor," *2003 IEEE Sensors Conference,* pp. 1194-1198, Toronto, Canada, Oct. 2003.

D.D. Stubbs, Sang-Hun Lee, W.D. Hunt, "Investigation of cocaine plumes using surface acoustic wave immunoassay sensors," *Analytical Chemistry*. 2003 Nov 15;75(22): 6231-5.

W.D. Hunt, D.D. Stubbs and Sang-Hun Lee, "Time-Dependent Signature of Acoustic Wave Biosensors," *Proceedings of IEEE*, vol. 91, pp 890-901, 2003.

D. D. Stubbs, W. D. Hunt, S. H. Lee, D. F. Doyle, "Gas phase activity of anti-FITC antibodies on a surface acoustic wave resonator device," *Biosen. Bioelectron.*, 2002, 17, 471-477

Stubbs, D.D., Lee, S.H., and Hunt, W.D., "Molecular recognition for electronic noses using surface acoustic wave immunoassay sensors," *IEEE Sensors Journal*, vol. 2, no. 4, pp. 294-300, August 2002.

Stubbs, D.D., Lee, S.H., and Hunt, W.D., "Vapor phase SAW immunoassay sensors," *2001 IEEE Ultrasonic Symposium*, pp. 357-360.

Patent Application

P.J. Edmonson, W.D. Hunt, S.H. Lee, and D.D. Stubbs "Differentiation and Identification of Analogous Chemical or Biological Substances with Biosensors," U.S. Patent Application No. 11/088809.

REFERENCES

[1] Stubbs, D.D., Lee, S.H., and Hunt, W.D., "Vapor phase SAW immunoassay sensors," *2001 IEEE Ultrasonic Symposium*, pp. 357-360.

[2] Stubbs, D.D., Lee, S.H., and Hunt, W.D., "Molecular recognition for electronic noses using surface acoustic wave immunoassay sensors," *IEEE Sensors Journal*, vol. 2, no. 4, pp. 294-300, August 2002.

[3] D.D. Stubbs, Sang-Hun Lee, W.D. Hunt, "Investigation of cocaine plumes using surface acoustic wave immunoassay sensors," *Analytical Chemistry*. 2003 Nov 15;75(22): 6231-5.

[4] Jay W. Grate and Mark Klusty, "SAW Vapor sensors Based on Resonator Devices," *Analytical Chemistry*, 1991, pp 1719-1727.

[5] Auld, B.A., *Acoustic Fields and Waves in Solids*, Vol I, 2nd ed. Krieger Publishing Company, 1990

[6] D.S. Ballantine,, R.M. White, S.J. Martin, A.J. Ricco, E.T. Zellers, G.C. Frye, Wohltjen, *Acoustic Wave Sensors, Theory, Design and Physico-Chemical Applications*, 1997 Academic Press.

[7] G. Sauerbrey, "Use of quartz vibrator for weighing thin films on a microbalance," *Z. Physik* vol. 155, 206-210, 1959.

[8] K.K. Kanazawa, J.G. Gordon, "Frequency of a quartz microbalance in contact with a liquid," *Anal. Chem*., vol. 57, pp. 1770-1771, 1985.

[9] M. Schweyer et al. 1996. "An Acoustic Plate Mode Sensor for Aqueous Mercury," *Proc Ultrasonics Symposium*, Vol. 1:355-358.

[10] R.M. White and F.W. Voltmer, "Direct piezoelectric coupling to surface elastic waves," *Appl. Phys. Lett*., 7, pp 314-316 (1965)

[11] Ballantine, D.S. and H. Wohltjen, "Surface acoustic wave devices for chemical analysis," *Analytical Chemistry* 61 (1989):704A–706A.

[12] M. Lewis, "Surface skimming bulk wave, SSBW," *Proc*. 1977 *IEEE Ultrasonic Symposium*, pp. 744-752, 1977

[13] B.A. Auld, J.J. Gagnepain, M. Tan, "Horizontal shear waves on corrugated surfaces," *Elec Lett*., vol. 12, No.24 pp. 650-651, 1976.

[14] Colin Campbell, *Surface Acoustic Wave Devices for Mobile and Wireless Communications*, Academic Press, 1998.

[15] K. Hashimoto, *Surface Acoustic Wave Devices in Telecommunications,* Springer, 2000, page 259.

[16] Baer et al. "STW Chemical Sensors," *IEEE Ultrasonic Symposium*, 1992, pp.293-298

[17] K. Hashimoto and M. Yamaguchi, "General-Purpose Simulator for Leaky Surface Acoustic Wave Devices Based on Coupling-Of-Modes Theory," *Proc. IEEE Ultrason. Symp*., pp.117-122, 1996.

[18] C.S. Lam and D.E. Holt, "A Comparison of Temperature Performance of SAW Filters Made On ST- And LST-Cut Quartz", *Proc. of Ultrasonic Symposium* 1988, pp. 273-277.

[19] C. Galli Marxer, M. Collaud Coen, T. Greber, U.F. Greber and L. Schlapbach, "Cell spreading on Quartz Crystal Microbalance elicits positive frequency shifts indicative of viscosity changes," *Analytical and Bioanalytical Chemistry*, 2003.

[20] Oliver Hayden, Roland Bindeus and Franz L Dickert, "Combining atomic force microscope and quartz crystal microbalance studies for cell detection," *Meas. Sci. Technol.,* vol.14, pp 1876-1881, 2003.

[21] Auld, B.A., *Acoustic Fields and Waves in Solids*, Vol II, 2nd ed. Krieger Publishing Company, 1990

[22] W.D. Hunt, D.D. Stubbs and Sang-Hun Lee, "Time-Dependent Signature of Acoustic Wave Biosensors," *Proc. IEEE.*, vol. 91, pp 890-901, 2003.

[23] Mirsky, V. M.; Riepl, M.; Wolfbeis, O. S., "Capacitive monitoring of protein immobilizationand antigen-antibody reactions on monomolecular alkythiol films on gold electrodes," *Biosens.Bioelectron*. 1997, 12, 977-990

[24] Dariusz Witt, Rafal Klajn, Piotr Barski, and Bartosz A.Grzybowski, " Applications, Properties and Synthesis of ω-Functionalized n-Alkanethiols and Disulfides - the Building Blocks of Self-Assembled Monolayers," *Current Organic Chemistry*, pp. 1763-1797(35), 2004

[25] Sang-Hun Lee, D.D. Stubbs, J. Cairney, and W.D. Hunt, "Rapid detection of Bacterial Spores Using a Quartz Crystal Microbalance (QCM) Immunoassay," *IEEE Sensors Journal*, 2005

[26] Horisberger, M. and Clerk, MF, "Labeling of Colloidal Gold with Protein A," *Histochemistry* 1985, 82, 219–223.

[27] Davis, K.A. and Leary, T.R. (1989). *Analytical Chemistry*, 61: 1227-1230.

[28] Gersten DM and Marchalonis JJ., "A rapid, novel method for the solid-phase derivatization of IgG antibodies for immune-affinity chromatography," *J Immunol Methods*, 1978; 24(3-4), pp 305–309.

[29] B. Michel *et al*, IBM *J. Research & Dev*. vol. 45 no. 5, 2001, pp 697-719

[30] H.J. van der Linden, S. Herber, W. Olthius, and P. Bergveld, *Analyst* 128 (2003) 325

[31] Prabhakar Tamirisa and Dennis Hess, "Plasma Polymerized Hydrogel Thin Films for Applications in Sensors and Actuators," 207th ECS Meeting, Canada, 2005

[32] Stubbs, D.D., Hunt, W.D., Lee, S.H. and Doyle, D.F. "Gas phase activity of anti-FITC antibodies immobilized on a surface acoustic wave resonator" *Biosensors and Bioelectronics*, Volume 17, Issues 6-7, 2002, pp 471-477.

[33] Sang-Hun Lee, D.D. Stubbs, J. Cairney, and W.D. Hunt, "Rapid Detection of Bacterial Spores Using a Quartz Crystal Microbalance (QCM) Immunoassay," *IEEE Sensors Journal*, vol. 5, no. 4, pp. 737-743, 2005

[34] J.F. Kearney, "Monoclonal antibodies specific for anthrax and peptides derived from the antibodies thereof," U. S. Patent 6,913,756, July 05, 2005.

[35] J.J. Quinlan and P.M. Foegeding, "Monoclonal antibodies for use in detection of Bacillus and Clostridium spores," *Appl. Environ. Microbiol.*, vol. 63, pp. 482–487, 1997.

[36] A.L. Sonenshein, J.A. Hoch, and R. Losick, *Bacillus subtilis and its closest relatives: from genes to cells*. ASM Press, Washington, D.C.

[37] René Scherrer and Philipp Gerhardt, "Location of Calcium Within Bacillus Spores by Electron Probe X-Ray Microanalysis," *J Bacteriol.* 1972 October; 112(1): 559–568

[38] Christopher D. Corso, Desmond D. Stubbs, Sang-Hun Lee, Michael Goggins, Ralph H. Hruban, and William D. Hunt, "Real-time detection of mesothelin in pancreatic cancer cell line supernatant using an acoustic wave immunosensor," Accepted for publication in *Cancer Detection and Prevention Journal*, 2006

[39] W.D. Bowers, R.L. Chuan, and T.M. Duong, "A 200 MHz surface acoustic wave resonator mass microbalance," *Rev. Sci. Instrum.* 62, 1624 (1991)

[40] J. Reibel, S. Stier, A. Voigt, and M. Rapp, "Influence of Phase Position on the Performance of Chemical Sensors Based on SAW Device Oscillators," *Analytical Chemistry* 70 (1998) pp. 5190–5197.

[41] R.F. Mitchell and D.W. Parker, "Synthesis of acoustic surface wave filters using double electrodes," *Elec. Letters*, vol. 10, pp 512, 1974

[42] R.H. Tancrell, M.B. Schulz, H.H. Barrett, L. Davies, and M.G. Holland, "Dispersive delay lines using ultrasonic surface waves," *Proc. IEEE*, 57, 1211-1213 (1969).

[43] Supriyo Datta, *Surface Acoustic Wave Devices*, Prentice Hall, 1984.

[44] Colin Campbell, *Surface Acoustic Wave Devices and Their Signal Processing Applications,* Academic Press, Boston, 1989.

[45] P.Hartemann and E.Dieulesaint. *Electronics Lett.*, 5, 657-658 (1969).

[46] R.H.Tancrell and R.C.Williamson. *Appl. Phys. Lett.*, 19, 456-459 (1971).

[47] B.J. Hunsinger and S. Datta, "A Generalized Model for Periodic Transducers with Arbitrary Voltages," *IEEE International Ultrasonics Symposium*, 1978, pp. 705-709

[48] Dong-Pei Chen and H.A. Haus, "Analysis of Metal-Strip SAW Gratings and Transducers," *IEEE Trans. Sonics and Ultrasonics*, Vol 32, pp. 395-408, May 1985.

[49] L.A. Coldren and R.L. Rosenberg, "Scattering Matrix Approach to SAW Resonators," *Proc. IEEE Ultrasonics Symposium* 1976, pp 266- 271.

[50] S. Cross, WR Shreve and T. S. Tan, "Synchronous IDT SAW. resonators with Q above 10000," *Proc. IEEE Ultrason. Symp*., 1979, pp 824-829.

[51] W.D. Bowers, R.L. Chuan, T.M. Duong, and B.H. Horine, "The Positional Dependence of a Surface Acoustic Wave Crystal's Mass Sensitivity," *Proc. 178th Mtg. Electrochem. Soc.*, October 14-19, 1990, Seattle, WA.

[52] W. Bowers, R. Chuan, and T. Duong, "A 200 MHz Surface Acoustic Wave Resonator Mass Microbalance," *Rev. Sci. Instrum.*, Vol. 62 (6):1624-1629, 1991.

[53] Edmonson, Hunt, Lee, and Stubbs "Differentiation and Identification of Analogous Chemical or Biological Substances with Biosensors" U.S. Patent Application No. 11/088809.

[54] Behring, E. & Kitasato, S. *Dt. Med. Wochenschrift*. **16,** 1113–1115 (1890).

[55] Cameron, D.J. & Erlanger, B.F. *Nature* **268,** 763–765 (1977).

[56] Leo C. James and Dan S. Tawfik. *Protein Sci.* **12,** 2183-2193 (2003).

[57] Anne Zeck, Michael G. Weller, & Reinhard Niessner. *Fresenius J. Anal. Chem.* **364,** 113-120 (1999).

[58] Laura M. Matz, Pete S. Tornatore, & Herbert H. Hill. *Talanta* **54,** 171-179 (2001).

[59] Avraham Bromberg & Richard A. Mathies. *Anal. Chem.* **75,** 1188-1195 (2003).

[60] Leo C. James, Pietro Roversi, and Dan S. Tawfik. *Science* **299,** 1362-1377 (2003).

[61] M.Suzuki, F.Ozawa, W.Sugimoto, and S.Aso, "Miniaturization of SPR immunosensors," *Analytical Sciences*, 17, pp.265-267 (2001)

VITA

SANG HUN LEE

Sang Hun Lee was born in Seoul, Korea. He earned a B.Eng. degree in Electronics from Korea University in 1998. Prior to finishing his undergraduate study, Mr. Lee served in the U.S. Army, Seoul, Korea, for two years. He crossed the Pacific Ocean to study graduate courses at Georgia Tech and joined Professor William Hunt's research group in 2000 where he did interdisciplinary research on acoustic wave biosensors and earned M.S. and Ph.D. degrees. When he is not working on his research, Mr. Lee enjoys traveling with his wife and kids and listening to heavy metal music at maximum volume.